FLUID DYNAMIC. EVALUATION IN

MODELS OF ARTERIAL BRANCHES

FLUID DYNAMIC EVALUATION IN

MODELS OF ARTERIAL BRANCHES

by

OSAMA A. A. EL MASRY, B.SC., M.ENG.

A Thesis

Submitted to the School of Graduate Studies

in Partial Fulfilment of the Requirements

for the Degree

Doctor of Philosophy

McMaster University

September 1977

DOCTOR OF PHILOSOPHY (1977)   McMASTER UNIVERSITY
(Mechanical Engineering)   Hamilton, Ontario

TITLE: Fluid Dynamic Evaluation in Models
                    of Arterial Branches

AUTHOR: Osama A. A. El Masry,

                    B.Sc. (Alexandria University)
                    M.Eng.(McMaster University

SUPERVISORS: Dr. G. F. Round
                    Dr. I. A. Feuerstein

NUMBER OF PAGES: xvi, 185

ii

ABSTRACT

The purpose of this investigation is to determine experimentally the fluid dynamic field in models of arterial branching vessels and to identify the flow features which might influence the predominant occurrence of atherosclerotic lesions in such vessels.

Flow conditions in four rigid-walled models representing the aortic bifurcation, iliac bifurcation, mesentric artery branch and renal artery branch are investigated over a Reynolds number range of 1000-4000 and a complete range of flow division between daughter vessels. Qualitative flow streamline patterns and quantitative definition of those flow conditions leading to flow separation are determined primarily at steady flow with a limited set of pulsatile experiments. The flow patterns observed are photographed using high speed cinephotography and a neutrally-buoyant tracer-particle technique. The flow streamline patterns in the four models are complicated and characterized by secondary flow motion. This motion is accentuated with increasing Reynolds number. Flow separation is inducible through alteration of flow division between daughter vessels or by an increase in the flow rate. Each of the four models has distinct combinations of flow rate and flow division ratio which give flow separation at the outside wall of one or both daughter tubes. The separated flows observed here display

iii

streamlines forming an open vortex with flow entering and leaving. The site of the separation point in the branching plane is approximately constant with the reattachment points occurring further downstream as Reynolds number increases and as the branch flow rate decreases.

Shear rate distributions at the walls of the four models are measured using an electrochemical technique. This technique is based on an oxidation-reduction reaction at electrodes implanted in the wall. Distribution of wall shear rate of the branching site is very non-uniform, with high shear rate at the leading edge of the flow dividers. The shape of the shear rate curves are functions of the geometry, total flow rate and most importantly the flow division ratio. An unstable pattern of shear is found at the wall where separation is expected to occur. For pulsatile flow, the time-averaged rate of shear is not appreciably changed by frequency and amplitude of pulsation. The biological implication of the results is discussed with specific reference to the sites of atherosclerotic lesions found in man for these geometries.

ACKNOWLEDGEMENTS

TABLE OF CONTENTS

LIST OF FIGURES

LIST OF SYMBOLS

A   Cross-section area of electrode surface, sq. cm.

C   Concentration of ferricyanide ion, moles/cm^3

C_b & C_w Concentration in the bulk and at the wall respectively, moles/cm^3

$\bar{c}$ Time-averaged concentration, moles cm^3

c'   Fluctuating component of concentration, moles/cm^3

D   Parent-tube diameter, cm

D_o Parent-tube diameter at neck section, cm

D   Diffusion coefficient, sq. cm/sec

d   Daughter-tube diameter, cm

$d_{elect.}$ Electrode diameter, cm

F   Faraday's constant, 96, 479 Coulombo/mole

f   Frequency of pulsation, c/sec

i   Cathode current, micro-Amperes

K   Mass-transfer coefficient, cm/sec

$\bar{K}$ Average mass-transfer coefficient, cm/sec

k'   Fluctuating component of mass-transfer coefficient, cm/sec

L   Length of rectangular electrode surface, cm

L_e Equivalent linear length for a circular electrode, cm

Q   Volumetric flow rate, cm^3/sec

R   Parent-tube radius, cm

S   Wall shear rate, sec^{-1}

S*   Dimensionless shear rate

$\bar{s}$ Time-averaged shear rate, sec^{-1}

s'   Fluctuating component of shear rate, sec^{-1}

T	Temperature, $^{\circ}K$
t	Time, sec
u	Velocity in x direction, cm/sec
$\bar{u}$	Mean velocity in x direction cm/sec
u'	Fluctuating velocity in x direction, cm/sec
v	Velocity in y direction, cm/sec
$\bar{v}$	Mean velocity in y direction, cm/sec
v'	Fluctuating velocity in y direction, cm/sec
w	Radian frequency, $= 2\pi f$, sec^{-1}
x	Direction parallel to electrode surface, cm
y	Direction perpendicular to electrode surface, cm

Greek Symbols

α	Unsteadiness parameter, $R\sqrt{\dfrac{w}{\nu}}$
β	Area ratio, $\dfrac{d_L^2 + d_R^2}{D^2}$
Γ	Gamma function
γ	Area ratio d_L^2/d_R^2
δ_C	Concentration boundary-layer thickness
ε_D	Eddy diffusivity, cm^2/sec
η	Dimensional transformation variable defined by Equation (5.19)
θ	Branch take-off angle
λ	Velocity amplitude ratio, $= u'/\bar{u}$
μ	Viscosity, gm/cm sec
ν	Kinematic viscosity, cm^2/sec
ρ	Fluid density gm/cm^3
σ	Branch flow division ratio, Q_i/Q_t

xiv

ψ Outside curvature of the branch, cm

Re   Reynolds number $(\frac{\rho \bar{u} D}{\mu})$

Sc   Schmidt number $(\frac{\nu}{D})$

Subscripts

i   Either left or right side branch

L   Left side branch

R   Right side branch

t   Total

LIST OF TABLES

CHAPTER 1

INTRODUCTION

1.1 The Problem

The work presented here on flow phenomena at branch-
ing sites was motivated by questions concerning the role
played by blood flow dynamics in the initiation and develop-
ment of arterial diseases. The disease of particular interest
here is atherosclerosis.

Atherosclerosis is a degenerative disease of the
arteries in which lipid deposits called atheromatous plaques
form in the subintimal layer of the arteries. They are
usually associated with degenerative changes in the arterial
wall. In the early stages, these deposits do not interfere
significantly with the flow of blood supplied by the vessels
affected. However, as time goes on, fibroblasts cause
sclerosis of the arteries and calcium precipitates with the
lipids to cause calcified plaques which can lead to gradual
occlusion of these vessels and to very detrimental effects
in the organs and tissues supplied.

Over one half of all human deaths are caused, either
directly or indirectly, by atherosclerosis. It is present
to some degree in almost all adults. The conditions usually
becomes worse with age. Yet, atheroscterotic lesions can be

1

found in children, even infants [1][1]. Thus atherosclerosis
is not only limited to old age.

1.2. Atherosclerosis and Flow

Atherosclerotic lesions tend to form near sites of
change of arterial configuration, such as branching sites
and curved segments. These areas of the arterial tree
experience different hemodynamic forces than others [2], [3].
This has led many investigators to consider the relation
between hemodynamic flow patterns and the development of
atherosclerosis. A variety of mechanisms [2], [4], [5]
have been proposed to explain this relation, but no unified
theory which adequately reconciles all of the known facts
has yet been developed.

Caro et al. [2] have shown that local vessel shapes
are an important factor in the formation of initial deposits
and claimed that the distribution of early atheroma is
coincident with those regions in which arterial wall shear
stress is relatively low. Based on their theoretical analysis
of diffusion in a developing boundary layer adjacent to a
solid wall, they pointed out that diffusion is enhanced both
to and from the wall by high velocity gradients and inhibited
by low velocity gradients. Considering this in conjunction
with experimental evidence that lesions occurred in low shear
regions in animals not receiving excess cholesterol in their

---

[1] Numbers in square brackets refer to references given at
the end of the thesis.

diet, these authors argued that the lesions were formed by cholesterol originating in the intima and preferentially kept within the wall through adverse conditions for mass transfer to the lumen. This mechanism for the formation of atheromatous lesions is based on a shear-dependent mass-transfer process. However, subsequent experiments [6] on the transport of C^{14}-cholesterol between serum and vessel walls in a perfused segment of the artery have demonstrated that the uptake process is not a shear-dependent mass-transfer boundary-layer process.

Fry [5] has shown that vascular endothelial cells in vivo undergo damage upon application of high shear stress (379 ± 85 dynes/cm^2). However, this level of shear rate is probably above the physiologically attainable range. Fry [7] also suggested that the flux to the wall of Evans blue dye bound to albumin increases to significant levels at wall shear stress well below this critical level and that the flux of lipo-proteins to the wall may be facilitated by moderate stress level. In a later paper, Fry [8] reported that exposure of the normal endothelial surface to elevated levels of shearing stress increased the wall permeability and with concomitant increase in serum cholesterol level, initial lipid deposition might occur.

Recent experimental studies by Caro [9] and Siflinger et al. [10] with injured (endothelium removed) and normal canine carotid artery segments have demonstrated that

arterial endothelium is the principal barrier to the passage of macromolecules (the size of albumin and low density lipoproteins) from the lumen into the arterial wall and the rate of passage of these macromolecules is strongly influenced by a variety of mechanical factors. These include the fluid flow pattern and steadiness and amplitude of the fluid pressure and shearing stress. Furthermore, Weinbaum et al. [11] have proposed that the passage of these macromolecules across the endothelium is primarily through a passive random motion of small pinocytotic vesicles. Theoretical, experimental and electronmicroscopic studies have been undertaken by this group in order to understand the mechanisms which might cause pinocytotic transport to be increased by mechanical factors. The preliminary results of this study suggest that pinocytotic transport rate is substantially increased by the application of unsteady mechanical stresses. However, the detailed mechanism of this process is obscure.

The work summarized and discussed above indicates that hydrodynamic flow factors may be very important in the formation of atheromatous lesions directly by causing functional and structural changes in the endothelial surface or indirectly through control of mass-transfer rates to and across the endothelium. Questions still remain, however, as to how and in what sequence smooth muscle cells, lipoproteins, cholesterol and thrombi accummulate at the focal sites, eg., curved segments of the arteries, branching sites

and bifurcations where lesions have been observed. The
evidence indicate that local fluid dynamics may play a part
in the selection of these sites. However the fluid mechanical
data previously published does not give a satisfactory
picture of the three dimensional character of streamlines,
boundary layer separation sites, velocity and velocity
gradients in arterial shapes prone to atheroma.

1.3 Fluid Dynamics of Branching Vessels

The problems which arise in studying flow in branch-
ing vessels prone to atherosclerosis are complicated by
several phenomena characteristic of the human cardiovascular
system. The vessel configuration is a three dimensional
complex geometry, the hemodynamic field is determined by
the complex rheological properties of blood and the vessel
wall and blood flow through the circulatory system is pulsatile.
The combination of these phenomena is not only complex to be
modelled experimentally but describing them mathematically
is a formidable task. In light of this, studies on the
flow of fluids in branching vessels have in the past eliminated
one or more of the complexities in order to simplify the
problem.

Knox [12] has studied the pressure drop downstream
of side branches and the effect of branch angle and area
ratio on the developed flow recovery lengths.

Motivated by their interest in the mechanics of lung
functions, Schroter and Sudlow [13] have studied the velocity

profiles in three dimensional symmetric bifurcation models
using hot-wire anemometry. This study has shown that simple
Poiseuille flow does not exist in the regions of the lungs
exhibiting a Reynolds number of 300 to 700, a range also
found in some large arteries. However the hot-wire probe
used did not define the flow patterns within the vessel
junction. In a later study Pedley et al. [14] used this hot-
wire probe data to estimate viscous energy dissipation and
pressure drop in branched airways.

A study by Schreck and Mockros [15] of flow in three
dimensional model bifurcations has produced a series of
velocity plots depicting flow profiles, similar to those of
Schroter and Sudlow.

Brech and Bellhouse [16] employed a specially designed
thin film velocity probe to study the velocity profiles and
wall shear rates in one particular geometry of a symmetric
bifurcation. These authors have found contra-rotating
helical vortices in the outside section of each daughter vessel
along with a high shear stress region on the inside wall of
each daughter vessel and a low shear stress region on the
outside wall.

El Masry [17] studied the velocity profiles and
surface shear rates in a series of symmetric bifurcations.
Area ratio and parent tube flow rate were the two independent
variables evaluated. Local velocity measurements were made
using tracer particle technique and high speed cine photography.
An analytical representation of the velocity as a mathematical

function of radial and angular positions was formulated for
a number of locations downstream of the carina. Wall shear
rates were deduced from these functions and found to be a
scaled and displaced cosine function at any axial position.

Roach et al. [18] have photographed fluid stream-
lines in glass bifurcations by injecting Evans blue dye
upstream of the bifurcation. Boundary-layer separation was
seen and the critical Reynolds number for turbulence was
determined and ranged from 2500 for a long straight tube to
1000 for a 180° bifurcation.

Fox and Hugh [4] have examined flow patterns in two
dimensional channel analogs of a right angle branch, a
bifurcation, a divergent channel and a curved vessel. These
authors found a correlation between areas where atheroma
is known to occur and locations of boundary layer separation.
It was suggested that high levels of cholesterol may initiate
boundary layer separation by increasing blood viscosity.

Rodkiewicz and Roussel [19] have studied the manner
in which the flow divides at an arterial junction where a
single branch leaves the parent trunk. The ratio of the
flow rate in the side branch to the flow rate in the main
trunk was found to increase with the decrease of the entrance
Reynolds number and the branching angle. Separation regions,
one in each branch have been observed together with the double
helical flow in the side branch. Rodkiewicz [20] has
additionally shown the presence and importance of a number of
flow separation and stagnation regions in a channel flow

model of the aortic arch.

Talukder [21] studied flow patterns and wall shear stress in plexiglass and flexible PVC models. A flow visualization technique was used to obtain the streamline patterns and a hot-film probe was used for the shear stress measurements. Models with area ratio equal to 1.2 only were used in this study. Observations provided evidence of secondary flow in both branches and flow separation at the outer wall of the branch of lower mean velocity. Wall shear measurements showed oscillatory wall shearing stresses for pulsatile flow with peak values which are many times higher than the steady flow values.

Several workers have done experiments under controlled fluid mechanical conditions using biological fluids. Goldsmith [22] has shown that in areas of disturbed flow vortices are formed and that velocities and velocity gradients close to the wall of the vessel are small. He suggested that small particles such as platelets will preferentially enter such vortices providing a mechanism for their accummulation and collision with the wall. Yu and Goldsmith [23] in a later paper, using 2µ latex spheres suspended in a 45 percent reconstituted red cell ghost suspension demonstrated the formation of aggregates of spheres in a vortex downstream of a restriction placed in a glass tube, the aggregates were found to deposit on the adjacent wall.

Murphy et al. [24] have carried out flow studies in plastic models of a number of arterial geometries using blood

from swine in an extracorporeal circuit. In bifurcation models they found that deposits were formed on the walls at the lips of the bifurcations and in multiple right-angle branches, proximal lips of the orifices are spared with the heaviest deposits found on the lateral margins.

Efforts to measure in vivo velocity profiles at the junction of the aorta with the common iliac artery of the dog have been made by Gutstein et al. [25]. Using a hot-wire anemometry for velocity measurements, they have found extremely unstable flow patterns near this junction and suggested that these disturbances will generate high shear stresses in the fluid which may be transmitted to the adjacent endothelium.

Schultz et al. [26], using then hot-film probes, have made velocity measurements in the ascending and descending throacic aorta in dogs. Flat velocity profiles were found in the ascending aorta and in the first part of the descending aorta. More developed profiles were found in the lower thoracic aorta and in the femoral artery. However, the hot-film anemometer method when used in vivo lacks sufficient resolution close to the wall for accurate measurements of either the velocity gradient or the shear stress in these critical regions of the arterial system.

Analytical approaches to the problem have been recently carried out by a number of investigators. Lew [27], [28] has solved the Navier-Stokes equations for the case of two-dimensional flow with low Reynolds number and zero bifurcation angle. Lynn et al. [29] have computed stream functions

and vorticity profiles for two-dimensional branching flow. Zamir and Roach [30] have solved the Navier-Stokes equations for high Reynolds number in a zero angle branch. In general, the velocity profiles obtained from these analytical solutions do not show the multiple peaks and inflection points of the velocity profiles obtained experimentally by El Masry [17], Schroter and Sudlow [13], and Brech and Bellhouse [16]. This can be attributed to the simplifications incorporated into these analytical models.

A finite difference technique was employed by Ehrlich [31] and by Friedman et al. [32] to obtain shear stress distribution in a symmetric two-dimensional branch for both steady and pulsatile flow conditions. In the latter work, comparisons between pulsatile flow and steady flow results at the same mean flow rate showed that the severity of the hemodynamic variables of interest was increased by pulsatility.

The finite element method was also used to calculate shear stress and pressure profile by Ray and Davids [33] in inlet section models with plugging and by Davids and Cheng [34] in ducts of arbitrary cross section.

Both the finite difference technique and the finite element method yield useful information regarding flow patterns in simple conduit geometries. However, the geometries used were only crude approximations to the real arterial geometries.

From the above review and discussion, one must conclude that all previously published fluid dynamic data do not give a satisfactory quantitative picture of the three dimensional character of streamlines, velocity and velocity gradients in arterial shapes prone to atheroma.

1.4   Scope of the Present Study

In this work, detailed fluid dynamic evaluation was carried out on four rigid-walled arterial models typical of blood vessels in man.   The dimensional and geometrical characteristics of these models were based on typical measurements from angiograms and data available from the literature for a number of blood vessels prone to atheroma.   Both steady and pulsatile flow were studied over a wide range of flow parameters.   This included total flow rate (Reynolds number), daughter to parent tube flow rate ratio, and frequency of pulsation under pulsatile flow conditions.

A neutrally-buoyant tracer-particle technique was used with high speed cine photography to study the flow patterns and boundary layer separation phenomenon in the experimental models.   Streamline patterns and secondary flow motions were observed over a wide range of flow parameters. Boundary layer separations were also observed, with separation in one or both of the daughter tubes occurring within the physiological range of flow parameters.   The sites of separations and the size of the separation regions were also obtained as a function of the total flow rate, the flow rate

ratio and unsteadiness parameter.

The prediction of the magnitude and direction of shearing stress along the walls of arteries has been one of the main goals of many theoretical and experimental studies, yet, very few direct measurements of this quantity have been obtained. In this study, shear rate distribution along the walls of the arterial models were measured by means of an electrochemical technique. This technique is based on an oxidation-reduction reaction at electrodes implanted in the wall. Measurements were made precisely over an extremely small surface area (the area of the electrode face). Distributions of wall shear rate along the outside walls and flow dividers of the models were obtained under steady and pulsatile flow conditions. Unstable patterns of shear, at the wall where separation is expected to occur, were also studied.

Finally, the physiological implications of the results of this study are discussed with specific reference to the sites of atherosclerotic lesions found in man for these geometries.

CHAPTER 2

ARTERIAL MODELS

2.1 Anatomical Background

The abdominal aorta (abdominal part of the descending aorta), (Figure 2.1), gives rise to a number of small paired branches including ones to the abdominal wall (not shown in the illustration). The major branches in this part of the aorta are to the digestive tract and to the kidneys. The branches to the digestive tract, unpaired and three in number, arise from the front of the aorta. The first is the coeliac trunk, which through three major branches, supplies the upper abdominal organs (stomach, liver, duodenum and pancreas spleen); next is the superior mesenteric artery which partly overlaps the distribution of the coeliac trunk but supplies almost all the small intestine and much of the large intestine; last is the inferior mesenteric artery, supplying the more caudal part of the large intestine.

The arteries to the kidneys (renal arteries) arise from the sides of the aorta and are therefore paired, typically one to each kidney. The aorta ends in the lower part of the. abdomen by bifurcating into paired common iliac arteries.

The two common iliac arteries, the terminal branches of the aorta, are like other paired arteries in being essentially similar. Each runs downward and laterally and ends by dividing

DIAPHRAGM

COELIAC

R. RENAL

S. MESENTERIC

I. MESENTERIC

AORTIC BIF.

ILIAC BIF.
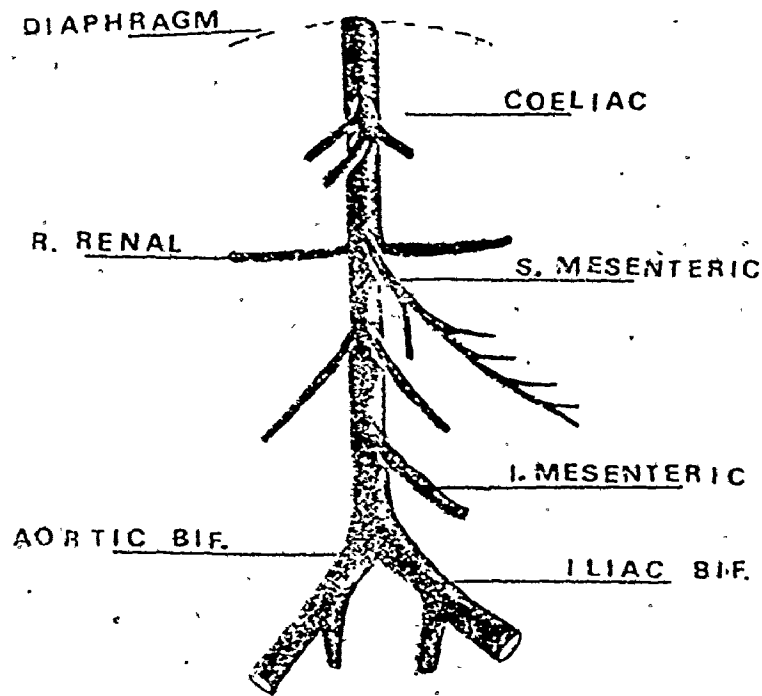
ABDOMINAL AORTA

Figure 2.1 Anatomical Sketch of the Abdominal
Aorta Showing Its Major Branches
and Bifurcations.

into internal and external iliac arteries.

The internal iliac artery descends into the pelvis
and supplies the pelvic viscera (bladder, uterus and vagina
in the female and rectum), sends branches into the buttocks
to supply the muscles there and one branch to the perineum
(space between the thighs) to supply the structure there.

The external iliac continues without diminuation in
size into the thigh. As this artery enters the thigh its name
becomes the femoral artery.

2.2   Localization of Atherosclerotic Lesions

The selective localization of atherosclerotic lesions
is one of the most striking features of this disease.
Different parts of the vascular tree, and indeed different
segments of a given artery, show wide differences in their
degree of involvement. This, in fact, has led many investi-
gators to suggest that mechanical and haemodynamic factors
might be important in the genesis of atherosclerosis.

In examining the aorta, one notices that arterial lesions
tend to spare the aortic wall around and immediately distal
to the ostia of the paired intercostal arteries. Some sparing
may also be noted immediately below the ostia of the more
distal branches such as the coeliac, superior mesenteric, renal
and inferior mesenteric arteries (Michell and Schwartz [35]).
In sharp contrast to that, the mouths of the intercostal and
the more distal branches are common sites for raised fibrous

plaques.

All types of raised plaques (fibrous, sudanophilic and complicated plaques) are far more common in the abdominal aorta than in the thoracic segment. Also calcification and surface thrombosis are very much more common in the abdominal part than in the thoracic part of the descending aorta. This distribution pattern is in contrast to the distribution of fatty streaks which are common in the descending arch and upper part of the thoracic aorta.

In comparing the carotid and iliac arterial systems, it is clear that the frequency of severe disease in the iliac arteries is considerably higher than in the carotid arteries, except for the carotid sinus. In the iliac system itself, the right common iliac shows a greater prevelence of severe disease than the left. Also the external iliac arteries show a remarkably low prevalence of severe disease in comparison with the common and internal iliac arteries.

It has been shown [35] that the selective involvement of some arteries, and the relative freedom of others can not be considered on the basis of arterial structure. Arteries with the same basic structure may have differing degrees of disease prevelance, while other arteries, with a very dissimilar structure may show a similar disease severity. One must conclude, therefore, that the selective localization of the disease is a result of the different flow conditions and geometric characteristics to be found in different segments of the arterial tree.

2.3 Dimensional and Geometrical Characteristics of the Models

In this work, the flow in four rigid-walled arterial models typical of major branching vessels and bifurcations of the abdominal part of the human aorta were studied in detail.

As a first step in model preparation, angiograms of a number of arteries were studied. These included: the abdominal part of the descending aorta and its major branches (superior mesenteric, coeliac and renal arteries), the aortic and the common iliac bifurcations and their arteries. Measurements of vessel diameter, take-off angle and radius of curvature of the transitions between parent and daughter tubes were made. Comparisons were made with data from the literature [3, 36, 37]. Although a certain degree of variability was observed, common geometrical characteristics were found and these were incorporated into the four models described in more detail below. Figures 2.2 to 2.5 show drawings for the models with dimensions given in Table 2.1. The entrance tube for all the models was for convenience made 2.2 cm, thus requiring scaling from anatomical information for fabrication. Since Reynolds number is reported for all observations and experiments, direct comparisons are possible with other data at equal Reynolds numbers due to dynamic similarity.

Model 1

This is a model of a symmetrical branch typified by the aortic bifurcation. Anatomically, this bifurcation is

TABLE 2.1

Geometrical Information for Models

MODEL	Parent tube		Left branch			Right branch			β	γ
	D(cm)	D_o(cm)	d_L(cm)	θ_L(°)	ψ_L(cm)	d_R(cm)	θ_R(°)	ψ_R(cm)		
1	2.2	1.8	1.27	37.5	1.8	1.27	37.5	1.8	1.0	1.0
2	2.2	2.2	1.27	45	2.2	1.8	20	6.6	1.0	.5
3	2.2	2.2	1.27	45	2.2	Straight continuation of parent tube			1.33	.333
4	2.2	2.2	.9	90	1.1	Straight continuation of parent tube			1.17	.167

θ Branch take-off angle

β Area ratio $= \dfrac{\text{area of daughter tubes}}{\text{area of parent tube}} = \dfrac{d_L^2 + d_R^2}{D_o^2}$

ψ Outside curvature of the branch

γ $\dfrac{\text{Left daughter tube area}}{\text{Right daughter tube area}} = \dfrac{d_L^2}{d_o^2}$

L = 3D

D

Do

Do

Do

OUTSIDE

OUTSIDE

d₁

INSIDE

d₂

37.5°   37.5°

MODEL 1

AORTIC BIFURCATION
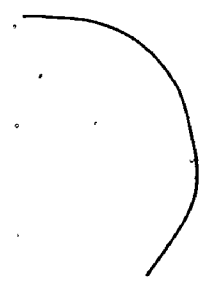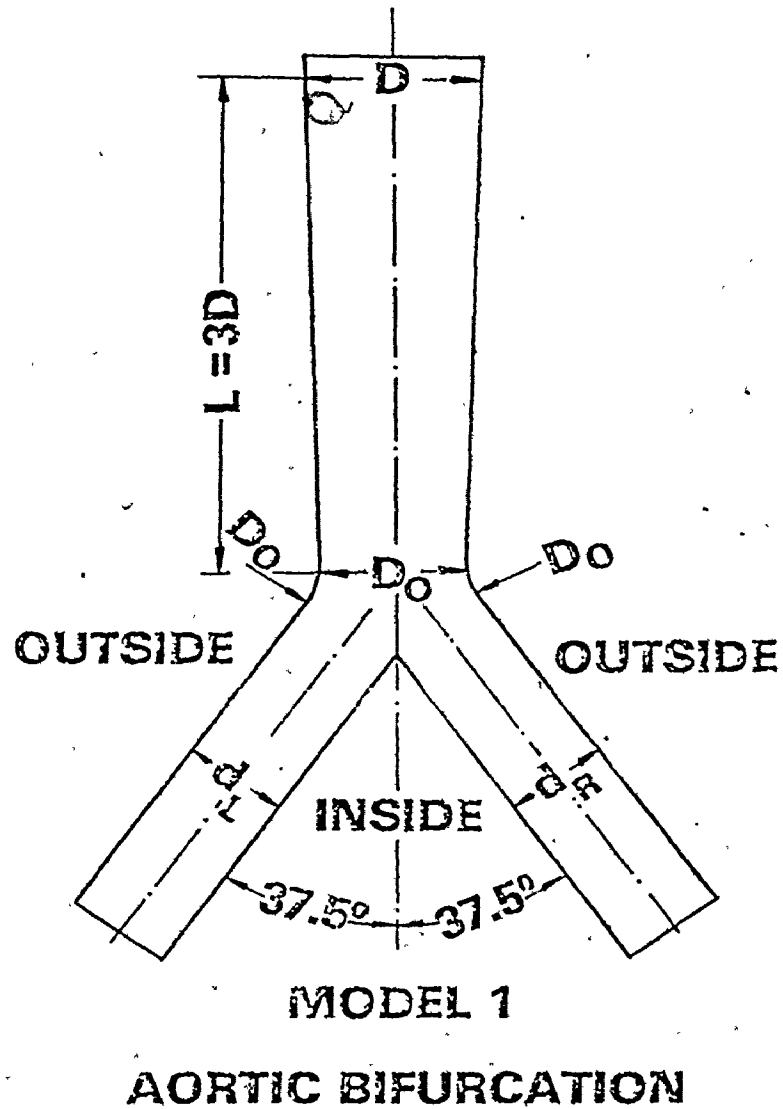
Figure 2.2   Geometrical Characteristics, of Model 1
(Dimensions are given in Table 2.1).

symmetrical having an angle between the two branches in the range 60°-90°. It has been reported [38] that the descending aorta undergoes a 40 percent reduction in area over its length. Experimental measurements [39, 40] have led to an exponential dependence for the area as a function of distance measured from the proximal site. The equation describing this taper is

$$A_n = A_o \ C^{-Bx/R_o}$$ (2.1)

where x is the distance coordinate, A_o and R_o are the mean area and radius at the proximal site and B is the taper factor. Such a taper was incorporated in the design of the parent tube of this model over three diameters upstream of the neck section (D_o), (see Figure 2.2).

The parent and daughter tube diameters were chosen to provide for an area ratio of 1.0 (total outflow area to neck section inflow area). This area ratio is in the physiological range of the aortic bifurcation in man, Gosling et al. [40].

Model 2

This is a model of the common iliac bifurcation in man. Since the internal iliac artery has a larger take-off angle than that of the external, an asymmetric branch results. In some cases [35], the external iliac artery is a straight continuation of the common iliac. The take-off angles selected were 20 and 45 degrees. The daughter tube diameter ratio was then selected with the aid of the mathematical relationship:
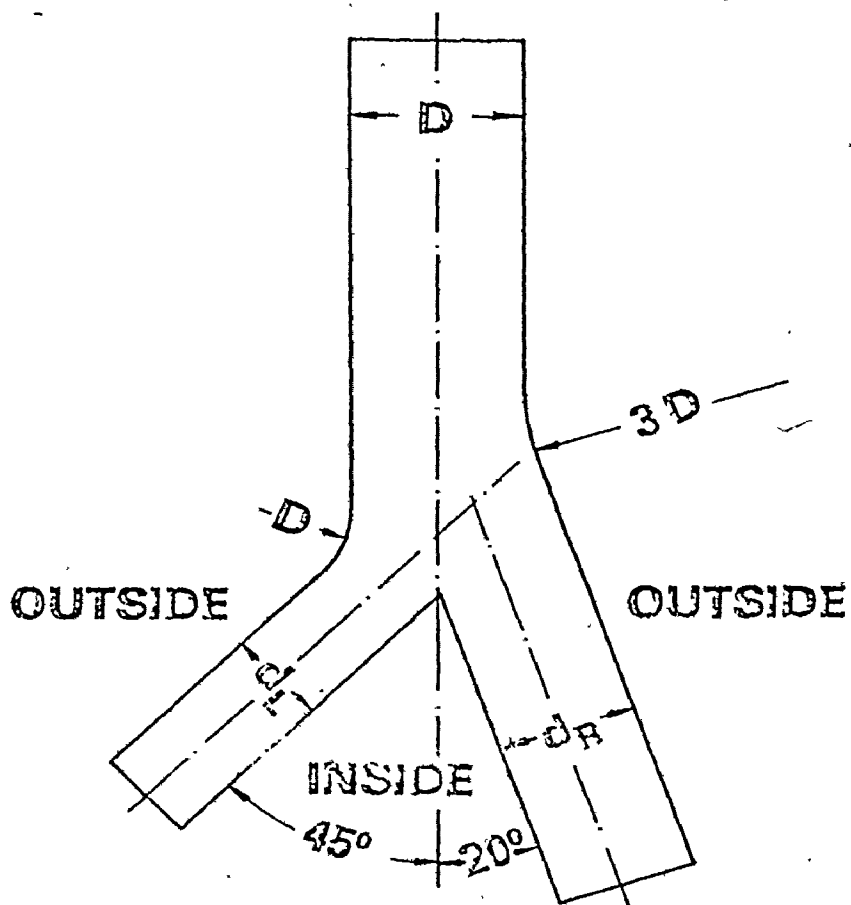
MODEL 2

ILIAC BIFURCATION

Figure 2.3   Geometrical Characteristics of Model 2
(Dimensions are given in Table 2.1).

$$\frac{d_L^2}{d_R^2} = \frac{\sin \theta_R}{\sin \theta_L} \qquad (2.2)$$

where the branch of smaller diameter (d_L) deviates from the stem of the model by the larger angle (θ_L). This mathematical form was derived from the momentum equation [42] and has been shown to be applicable in a number of physiological cases.

A total outflow to inflow area ratio of 1.0 was selected for this model to complete the geometrical definition of this model (Figure 2.3).

Model 3

This model is representative of the major branches emanating from the abdominal aorta to supply the digestive system. The three branches (coeliac, superior mesentric and inferior mesentric) take-off at a sharp angle (less than 90°) to the aortic trunk. They vary in size in the range (7-20 mm), Gray [36]. In the model, a 45° take-off angle and a 12.7mm diameter were selected for the side branch. The other daughter tube was modelled as a straight continuation of the parent tube. this resulted in an area ratio of 1.33.

Model 4

This model is a simplifed version of a renal artery emanating from the main aortic trunk. The renal arteries are paired and branch from the two opposite sides of the aorta, one to each kidney. Only one renal artery is modelled here. They appear to be nearly perpendicular to the main aortic trunk
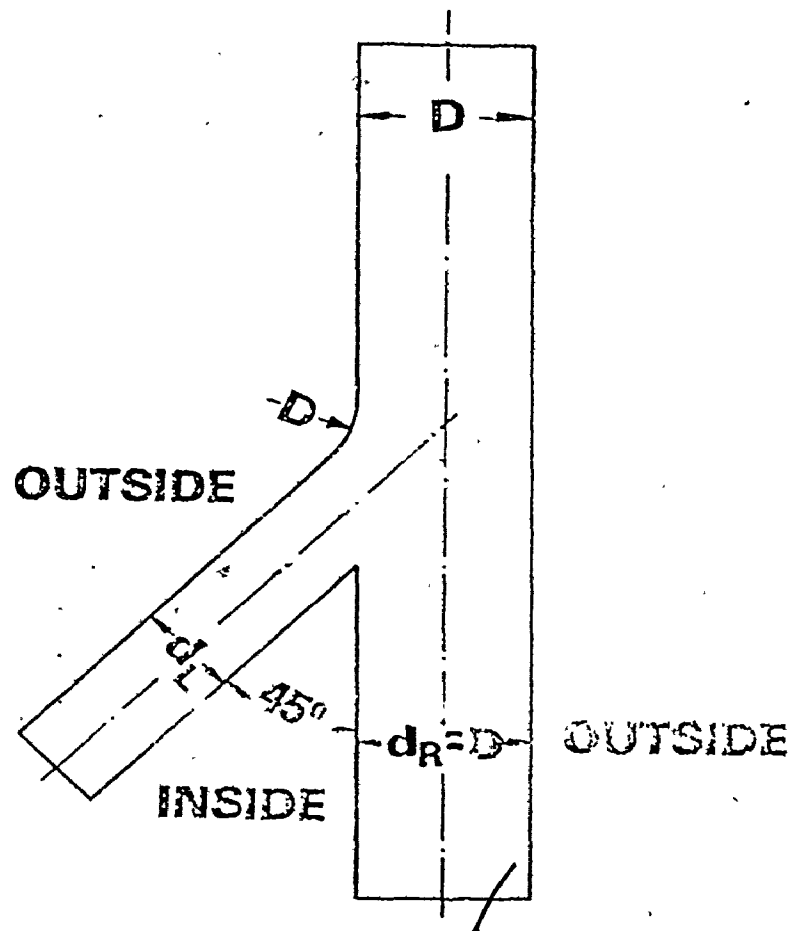
MODEL 3

45° — BRANCH

Figure 2.4   Geometrical Characteristics of Model 3
             (Dimensions are given in Table 2.1).
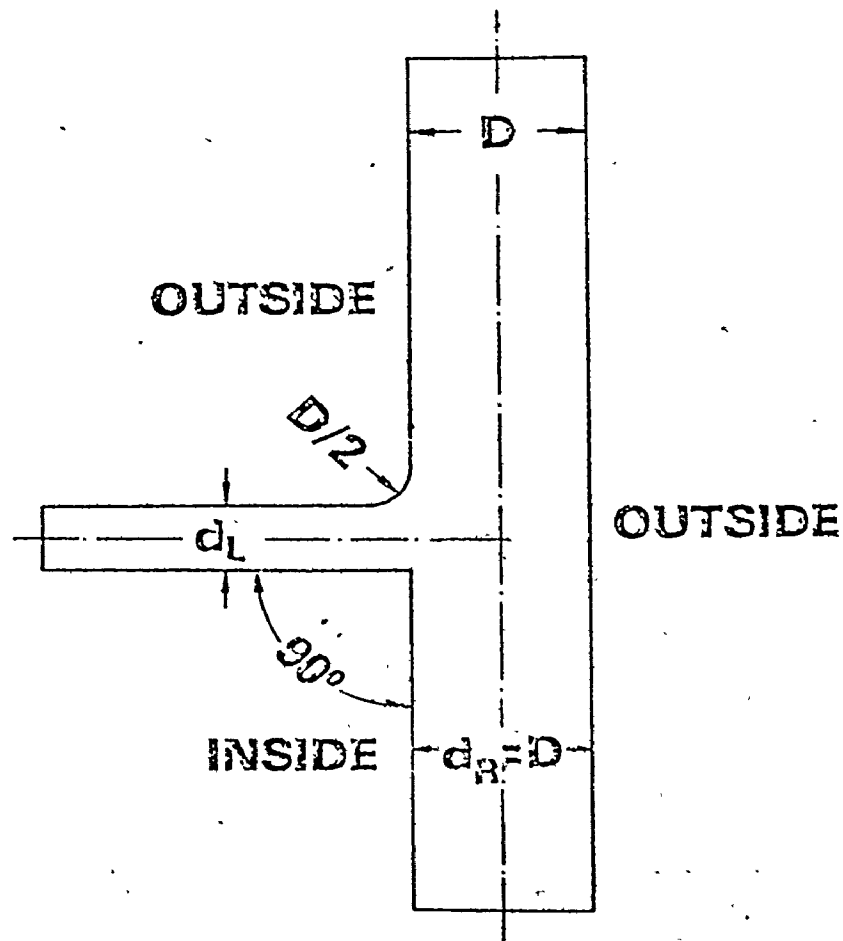
MODEL 4

90°—BRANCH

Figure 2.5   Geometrical Characteristics of Model 4
(Dimensions are given in Table 2.1).

and this was secured in the construction of the model by taking
the take-off angle equals to 90°. The diameter of this artery
was chosen to comply with anatomical measurements made by Caro
et al, [3], and the author's own measurements from the
angiograms. The models were machined from blocks of clear
acrylic plastic "Perspex". Powered drilling operations were
used along with manual forming to shape the transition sections.
Clear transparent specimens resulted after polishing. The
accuracy of the machining operations was checked by comparing
projected cross-sections of the models from cine films with
the design drawings. Deviations of less than 0.05 cm were
found. Rigid plastic tubes of length 15-20 diameters having
diameters equal to those of the models were attached.

2.4 Experimental Apparatus

In order to study the fluid dynamic aspects of flow
in the arterial models described in the previous section, an
experimental apparatus was designed to provide for both steady
and pulsatile flow of fluid within the required range of
Reynolds number. Materials and parts used in the construction
of this flow system were selected to be able to handle two
different fluids. A fluid suspension of particles (tracer-
particle technique, section 3.2) and a chemical solution (electro-
chemical technique, section 5.5) were both used in two different
applications as circulating fluids.

The apparatus, shown diagramatically in Figure 2.6,
consists of the following components:-

Description of Symbols Used in Figure 2.6

A   Model

B   Control Valve

C   Rotameter

D   Pulsation Damper

E   Speed Control Unit

F   Motor

G   Pump

H   Rotameter

I   Mixing Chamber

J   Scotch-yoke Pulsatile
     Flow Generator
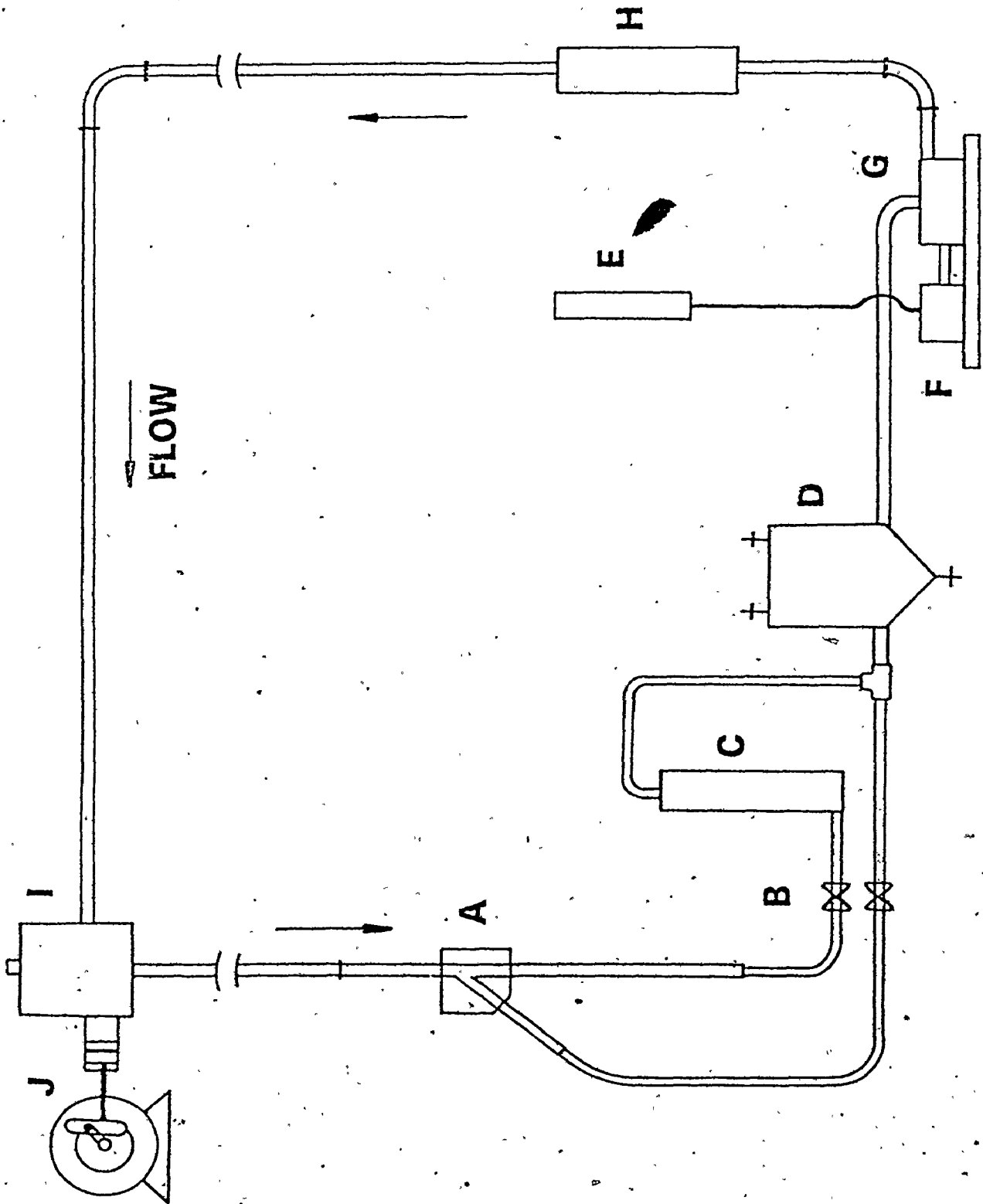
Figure 2.6   Schematic Diagram of Flow System

1. Steady Flow Motor-Pump Unit

A positive displacement Moyno type pump (SSF pump), G, was used to provide for a smooth continuous steady flow through the system. The pump was driven by a 1/2 h.p.-D.C. motor, F, with a 110-V SCR speed control, E.

2. Flow Measurement and Flow Control

Flow rates were monitored with two rotameters (Brooks O-Ring-Seal Rotameters model 1307-08C), H and C, calibrated to have an accuracy of $\pm$ 2% of the maximum reading. They were placed downstream from the pump and downstream from one of the model's daughter tubes (the larger daughter tube usually). Flow resistance in each daughter tube was controlled by screw-clamps, B, on a section of the plastic tubing, as recommended by Knox [12]. Smooth variations in flowrate were obtained with these valves.

3. Mixing Chamber

In order to provide homogeneous mixing of the particle suspension (in the case of the tracer particle suspension) and remove any small scale fluctuations which might be produced by the steady flow pump, a "Prespex" cylinder, I, was used with stainless steel wire mesh (1/16" mesh size). The cylinder has a provision in the base for a long stainless steel tube (160 cm). The tube served as an extension for the model parent tube with the same inner diameter (2.2 cm). The length of the tube was sufficient to allow the development of a Poiseuillean

velocity distribution (in the case of laminar flow) just
upstream of the model.

4.   Pulsation Damper

In order to remove the pressure fluctuation and damp
it downstream from the test section, tank (D) was used. The
air cushion (nitrogen in the electrochemical application) on
the top of the liquid in the tank worked as a damper.

5.   Pulsating Unit

Pulsatile flow was obtained by means of a piston acting
on the fluid within the mixing chamber upstream of the test
section. The piston was powered by a variable speed D.C. motor
through a scotch-yoke mechanism. By varying the main pump total
flowrate and frequency and amplitude of the piston, a wide range
of mean flowrates, frequencies and amplitude ratios was obtain-
able.

2.5   Flow Parameters

The dimensionless fluid-mechanical parameters that
govern the study of steady and pulsatile arterial flow are:

1.   Reynolds number (Re)

It is convenient to designate total flowrate in the
inlet section of the model parent tube in terms of Reynolds
number, a dimensionless quantity which gives an indication of
the relative contribution of fluid inertial forces and fluid

viscous forces upon the flow of the fluid.

Reynolds number is defined as

$$Re = \frac{\rho \bar{u} D}{\mu}$$

where $\bar{u}$ is the average fluid velocity; D is the tube
diameter, ρ is the fluid density and μ is the fluid viscosity.

For blood flow in the human aorta and its branches,
Reynolds number can be determined from the following physiological data:

Relative blood viscosity	3.5-4
Blood density	1.05 gm/cm^3
Diameter of the aorta	1.9-2.4 cm
Mean blood velocity	32 cm/sec

This results in a value for the aortic Reynolds number
in the range of Re = 1600-2300.

2. Branch Flow Ratio (σ)

Variations in local blood flowrate to meet variations
in local requirements of different parts of the body have been
known to physiologists for some time [43, 44]. The "borrowing
and lending" mechanism suggested by DeBakey et al. [45] explains
that these variations are caused by the control and regulation
of the vascular bed, which permits an increase in the blood
supply to one part of the body with a simultaneous decrease in
the volume of blood in other parts. This variation in the local
blood flowrate does not, however, involve any alteration in the
total blood volume.

In the average normal individual, the factors which may produce changes in the local blood supply to a certain part of the body are: (1) change with the physical and chemical activities of the part, (2) relation of the part to the heart level, (3) interruption of the sympathetic pathways to the part, and (4) general psychic state of the individual.

Exercise and digestion are two examples of conditions under which redistribution of blood flow occurs [44, 46]. Development of an infection in a part or organ of the body is another situation under which blood is shifted into this part at the expense of other parts of the body with less urgent demand.

For an arterial junction, the way in which the flow divides between the branches downstream is subjected to the local needs of the parts supplied through these branches and controlled by the resistance of the vascular bed of these parts.

The branch flow ratio is defined as

$$\sigma_i = \frac{Q_i}{Q_t} \, , \quad 0.0 \le \sigma_i \le 1.0$$

where Q_i is the flowrate in the branch designated by i and Q_t is the total flowrate in the parent tube. In this study, the range for the parameter σ_i was extended from its physiological range for a better understanding of its effect.

3. Unsteadiness Parameter (α)

The pulsatile blood flow in the human aorta can be

approximated by a Fourier series [47, 48]. The first harmonic, a sine wave having the frequency of the heart beat, is the largest in magnitude and the most important among the oscillatory components. In this study, the pulsatile flow in the models was approximated by the sum of a steady component and the first sinusoidal harmonic. This enabled the investigation of the effect of frequency and amplitude of pulsation on the flow patterns in a simple yet, physiologically representative way.

The unsteadiness parameter (α) is defined as

$$\alpha = R\sqrt{\frac{w}{\nu}}$$

where R is the tube radius, w is the frequency of oscillation and ν is the fluid kinematic viscosity.

The experimental value for α was chosen to be in the physiological range of $\alpha = 8\text{-}18$.

4. Velocity Amplitude Ratio (λ)

The amplitude of the oscillation is another characteristic parameter of the pulsatile flow. The velocity amplitude ratio (λ) is defined as

$$\lambda = \frac{u'}{\bar{u}}$$

where u' is the peak to peak amplitude velocity and $\bar{u}$ is the mean velocity.

Kuchar and Scala [49] reported the physiological range of λ in large arteries to be $1 < \lambda < 2$.

CHAPTER 3

FLOW VISUALIZATION STUDY: APPROACH

3.1   Theoretical

The purpose of flow visualization study in the present work was to give a clear picture of the nature of both steady and unsteady flow patterns in the arterial shapes described in the previous chapter and to study the variations in these patterns under different flow conditions, i.e., total flow rate and branch flow ratio. It was also desired to study the flow separation phenomenon in the models and quantitatively characterize its occurrence.

3.1.1   Flow Patterns

Complete mathematical analysis of flow patterns and velocity field in three-dimensional complex geometries such as those of the models under consideration, are currently beyond the capabilities of modern computers and mathematical know-how. Only experimental tools such as the hot-wire anemometer and laser doppler anemometer and techniques such as flow visualization and electrochemical measurements can provide useful information concerning the flow field. Flow visualization techniques are widely used in defining flow patterns in complex geometries in both steady and unsteady

flows.

In steady flow, since there is no change in the direction of velocity in the flow field, streamlines are fixed in space. A particle always moves tangentially to the streamline. Hence, in steady flow the path of a particle is a streamline.

In unsteady flow, since the direction of the velocity vector at any point may change with time, streamlines may shift in space from instant to instant. A particle then follows one streamline one instant, another one the next instant, so that the path of the particle may have no resemblance to any given instaneous streamlines. The use of high speed cine photography enables taking photographs of the streaks made by the particles in a short time interval. Tracing on the projected film continuous lines that have the direction of the streaks at every point portrays the instantaneous streamlines for any instance for unsteady flow.

In order to understand the complicated nature of flow in the three dimensional arterial models, it is essential to start by defining the flow patterns in these geometries. Flow through a branch is characterized by different unusual flow phenomena resulting from its three-dimensional nature. Flow cross-over phenomenon [16, 50] and the tendency to form pairs of helical counter-rotating vortices [13] are two of the important fluid motions to be studied.

3.1.2 Boundary Layer Separation: Steady Flow

When flow occurs over any surface, the fluid adjacent
to it is brought to rest because of the frictional stresses
exerted upon the fluid by the surface. Layers further
from the surface also have their velocity reduced by these
stresses. The reduction being less the further the layer is .
situated from the boundary. Due to these variations in
velocity, the fluid near the boundary has low momentum, but
the fluid momentum increases rapidly towards the core of the
flow and away from the boundaries.

For small viscosities (large Reynolds numbers), the
viscous effects are important only in the immediate vicinity
of the boundary of a solid. This immediate region is generally
referred to as a boundary layer. In that layer the velocity
of the fluid increases from zero at the wall (no slip) to its
full value which corresponds to external frictionless flow
[51].

The phenomenon of boundary layer separation is intimately
connected with the pressure distribution in the boundary
layer. For flow against a positive pressure gradient, the
fluid near a boundary, having low momentum, may rapidly be
brought to rest under the action of such a gradient. Beyond
this stagnation point (separation point) its flow will be
reversed. Boundary layer separation is always associated
with the formation of vortices and with large energy losses in
the wake behind the separation point. : For internal flows,
such a positive pressure gradient can occur in divergent

channels, in a bend and at branching sites. These geometries
are present in the arterial system in the human body and
there is a distinct possibility that flow separation can occur
within this system where local adverse pressure gradients may
exist.

3.1.3 Boundary Layer Separation: Unsteady Flow

In oscillating flows, the steady flow description of
separation is no longer meaningful. In such flows the
character of the boundary layer at any spatial location
varies as a function of time-with the cyclic component of the
flow. Hence, no single velocity profile can be associated with
a given point on the surface. Despard and Miller [52] have made
extensive measurements of instantaneous velocity profiles in
oscillating boundary layers subject to adverse pressure
gradients. The results of their study have shown that flow
separation in an oscillating stream is characterized by the
existence of an axial location (separation point), immediately
downstream of which there is reverse flow near the wall surface
over the entire pulse cycle. The same study and other
theoretical work by Schneck and Ostrach [53] have shown that,
in a pulsatile flow situation, the flow separates upstream
of where it would in a corresponding steady flow situation
and that the separation point in the unsteady case moves
downstream, towards its steady flow location, as the frequency
of oscillation is progressively increased.

These factors also influence flow separation in the

arterial system where local adverse pressure gradients may exist over the cardiac cycle. The present knowledge on the separation in the major central arteries under pulsatile flow conditions is by no means well developed, and further research is necessary to determine the extent of this local flow phenomenon in the arteries of man.

3.2   Experimental

3.2.1 Neutrally-Buoyant Tracer-Particle Technique

Techniques for defining fluid motions are numerous. They may be used for both quantitative evaluation of velocities and qualitative determination of streamlines. In the latter category, dye injection, smoke tracers, hydrogen bubbles and polymer tracer particles have proven useful for a variety of applications. In this study, a neutrally-buoyant tracer particle system similar to others used by Feuerstein and Woods [54], Pike [55] and El Masry [17] was utilized with cine photography to study the flow patterns and boundary layer separation phenomenon in the experimental models. In this technique, a fluid suspension of particles having the same density of that of the carrier fluid is used. These particles when photographed give the suspending fluid path-lines, provided that:

a)   the particle size is small relative to the vessel size

b)   there is no or at most a small difference in density between the suspending fluid and particle and

c) the particle concentration is low.

In order to use neutrally-buoyant particles as tracers in complex flows, one must determine if these particles can be considered to be replacements for the fluid particles and that the presence of these particles does not alter the homogeneity of the carrier fluid. There exists both experimental data and theoretical solutions for the motion of suspended spheres in well defined flows which provide criteria for judging when this alternative becomes significant (Appendix B). In fact, the ratio of particle radius to tube radius and the ratio of particle radius to distance from the wall are important dimensionless groups for describing the deviation between particle velocities and fluid velocities. Feuerstein and Woods [54] have shown that results which do not vary with particle size do not contain errors due to the presence of particles, assuming a particle-size ratio of at least 2. Using particle sizes (100-300μ) in tube radius of 1 to 2 cm, both El Masry [17] and Pike [55] have shown that particle inertia effect was negligible for the range of Reynolds number (200-1200).

3.2.2. Particle Suspension

The composition and physical properties of the suspending medium are detailed in Table 3.1. Polystyrene particles of size range 100-300μ were present at a concentration of 10 particles/ml and were neutrally buoyant in the suspending fluid. There was a difference in refractive indices between the perspex of the model (1.4812) and the

TABLE 3.1 Composition and physical properties of suspending fluid.

Composition by volume per 1 litre of water	Composition by weight per 1 litre of water
142 cc of glysrol	180 gm of glysrol

Physical properties at 20°C		
Density gm/cm^3	Refractive index	Viscosity Centipoise
1.042	1.3552	1.528

suspending fluid (1.3552). This resulted in some optical distortion which was not considered important for the qualitative observation of the particle paths (Appendix C).

3.2.3 Optical Equipment

(1) Cine Camera

(2) Illumination System

(3) Photo-Optical Data Analyser

(1) Cine Camera

Photographic information was obtained with the aid of a high speed motion picture camera (Lo Cam 51-0003, Red Lake Laboratories, Red Lake, Calif.). The model used was a 16 mm intermittent pin-registered camera controlled by solid-state electronics for an accuracy of $\pm$ 1% or 1 frame, whichever is greater. The camera has a frame rate range of 16-500 frames/sec.

A 55 mm f-2 Asahi Pentax lens with extension tubes was used to provide an image for continuous recording of particle movement within the models. The region of the flow field that was of experimental interest extended from a few diameters upstream of the model carina to about 5 diameters into the daughter tubes.

The film used was Eastman Kodak Double-X Negative 7222 on 100 feet reels.

(2) Illumination System

Two different systems of illumination were used for two

different applications; the streamline observation and the study of flow separation. In the first system, diffuse back illumination was provided by directing two Westinghouse 1500W, 208V, tungsten halogen lamps equipped with parabolic polished-aluminum reflectors, through translucent photographic papers into the back of the test section. Precautions were taken to avoid unwanted reflections by appropriate direction of the lamps and placement of the photographic papers.

Due to the fact that rays of light issuing as a cone from the above mentioned lamps are twice refracted at curved surfaces which may result in light distortion especially for these particles close to the wall, a second system of lighting was used to study the boundary layer separation and the particle movement close to the wall. In this system, a strong point source of light was provided by a 100W carlson lamp which was placed at the focal point of a 15 cm focal length, plane convex lens to produce a parallel beam 5 cm in diameter. The object was illuminated by two such beams, one from the side and one from the rear, intersecting at right angles.

(3) Photo-Optical Data Analyser

Film analysis was carried out with the aid of an L.W. Photo Inc. Photo-Optical Data Analyser (model 224-A), which was set up in a specially constructed rig to allow back-projection onto a transparent screen. The frame rate could be set to any of several different settings (2-24 f.p.s); or the films could be projected frame by frame.

3.2.4 Photography

For streamline observation, high speed photography
was used to provide an image for continuous recording of
particle movement within the models. Particles were
followed from a position within the parent tube where Poiseuille
flow (parabolic velocity profile) existed to positions
approximately 5 diameters into the daughter tubes. Since the
fluid entering the daughter tubes divided and since secondary
flows (flows not parallel to the centre line of the conduit)
existed, it was of interest to select streamlines emanating from
a number of positions within the parent tube and follow them
into the daughter tubes. These streamlines and their respective
positions within the parent tube were labelled with numbers
from 1 to 8. Figure 3.1 shows the approximate positions of the
selected streamlines within the parent tube cross-section.
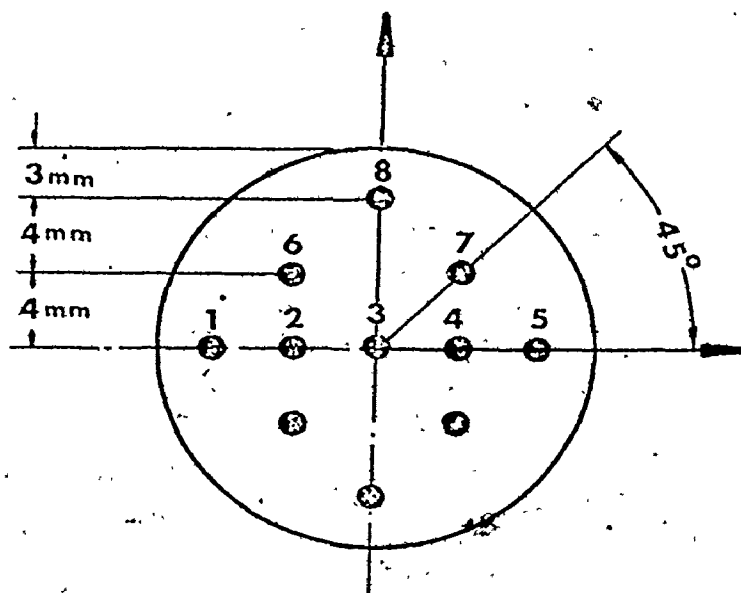
Figure 3.1   Approximate Positions of the Selected Stream-
lines within the Parent Tube Cross-section.

Within the parent tube, particles near the median
plane were located by focussing on this plane using a lens
configuration of small depth of field. Particles from other
parent-tube positions were located, after filming with a large
depth of field, through their linear velocity since they were
in a symmetrical parabolic velocity profile having a defined
relationship between radial position and local velocity.

Photographic data were obtained for flows in both
laminar and turbulent regimes (Re = 900-3000). Although it
is strictly speaking improper to speak of a "streamline" in
connection with turbulent flows, the particle motions observed
at high flow Reynolds numbers did not display perturbations
perpendicular to the particle's main path which would be
characteristic of turbulence. This may be due to either the
absence of local turbulence at these values of Reynolds number
or to a scale of turbulence which was small with respect to the
particles' size, 100-300 μm. Thus, particle paths were
referred to as streamlines throughout the presentation of the
results (Chapter 4).

Data concerning flow separation and the size of separa-
tion vortex (Section 4.2) were obtained from cine films taken
by focussing the lens on the median plane at a region close
to the wall. Downstream of the separation point, particles
near the wall moved slowly in a reversed flow direction. They
were brought to a standstill at the separation point before
they moved laterally away from the wall and then rapidly resumed
forward motion.

CHAPTER 4

FLOW VISUALIZATION STUDY:
· RESULTS AND DISCUSSION

4.1   Steady Flow Patterns

· The results of the steady flow pattern observations
are presented in this section in the form of drawings of
streamlines to indicate the relative importance of vessel
geometry, flow rate (Reynolds number) and branch flow division
ratio upon flow paths and formation of separated flows.
Individual vessel flows are designated as Q_L, Q_R and Q_t
with L and R referring to the left and right branches (from
the viewpoint of the observer) and t total flow in the parent
tube.

The streamline patterns for the four models are shown
at a common parent tube Reynolds number of 1800, see Figures
4.1 to 4.4.   Flow division in each case was made proportional
to the respective flow areas of the daughter tubes. No flow
separation was observed at these conditions, although some
reverse flow was observed on the near and far walls of
Model 3.

There existed a number of similarities in the flow
patterns for the four models. Streamlines emanating from the
median plane (plane of symmetry of the model) of the parent
tube (labelled 1, 2, 3, 4 and 5 for Models 1 and 2 and 1 and 2
for Models 3 and 4) did not follow the outside boundaries of

MODEL 1

Figure 4.1   Streamline Pattern in Model 1
Re = 1800, Q_L/Q_t = 0.5
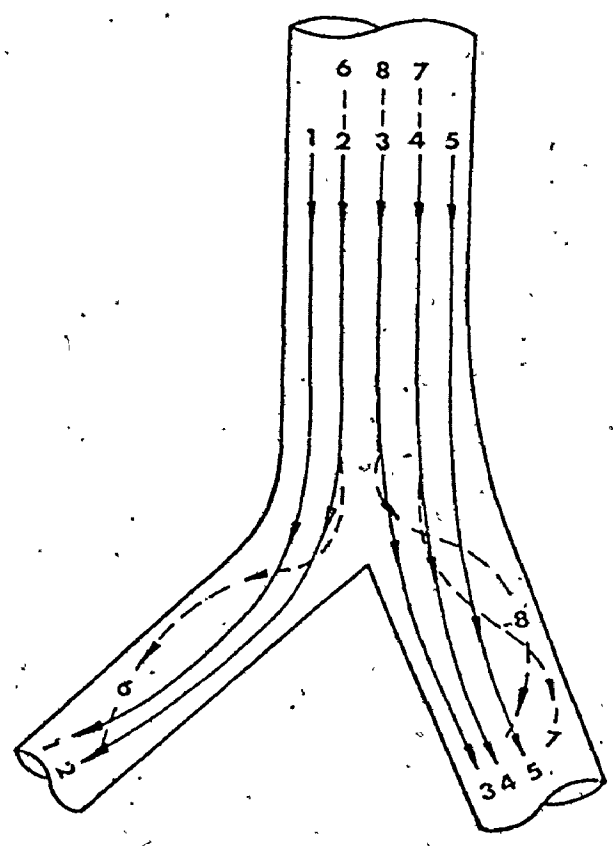
MODEL 2

Figure 4.2 Streamline Pattern in Model 2
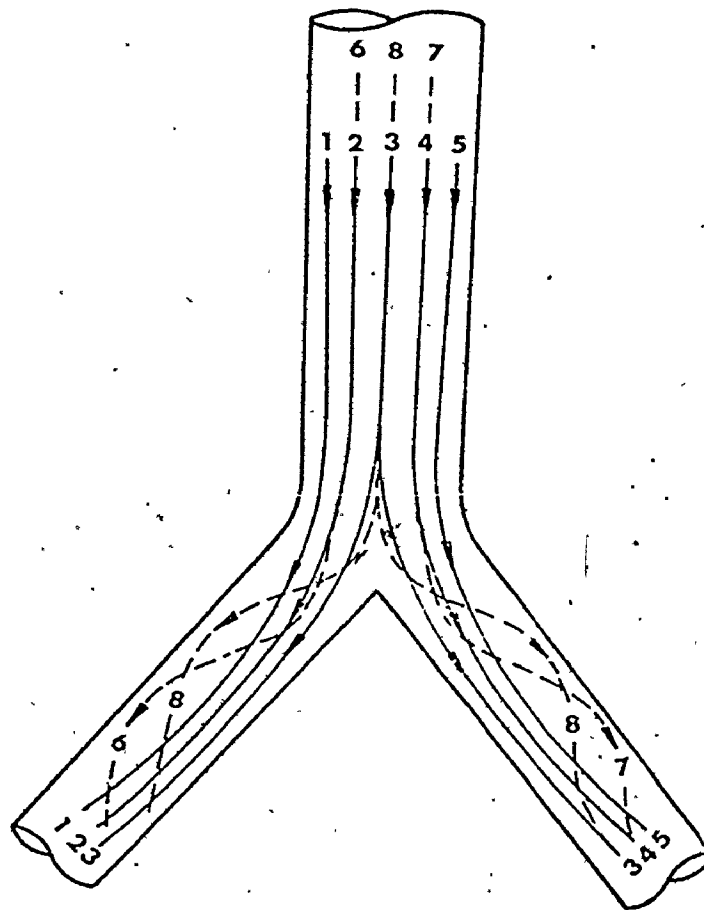Re $\approx$ 1800, $Q_L/Q_t = 0.33$
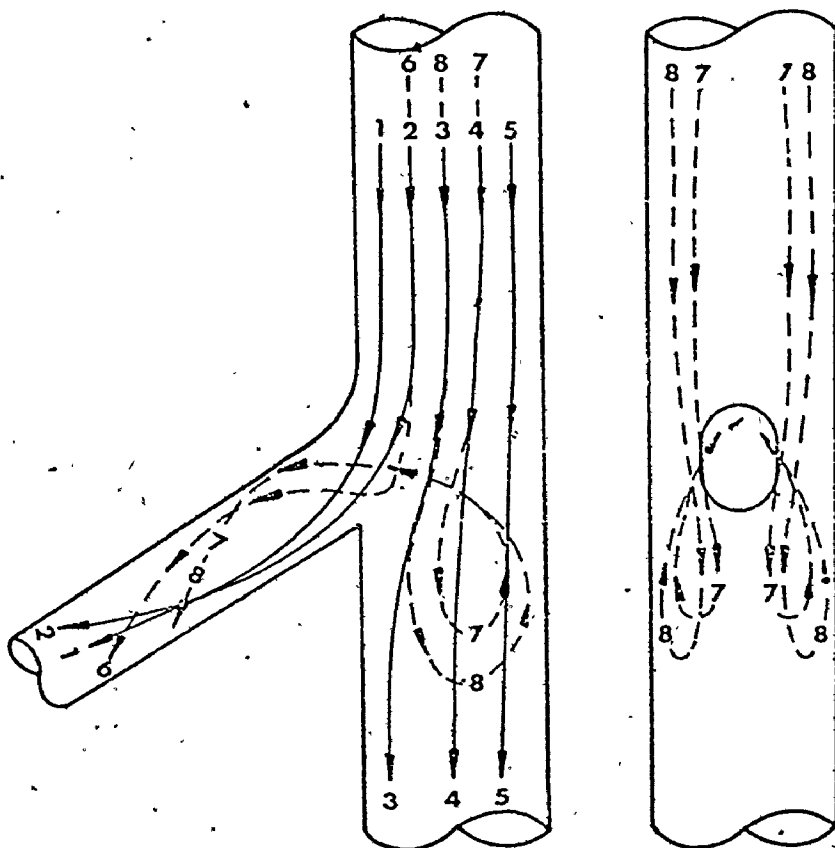
MODEL 3

Figure 4.3 Streamline Pattern in Model 3
Re = 1800, Q_L/Q_t = 0.25
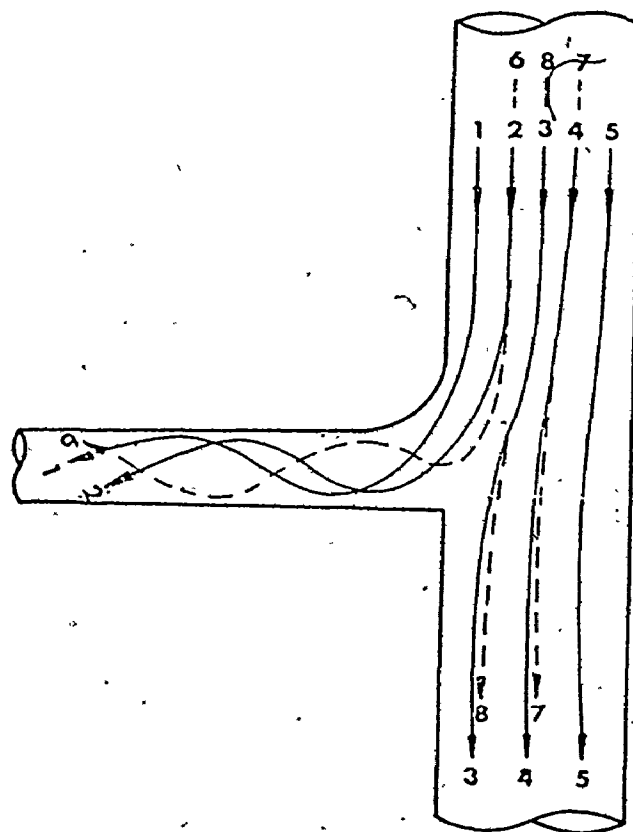
MODEL 4

Figure 4.4   Streamline Pattern in Model 4
Re = 1800, Q_L/Q_t = 0.14

the models but rather moved radially from the outside wall towards the flow divider while the distance between them was reduced upon entering their respective daughter tubes. This resulted in a flow of fluid from the daughter tube outside wall to the inside wall within the median plane and was in part responsible for the paired counter-rotating vortices observed by the author [50] and others [13, 15, 16] in the daughter tubes of symmetric bifurcations. Complementary to this motion, a group of streamlines traced from particles located on either side of the median plane (labelled 6, 7 and 8 for all models) moved from their respective positions within the parent tube to the outside of the daughter tubes. This secondary flow motion is believed to be a result of the transverse pressure gradient (inward) induced in the median plane to balance the centrifugal force caused by the outside bend at the transition section of the model [16]. Model 3 (Figure 4.3) displayed an additional characteristic in which streamlines 7 and 8 first entered the right branch (continuation of the aorta) before reversing direction and entering the daughter tube. An explanation for this phenomenon can be provided by the fact that this model (Model 3) had a large area ratio (outfow to inflow cross sectional area) of 1.33 which could be expected to set a high adverse pressure gradient on the wall of the diverging section of the models. Flow near the wall with low momentum was likely to separate and reverse its direction at moderate flowrates.

There was a change in the streamline patterns in the
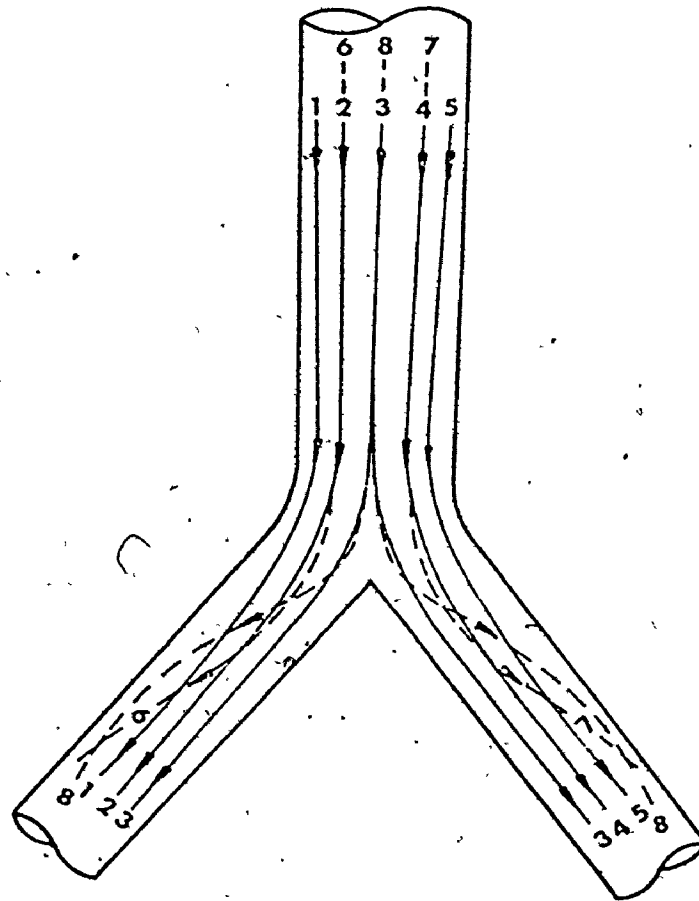
MODEL 1

Figure 4.5(a)   Effect of Varying the Total Flow Rate
on Streamline Pattern of Model 1

Re = 900, Q_L/Q_t = 0.5
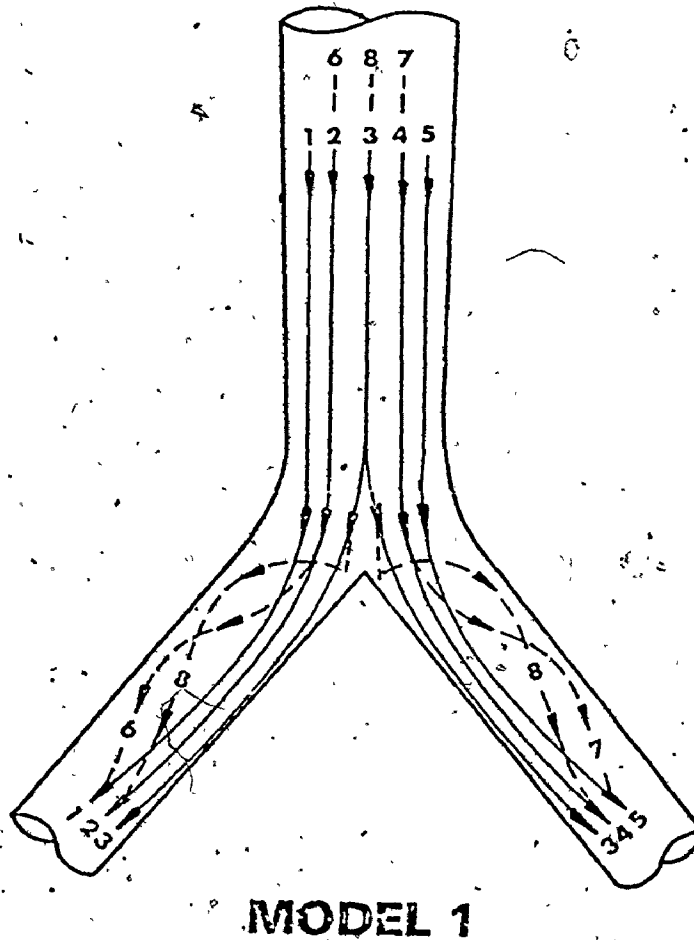
MODEL 1

Figure 4.5(b)   Effect of Varying the Total Flow Rate
on Streamline Pattern of Model 1
Re = 3600, Q_L/Q_t = 0.5

four models with an increase in flowrate (Reynolds number).
This is shown in Figure 4.5 (a, b) with Model 1 as an example.
At the higher flowrate (Figure 4.5(b), Reynolds number is
equal to 3600), streamlines 1, 2, 5, 4 and 5 were more dis-
tinctly displaced towards the flow divider than at the lower
flowrate (Figure 4.5(a), Reynolds number equal to 900).
Likewise, streamlines 6, 7 and 8, which cross from their start-
ing positions on both sides of the median plane in the parent
tube to the outside of the daughter tubes, did so furhter
upstream, i.e., closer to the daughter tube entrance, and with
an apparent increase in radial velocity component. Flow
separation was not observed at either flowrate.

Of particular interest in this study is the formation
of separated flow regions. A major shift to separated flow
was observed for the four models when the flow division ratio
was altered from those specified in Figures 4.1 to 4.4 without
changing the parent tube Reynolds number.   Two examples for
this separation phenomenon are given in Figures 4.6 and 4.7
for Models 1 and 2. When the left branch flowrates were
decreased to levels of 30 percent $(Q_L/Q_t = 0.30)$ and 15 percent
$(Q_L/Q_t) = 0.15)$ of the parent tube flowrates for Models 1 and
2, respectively, flow separation (disturbed flow) resulted in
the daughter tube with less flowrate (left branch). Separated
flow of this type could be similarly induced in Models 3 and
4 by increasing the parent tube Reynolds number while maintaining
the flow division ratio of the base case (Figures 4.3 and 4.4).
An example for these conditions is depicted in Figure 4.8 for
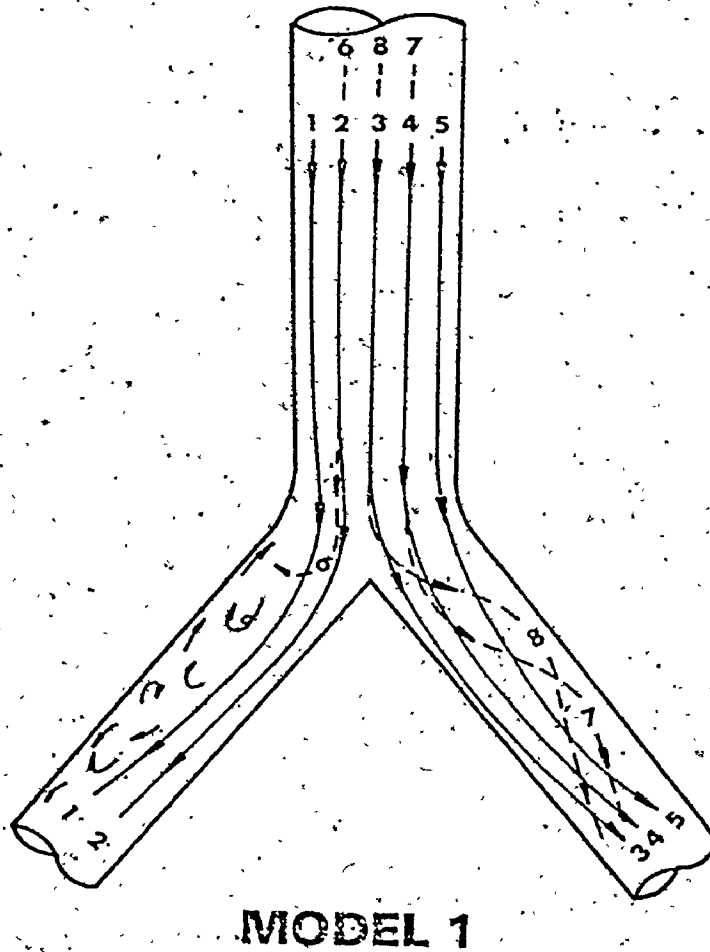
Figure 4.6   Flow Separation in the Left Side Branch
of Model 1
Re = 1800, Q_L/Q_t = 0.3
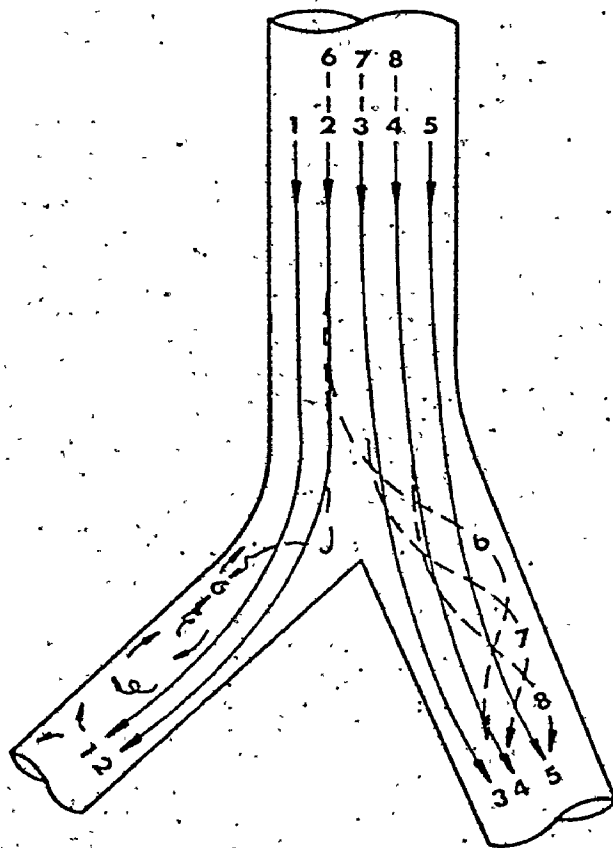
MODEL 2

Figure 4.7   Flow Separation in the Left Side
Branch of Model 2
Re = 1800, Q_L/Q_t = 0.15
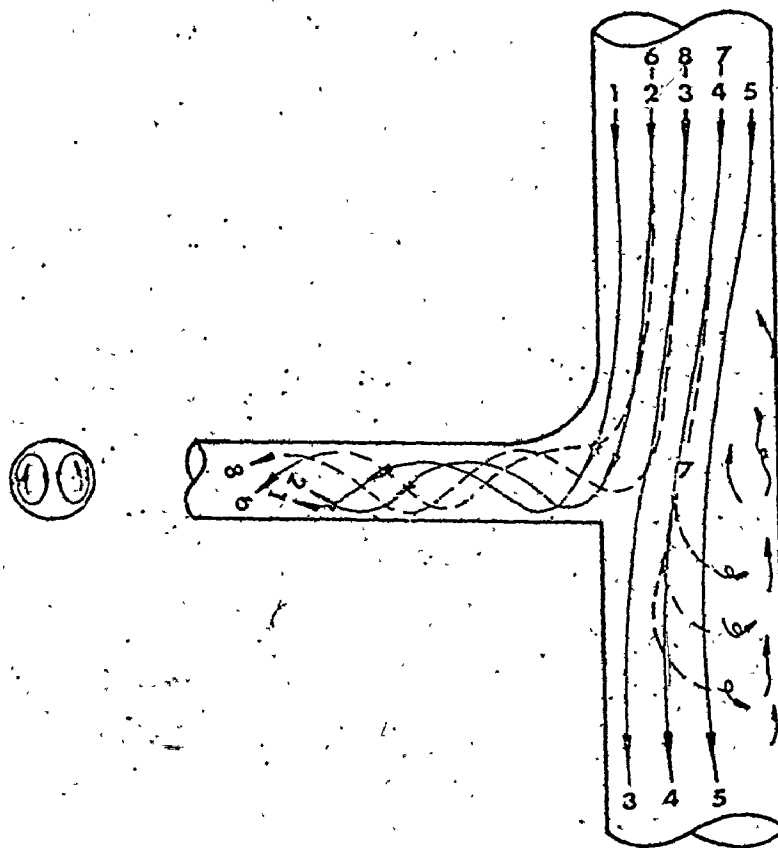
MODEL 4

Figure 4.8 Flow Separation in the Main Tube
of Model 4.
Re = 2800, Q_L/Q_t = 0.14, Q_R/Q_t = 0.84

Model 4. Here the parent tube Reynolds number was increased
from 1800 in Figure 4.4 to 2800 in Figure 4.8 while the flow
division ratio was kept the same at 0.14. Separation flow
was observed in the parent tube near the junction and in its
straight continuation (right branch) as a result of increasing
Reynolds number.

Unlike simpler two-dimensional flows which have a
single separation point with a downstream set of closed
streamlines forming a recirculating vortex [56], three-dimensional
flows, such as those described above, display a locus of
separation points creating a more complex pattern resulting in
streamlines which do not form a closed vortex. Here flows
enter and leave the vortex region having a residence time
dependent on flowrate and vessel shape. A detailed study of
these variables was not made. An additional type of flow
separation was found to exist near the carina (flow divider
point) with Model 3. A number of vascular flow studies have
characterized this region as a high shear rate area [16, 17, 32]
in which locally separated flows have not been previously
reported. In this case, an open and small vortex was observed
to form on the inside wall of the side branch (left branch)
of Model 3 for high Reynolds number (≥ 3000) and high flow
division ratio ($Q_L/Q_t = 0.6$). This vortex is shown in Figure
4.9 and marked by the letter S. The left branch of Model 2
which has the same diameter and take-off angle of that of
Model 3, did not show this type of separation vortex for flow
conditions similar to those of Model 3 where the vortex was
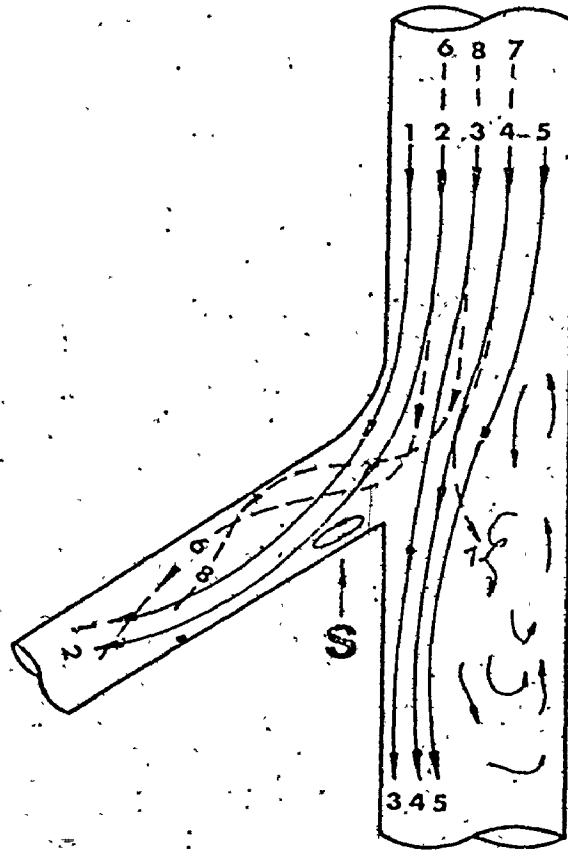
MODEL 3

Figure 4.9 Flow Separation on the Flow Divider
Wall (Marked S) Along with Separation
on the Outside of the Opposite Limb

Re = 3600, Q_L/Q_t = 0.6
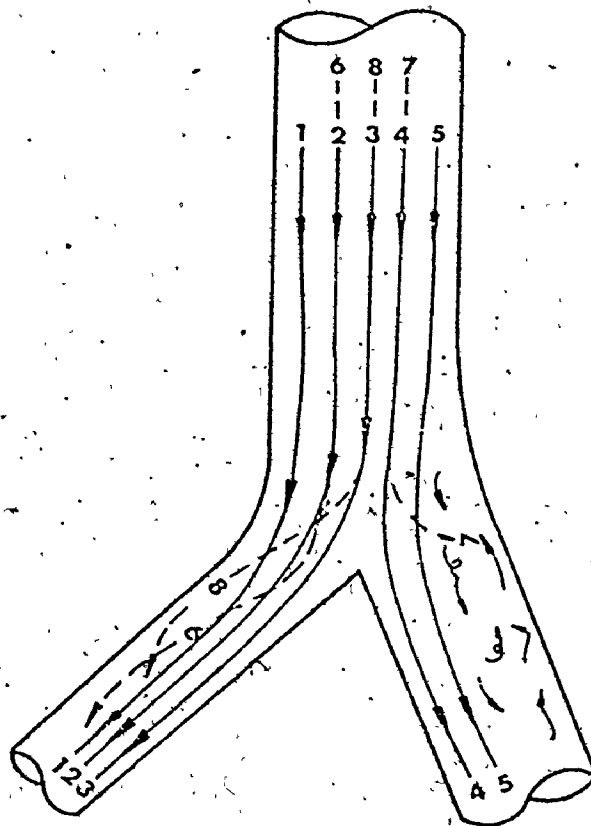
MODEL 2

Figure 4.10 Flow Separation in the Right Side Branch of Model 2. No Separation on the Flow Divider Wall

Re = 3600, Q_L/Q_t = .6, Q_R/Q_t = 0.4

observed. (See Figure 4.10) This difference in the patterns may be attributed to the difference in the area ratio of the two models (α = 1.0 for Model 2 and α = 1.33 for Model 3)..

4.2 Qualitative Study of Flow Separation

The separation phenomena described in the previous section are presented only for certain defined combinations of Reynolds number and flow division ratio. They may occur singly or in combination. Separation as a function of geometry, Reynold's number and flow division ratio was studied by filming the flow pattern near the walls of the models over a wide range of flow parameters. For a specific total flowrate (Reynolds number), the flow rates in both branches were slowly and progressively changed by means of screw clamps until a flow separation (flow reversal near the wall) was just seen to form. Flow division rates and Reynolds number were then calculated from flowrate measurements.

The information resulted from the above experiments is presented on a separate diagram for each model geometry studied and is given by Figures 4.11 to 4.14. In Figure 4.13 and 4.14, experimental data is plotted in a much more expanded scale than is used in the other two figures. The solid lines on each diagram are the best straight lines drawn through the experimental points. These lines separate areas in which different flow conditions exist. For example, zone A of Figure 4.11 is a region in which flow separation occurs on the outside wall of the left branch in the model under consideration (Model 1). This means that all of the combinations of Reynolds number and
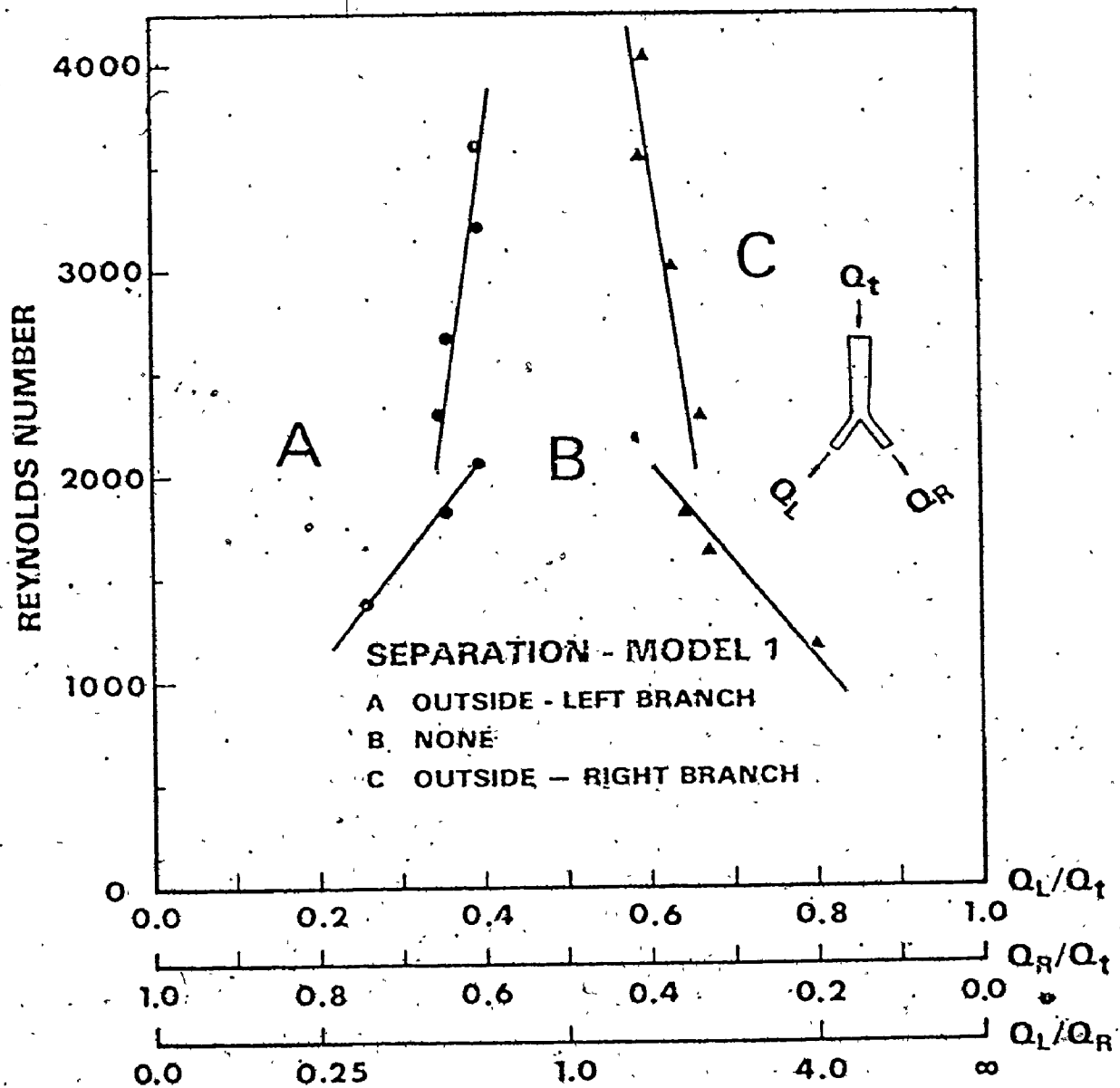
Figure 4.11 Flow Conditions for Model 1 Showing Zones of Separation and No Separation as Functions of Reynolds Number and Flow Division Ratio.
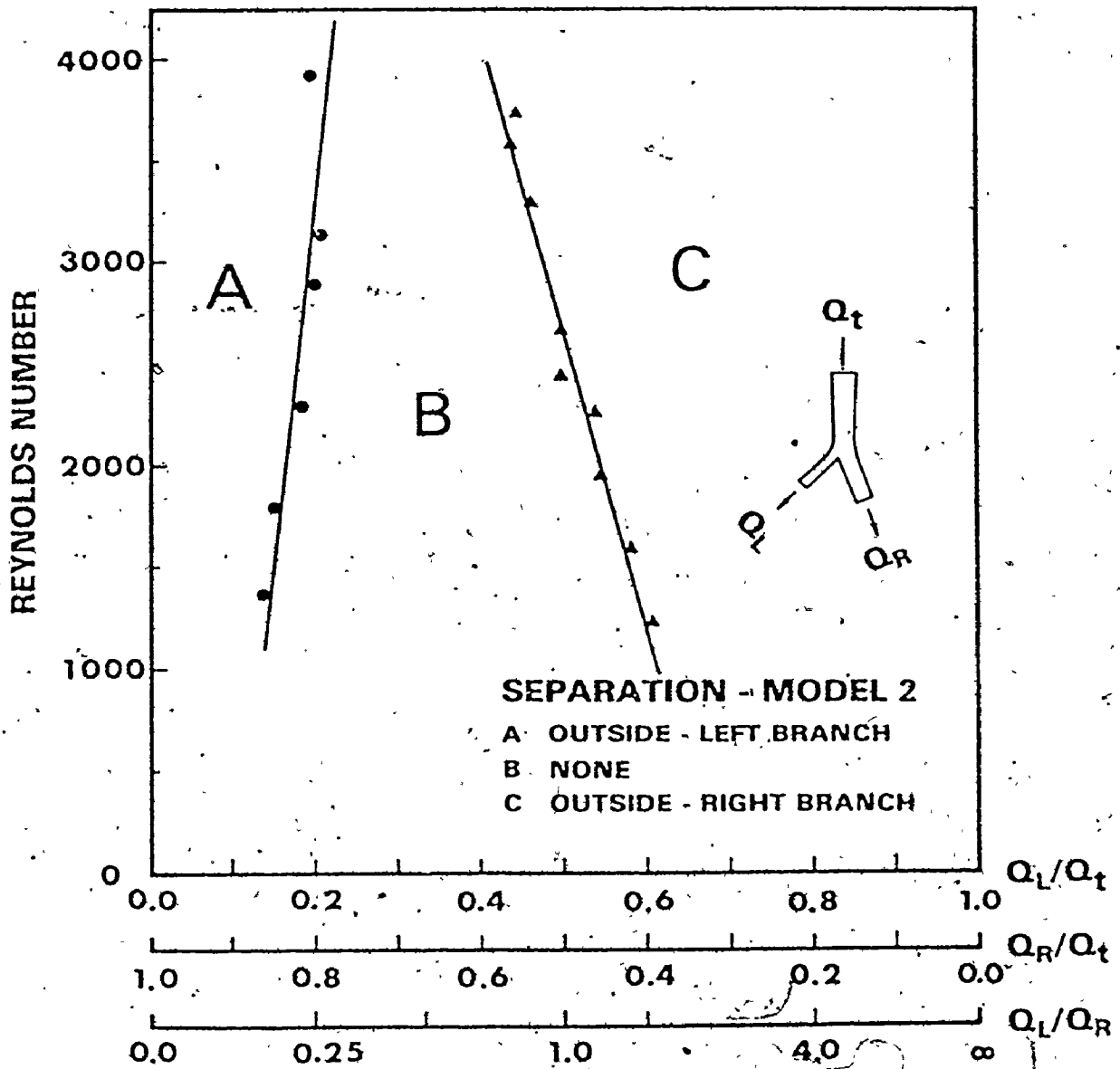
Figure 4.12   Flow Conditions for Model 2 Showing Zones of
Separation and No Separation as Functions of
Reynolds Number and Flow Division Ratio.

62
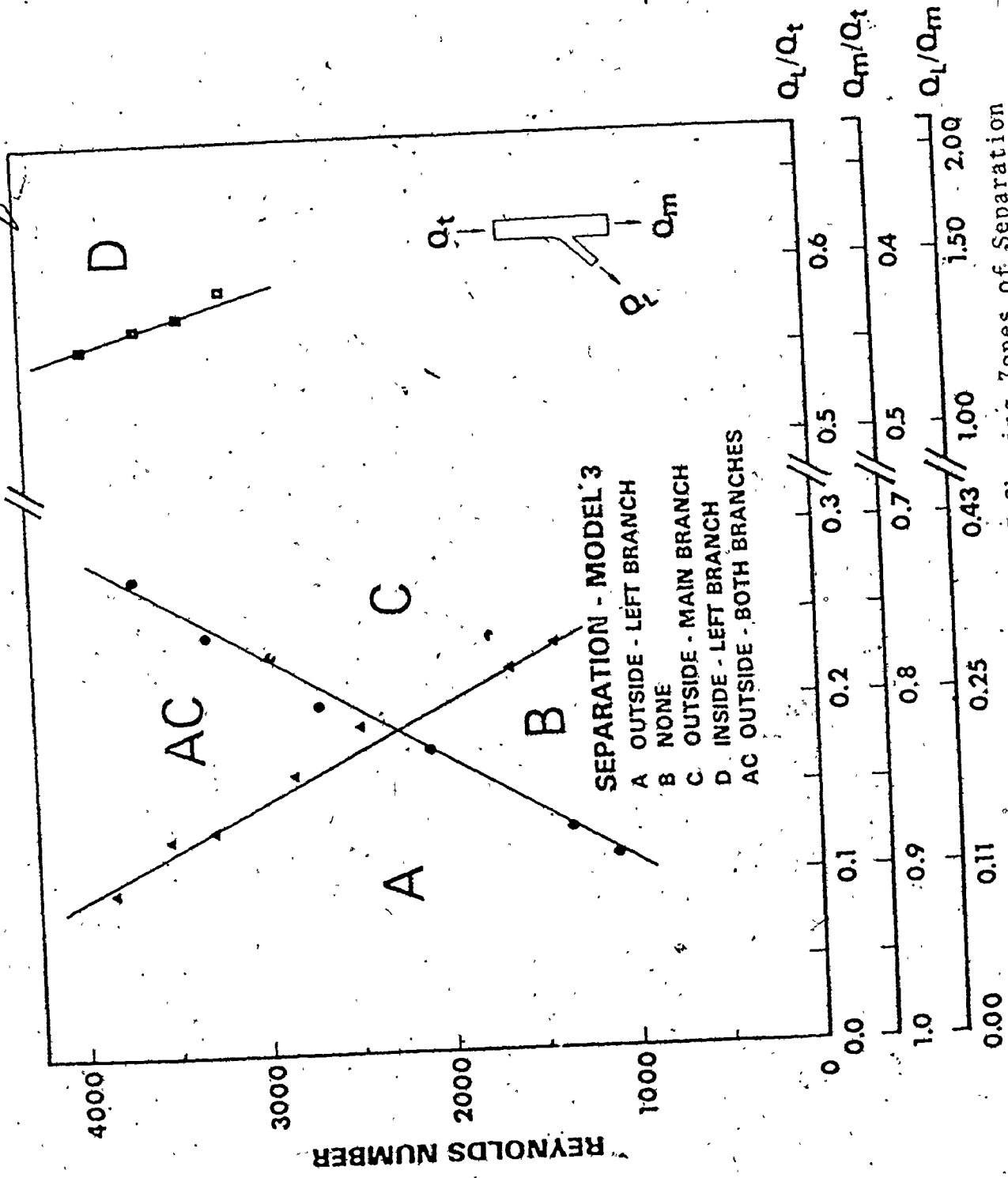
Figure 4.13 Flow Conditions for Model 3 Showing Zones of Separation and No Separation as Functions of Reynolds Number and Flow Division Ratio.
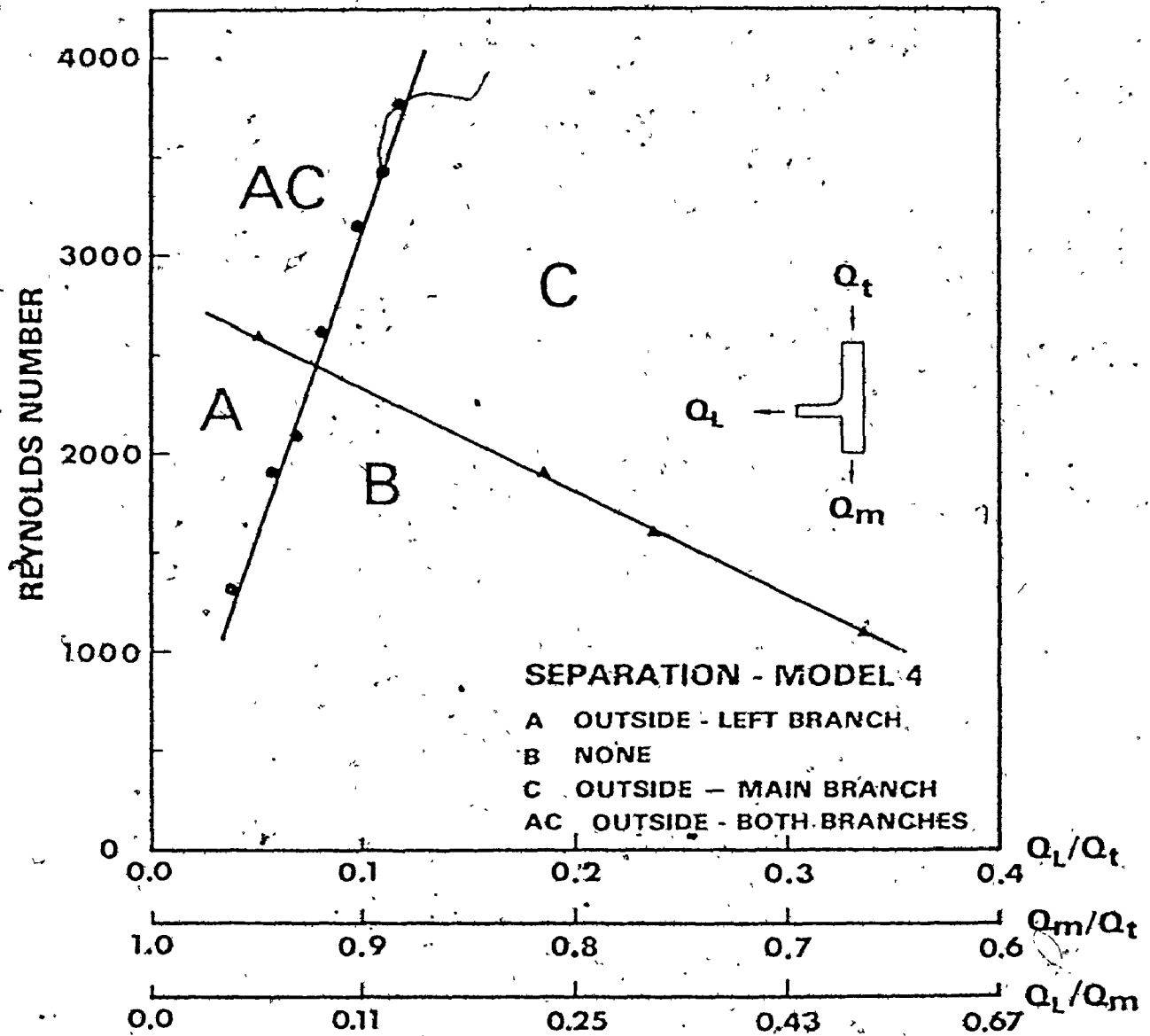
Figure 4.14   Flow Conditions for Model 4 Showing Zones of Separation and No Separation as Functions of Reynolds Number and Flow Division Ratio.

flow division ratio to the left of the lines through the experimental points, marked with closed circles (●), give separated flow.

All of the models displayed regions where no flow separation occurred. Flow separation was absent in Models 1 (Figure 4.11) and 2 (Figure 4.12) for a narrow range of flow division for all the Reynolds number range studied here (up to a Reynolds number of 4000). A change in the slope of the demarcation lines for Model 1 at a Reynolds number of 2000 (Figure 4.11) could be associated with transition from laminar to turbulent conditions where a change in the slope of wall pressure distribution is expected. However, this was not observed for Models 2, 3 and 4. Studies of Models 3 and 4 (Figures 4.13 and 4.14) indicated regions in which simultaneous flow separation was observed at the outside of both daughter tubes.

Figures 4.11 to 4.14 indicated clearly that boundary layer separation in three-dimensional branching vessels is a part of the complicated flow phenomenon in these geometries which is characterized by the secondary flow motion. This motion results from a change in the cross-sectional geometry and is strongly influenced by flow parameters. The fact that separation was observed on the outside walls of large radius of curvatures (Models 2, 3 and 4) and different branching angles [0, 20, 45 and 90°] leads to the conclusion that the details of the geometry (including branching angle shape of the flow divider and curvature of the walls are second factors leading to separation. These parameters may slightly modify the critical flow conditions leading to separation but not to alter the general trend and functionality of separation as reported here.
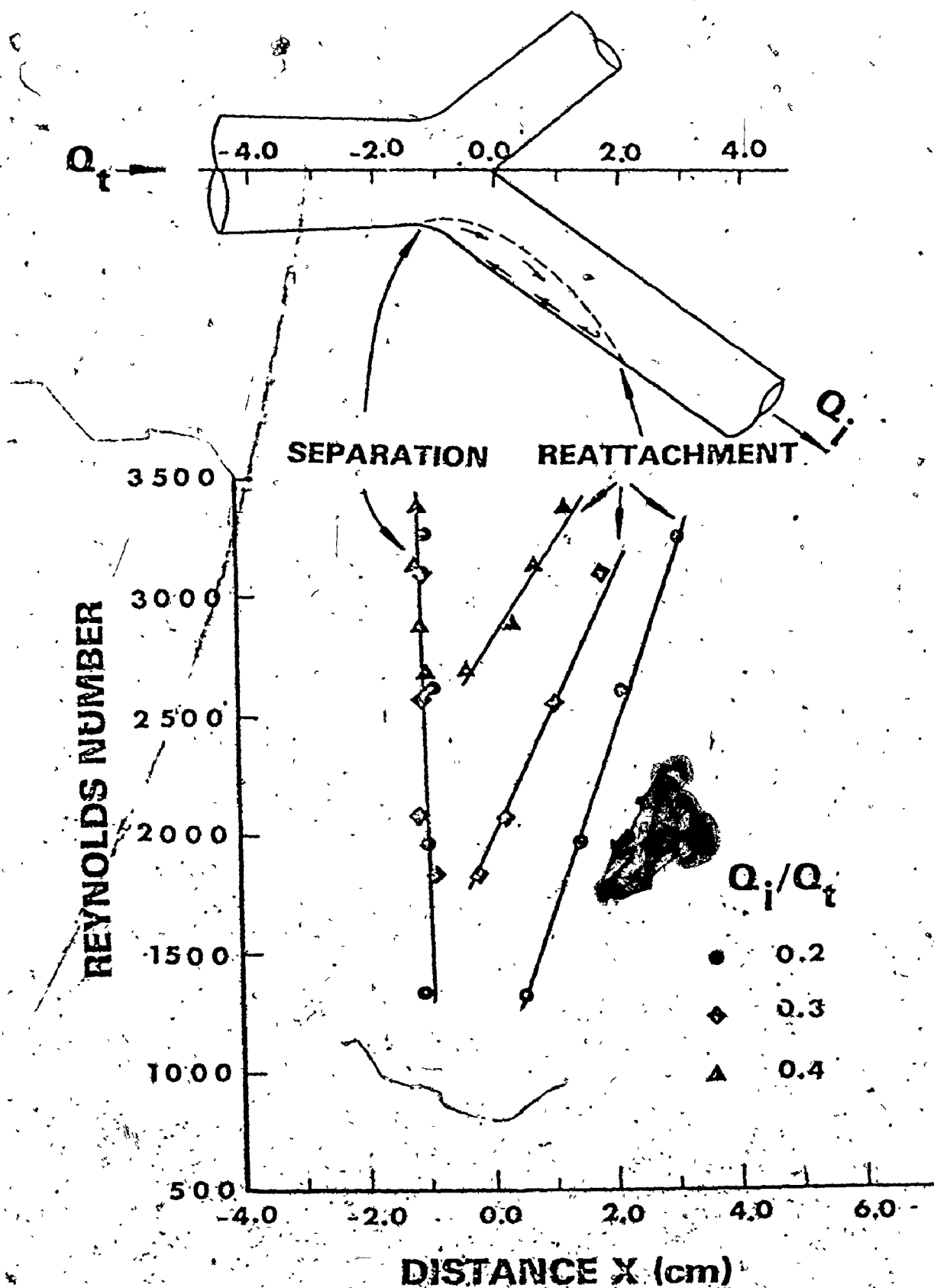
Figure 4.15 Definition of Separation and Reattachment Positions for Model 1 as a Function of Reynolds Number and Flow Division Ratio.

A complete study of the position and size of the separation vortex was made in Models 1 and 2. The separation vortices in Models 3 and 4 are similar to those of 1 and 2 and only a limited number of observations were made to determine the separation point and the extent of the separation regions in Models 3 and 4.

Although the separation vortices formed on the walls of the models are three-dimensional and display a locus of separation points, these vortices were studied in a two-dimensional plane (plane of symmetry of the model). Separation and reattachment points referred to in this section are those of the vortex in this plane.

The size of the separation vortices were found to be dependent upon Reynolds number in the parent tube and flow division ratio. Figures 4.15 and 4.16 (a, b) are plots of projected separation vortex length measured on a scale parallel to the model centreline. Length measurements were taken at the intersection of the median plane with the daughter tubes of Models 1 and 2. The sizes shown in Figure 4.15 correspond to zones A and C of Figure 4.11 while Figure 4.16(a) corresponds to zone C of Figure 4.12 and Figure 4.16(b) to zone A of that figure. The largest vortex sizes were for those flow conditions of Reynolds number and flow division furthest from the zones of no separation. It is of interest to note that the site of the separation point was approximately constant and independent of the flow division ratio. Upon increasing the Reynolds number the separation point was observed
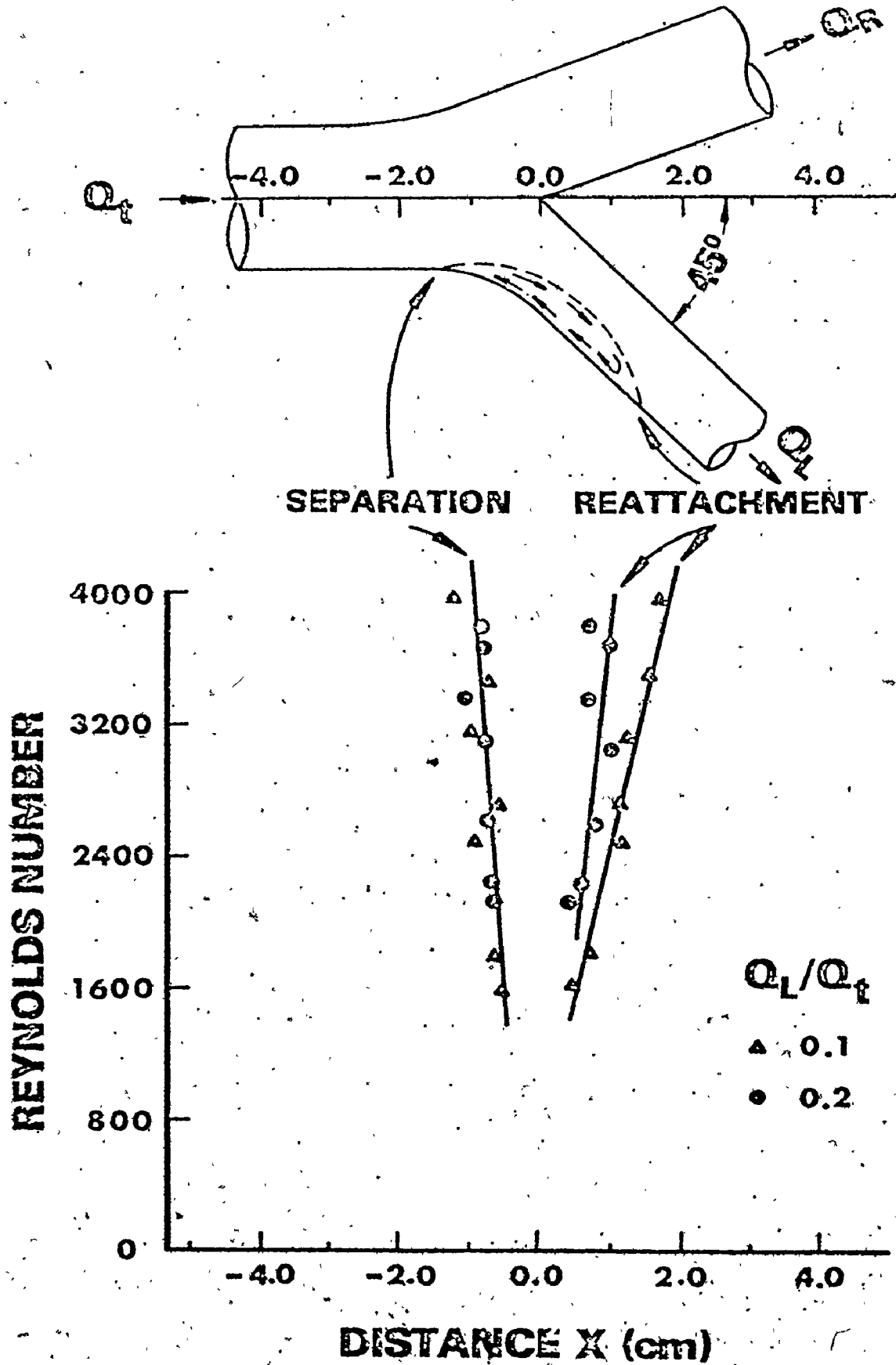
Figure 4.16(a)   Definition of Separation and Reattachment
Positions for the Left Side Branch of Model
2 as a Function of Reynolds Number and Flow
Division Ratio.
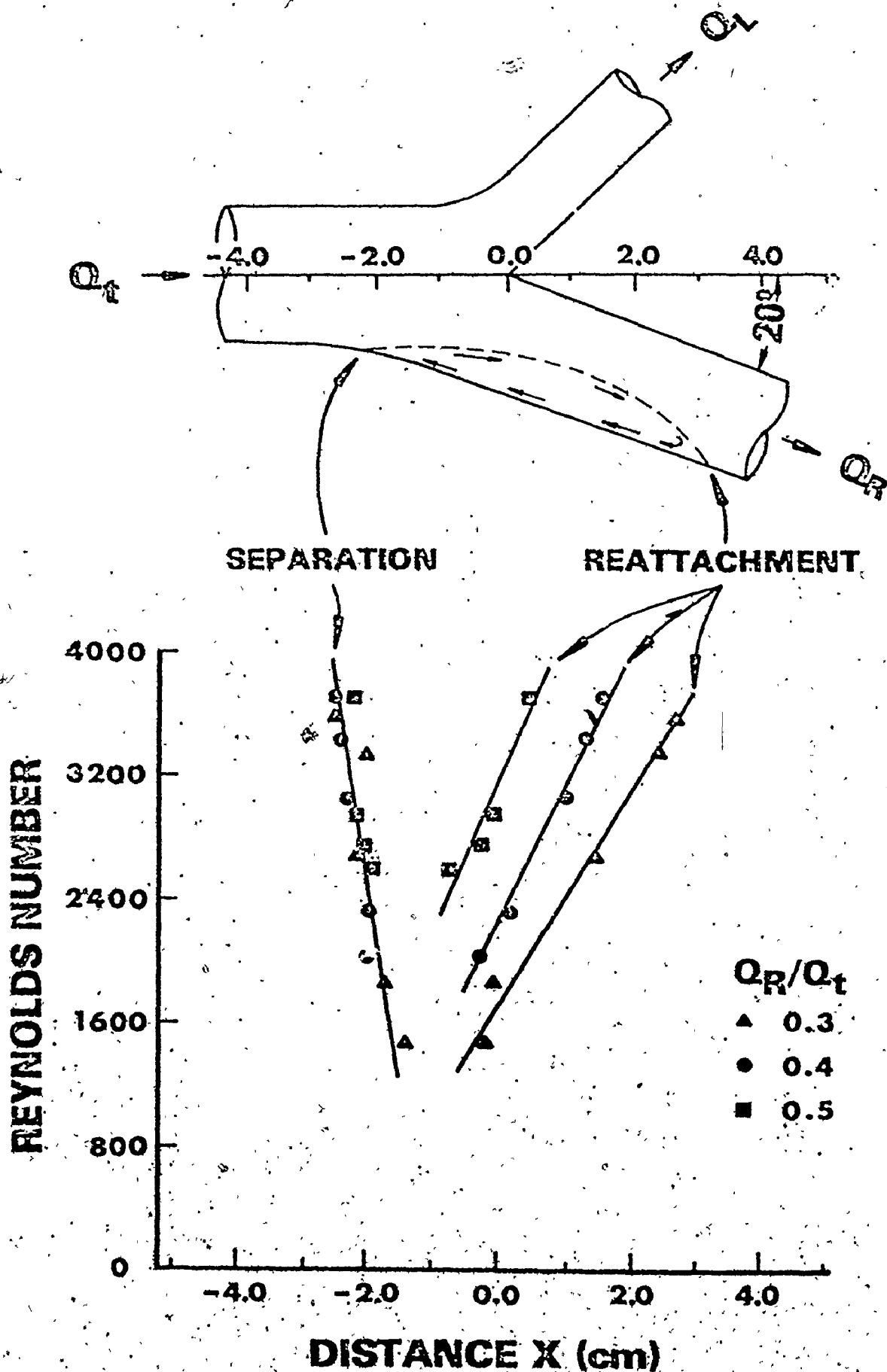
Figure 4.16(b)   Definition of Separation and Reattachment
Positions for the Right Side Branch of Model
2 as a Function of Reynolds Number and Flow

to move slightly upstream. This is best shown with the larger branch of Model 2 (Figure 4.16(a)) and suggests that branch curvature magnifies this effect.

4.3 Pulsatile Flow

A limited investigation aimed at defining the difference between pulsatile and steady flows was undertaken. Physiological pulsation was approximated here by a sine wave flow component added to the steady flow component. Mean flow Reynolds number range was (1200-1900). Frequencies from 0.2 to 0.6 sec^{-1} were chosen corresponding to α values from 10 to 18. In order to create a base condition (in the parent tube) in which no reverse flow was present, an additional constraint upon the flow fluctuation ratio was necessary. This aided the experimental recognition of separated flow and resulted in a flow fluctuation ratio range of 0.8 to 1.2.

The first set of observations were made at flow division ratios which would not have led to flow separation for steady flow within the Reynolds number range chosen for pulsatile investigation (1200-1900). These operating points come from zone B for Models 1, 2, 3 and 4 (Figures 4.11 to 4.19). At frequencies less than $0.3 sec^{-1}$ (α less than 12), the instantaneous flow patterns were similar to those observed in steady flow (see Figures 4.1 to 4.4) and included a shift in pattern from the maximum to minimum of the flow pulse akin to that observed in steady flow between Reynolds numbers of 900 and 3600 (see Figure 4.5). The instantaneous patterns closest

in form to the comparable steady flow patterns at the same
flow conditions occurred at the maximum and minimum points
in the flow pulse where the fluid was neither accelerating
or decelerating. No flow reversal was observed near the wall
at these frequencies, less than $0.3 \sec^{-1}$. For frequencies
above $0.3 \sec^{-1}$ (α greater than 12), there was reverse flow
on one or both of the outside walls of Models 3 and 4. These
reverse flows occurred only over a portion of the decelerating
part of the flow pulse. No back flow was observed on the walls
of the flow divider, the inner wall of the branch.

Since reverse flow may be an integral part of pulsatile
flow, for some fraction of the pulse cycle, depending on the
value of α and the flow fluctuation ratio [47], it is necessary
to distinguish this from separation which also displays reverse
flow. Despard and Miller [52] have, based on experimental
evidence, established a criterion for flow separation during
pulsatile flow which requires reverse flow during the entire
pulse cycle (see section 3.1.3). According to this criterion,
flow separation was not present during the experiments
described above.

A second set of observations were made at flow division
ratios which would have led to flow separation for steady
flow within the Reynolds number range chosen for pulsatile
flow investigation (1200-1900). These experiments dealt only
with Models 1 and 2 with operating points taken from zones A
and C of Figures 4.11 and 4.12. Using the criterion of
Despard and Miller, flow separation was observed at conditions

approximately equal to those for flow separation in steady
flow. The location of the separation points for these
experiments were indistinguishable from the comparable steady
flow separation points (same mean flow Reynolds number and
flow division ratio). Both flow conditions for separation
and location of separation point were found to be independent
of pulse frequency in the range of this study (0.2-0.6 sec^{-1}).

4.4   Discussion

The complex nature of three dimensional flows within
models of arterial branches has been clearly demonstrated
here and in a number of other studies [13-19, 21, 25, 29-34].
In part this arises from the geometrical shapes of the transi-
tion sections at the junctions of branching tubes. This
results in a potential extensive expansion and contraction of
effective tube cross-sectional flow area. As has been demonstrated
here, asymmetry is a second factor leading to complex flows.
Flow patterns, which are characterized by secondary flow
motions, are present in all the four models. Flow parameters
such as Reynolds number and flow division ratios are important
factors in determining the actual flow patterns.

It has been previously shown that vortex motion is
developed downstream of an asymmetrically placed obstruction
in a circular tube and that the recirculating streamline in
such a flow completes a finite number of cycles before leaving
the recirculation region [23]. This is in contrast to flows
downstream of a symmetrical expansion which displays continuously

circulating vortex streamlines [56, 57]. The flow separation observed in the current study are analogous to those of the asymmetrical case. This means that they all have open recirculating vortex regions. Fresh upstream fluid enters and leaves the separation vortex simultaneously.

Although two-dimensional channel flows (in contrast to three-dimensional flows within branching circular tubes) may demonstrate flow separation and disturbed flows [4, 32], the occurrence of these would necessarily be at flow conditions (Reynolds number and flow division ratio) quite different from those for the comparable three-dimensional cases. The lack of any flow separation for Model 1(aortic bifurcation) and Model 2 (iliac bifurcation) for a range of flow division ratio and up to a Reynolds number of approximately 4000 is an example. This has been previously explained in terms of a flow crossover phenomena [16, 50] wherein high velocity fluid from positions close to the central core region of the parent tube crosses over to the outside of the daughter tubes thus helping in the prevention of boundary layer separation - this is consistent with the streamline patterns demonstrated here. The forces necessary to develop such flows are not possible in a two-dimensional channel configuration.

The results of the flow separation study presented here are in good agreement with other studies in similar models [16, 19] and further extend the range of those studies and characterize the separation conditions in a systematic way. The absence of flow separation in symmetric bifurcations with equal flow

division (Q_L/Q_t = 0.5) has been reported by Feuerstein et al.
[50] and Brech and Bellhouse [16] to be true for symmetric
three-dimensional models up to Reynolds numbers of 1200,
in [50] and 1500 in [16]. In a side branch model (similar to
Model 3), Rodkiewicz and Roussel [19] have shown that separated
flows may occur in both branches at the same time under flow
conditions akin to those presented here by zone AC in
Figure 4.17.

In vitro pulsatile flow studies with whole blood
have shown that boundary layer separation occurs at a threshold
flowrate (Reynolds number) and that localized velocity perturba-
tions within the separation region are present [58, 59].
The model used by these workers is similar to Model 3 of this
study. Turbulence and localized velocity fluctuations akin to
those found in vitro [58, 59] occur in vivo at the junction of
the abdominal and iliac artery in dogs [25]. Similar flow
distrubances were found in vivo at the ilioaortic junction in
pigs [60]. Although flow separation is implied in these in vivo
studies as the main cause of flow disturbances, they do not
contradict the findings of this work where no flow separation
was observed for a wide range of flow division ratios in a
model of an abdominal aortic bifurcation. They may be explained
by the fact that the dog and pig have aortic trifurcations in
which the area ratio changes within the junction may be
sufficiently large to induce flow separation not found in
bifurcation.

CHAPTER 5

ELECTROCHEMICAL TECHNIQUE

5.1 Introduction

The diffusion-controlled electrochemical technique is one of the most useful techniques for qualitative measurements of transport phenomena in liquids. However, it should be noted that there are limitations in the use of this method. First, it is limited to liquids; accordingly, the data of mass-transfer are limited for high Schmidt numbers (Sc). Second, only certain kinds of liquids can be used, i.e., those in which a diffusion-controlled electrolytic reaction occurs [61].

In this technique an electrochemical reaction is carried out at the surface of an electrode which is mounted flush with a solid wall. This test electrode works as the cathode of the electrochemical cell. The anode is located downstream of the cathode and has a much larger area than the cathode so that the electric current flowing in the circuit is controlled by mass transfer at the cathode surface.

5.2 Electrochemical Reaction Under the Diffusion-Controlling Condition

The electrochemical technique is analogous to the constant-temperature hot-wire anemometer in that the concentration

of the diffusing species is made constant (and equal to zero)
at the cathode surface and the current is proportional to the
rate of mass-transfer to the electrode. This current is called
the limiting current. From the limiting current density values,
the transfer rate of mass or momentum can be calculated.

The technique is based on a diffusion controlled reaction
of ferricyanide ion to ferrocyanide ion at the cathode. At
the anode, ferrocyanide is reconverted to ferricyanide, thereby
maintaining a constant concentration of both chemical species.
This reaction can be written as:

Cathode $\quad Fe\ (CN)_6^{-3} + e \rightarrow Fe\ (CN)_6^{-4}$

Anode $\quad\quad Fe\ (CN)_6^{-4} \rightarrow Fe\ (CN)_6^{-3} + e$
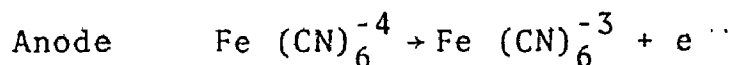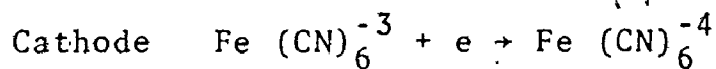
The test solution used in this work consisted of 0.1
M each of potassium ferricyanide ($K_3\ Fe\ (CN)_6$] and potassium
ferrocyanide ($K_4\ Fe(CN)_6$] in a strong (2M) aqueous solution
of sodium hydroxide (NaOH). The NaOH provided for an
excess of electrolyte, which made it possible to neglect ion
migration due to potential gradients near the cathode, and to
prolong the life of the ferricyanide solutions, which are
less stable at low pH.

The rate of transfer of ferricyanide ion is given by:

$$N = -\ (D + \epsilon_D)\ \frac{\partial C}{\partial y} \qquad\qquad (5.1)$$

where y is the direction perpendicular to the surface
of the electrode.

Integration of Equation (5.1) in the general case [61] gives:

$$N = \overline{K} \, (C_b - C_w) \qquad (5.2)$$

where C_b and C_w are the concentration in the bulk and at the wall respectively.

The ion flux (N) can be determined by measuring the current flowing in the circuit and using Faraday's equation:

$$N = \frac{i}{A \, F} \qquad (5.3)$$

where i is the measured current.

A is the cross-section area of the electrode surface,

and   F is the Faraday's constant

Equations (5.2) and (5.3) can be combined to give:

$$\frac{i}{A \, F} = \overline{K} \, (C_b - C_w) \qquad (5.4)$$

The concentration of ferricyandide ion at wall C_w depends on the rate of ionic reaction at the cathode. At a large enough voltage across the two electrodes the reaction rate is fast enough that C_w is essentially zero at the test electrode and the current is controlled by the magnitude of the mass transfer coefficient. The experiments consist of controlling the voltage at a value so that $C_w \cong 0$ and measuring the current

At the limiting current Equation (5.4) becomes

$$\overline{K} = \frac{i}{A \, F \, C_b} \qquad (5.5)$$

The limiting current can be seen easily from the potential
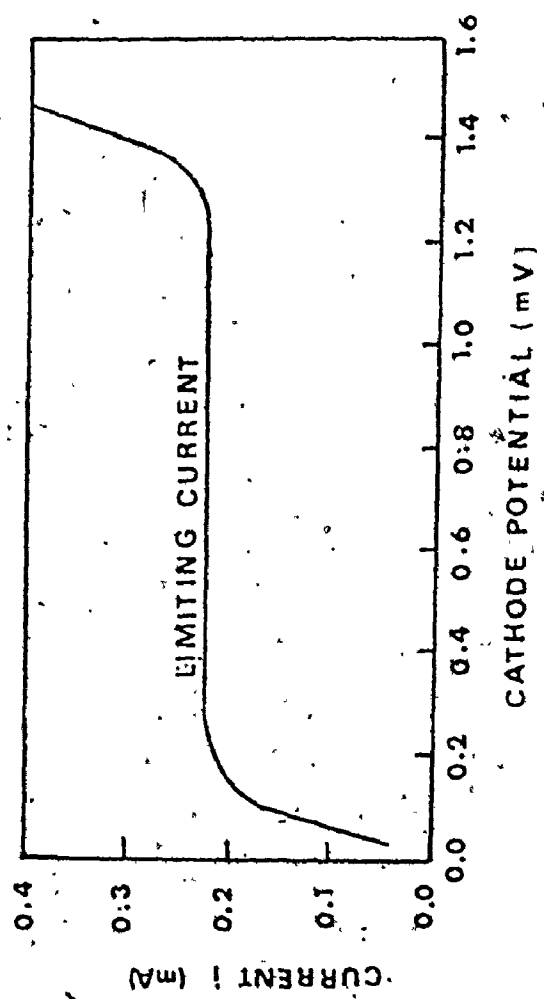
Figure 5.1   Potential-current Relationship.

current curve given in Figure 5.1. As the applied voltage is increased the current increases exponentially due to the accummulation of the ions at the surface of the cathode which is equivalent to the charging current. As the potential is made higher the current increases further and approaches a constant value, i.e., a limiting current, asymptotically. Under the condition of limiting current, the ions transferred to the electrode surface react very soon and the increasing potential does not result in an increase in the rate of the desired reaction [61]. A further increase of the potential over the limiting current region causes a steep increase in the current due to the discharge by a secondary reaction such as hydrogen evolution on the cathode surface.

The electrochemical technique can be used also to measure the velocity gradient at a liquid-solid interface. The theory which relates mass transfer measurements to the velocity gradient at the surface is outlined in the next section (Section 5.3).

5.3 Theory

Diffusion of the ferricyanide ion to the cathode occurs at the surface of the electrode through a shear rate dependent boundary layer (See Figure 5.2). For a rectangular electrode with its short side (L) parallel to the flow and long side perpendicular to the flow direction, the concentration boundary layer is considered two dimensional. Hence, the general boundary layer equation for mass transfer of the ions may be written as:
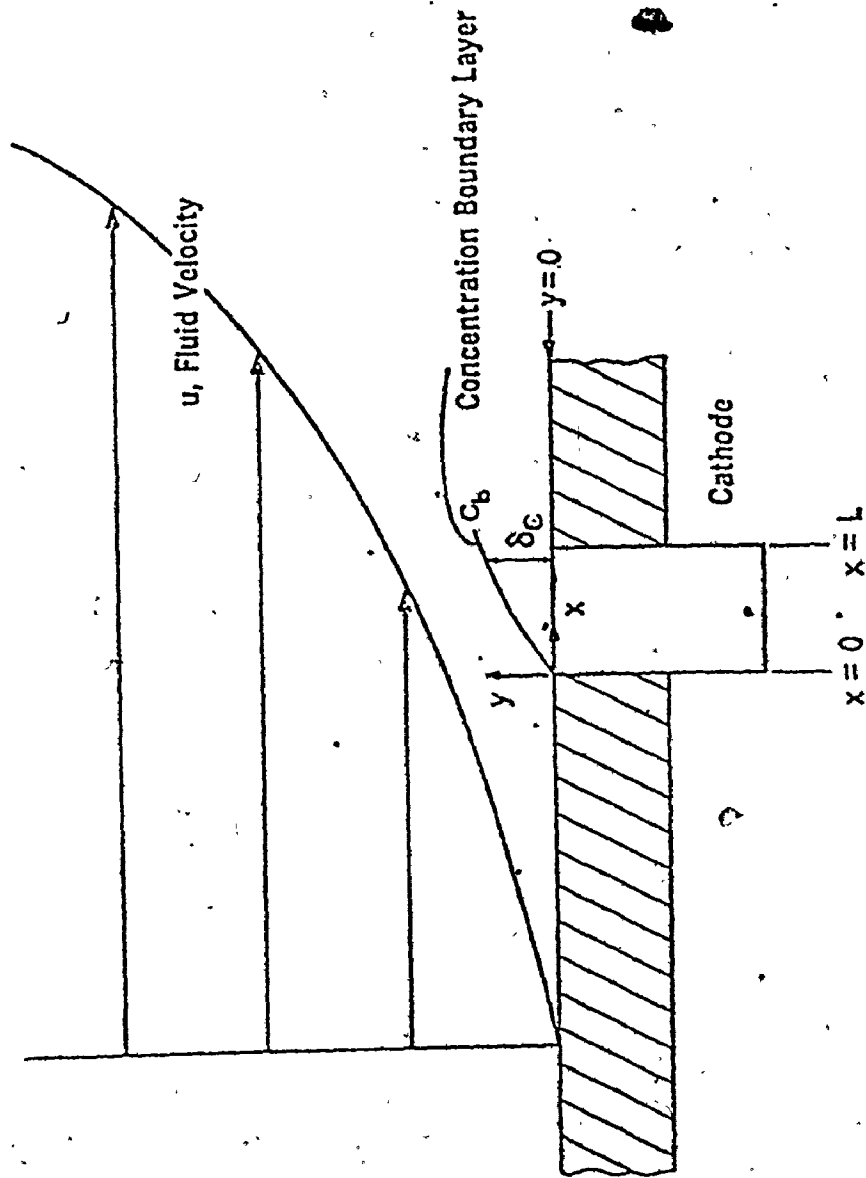
Figure 5.2 Schematic Diagram of a Cathode Imbedded
in the Wall.

$$\frac{\partial C}{\partial t} + u\frac{\partial C}{\partial x} + v\frac{\partial C}{\partial y} = D\left(\frac{\partial^2 C}{\partial x^2} + \frac{\partial^2 C}{\partial y^2}\right) \qquad (5.6)$$

where x and y are the coordinates in the direction of the flow and perpendicular to the surface, respectively.

The term $\frac{\partial^2 C}{\partial x^2}$ representing the diffusion in the flow direction can be neglected for large values of velocity gradient [62]. This assumption is true except in the flow very close to the separation point. Hence Equation (5.6) is reduced to

$$\frac{\partial C}{\partial t} + u\frac{\partial C}{\partial x} + v\frac{\partial C}{\partial y} = D\frac{\partial^2 C}{\partial y^2} \qquad (5.7)$$

The boundary conditions are

$C = 0$ at $y = 0$ for $0 \leq x \leq L$

$C = C_b$ at $y = \infty$ (5.8)

$C = C_b$ at $x = 0$

where C_b is the bulk concentration of ferricyanide ions. The velocity and concentration are expressed as the sum of time smoothed and fluctuating components

$$u = \bar{u} + u', \quad v = \bar{v} + v', \quad C = \bar{c} + c'$$

The ratio of the concentration boundary layer thickness to the momentum boundary layer thickness is proportional to $(Sc)^{-1/3}$ or to $(\frac{v}{D})^{-1/3}$. Since Schmidt number (Sc) for this system is high (>3200), the ratio of the two boundary layer

thicknesses will be small and the velocity gradient $(\bar{s})$ can be assumed to be linear in the very thin concentration boundary layer so that

$$\bar{u} = \bar{s} \, y \qquad\qquad (5.9)$$

From the continuity equation, $\bar{v}$ is calculated

$$\bar{v} = -\frac{1}{2} \left(\frac{\partial \bar{s}}{\partial x}\right) y^2 \qquad\qquad (5.10)$$

where $\bar{s}$ is the time-smoothed velocity gradient at the wall and is a function of x.

The fluctuating velocity near the wall can also be represented by

$$u' = s' \, y \qquad\qquad (5.11)$$

$$v' = -\frac{1}{2} \left(\frac{\partial s'}{\partial x}\right) y^2 \qquad\qquad (5.12)$$

where s' is the fluctuation in the velocity gradient at the wall and is a function of t and x.

For the time-smoothed concentration field, substituting the expressions for $\bar{u}$ and $\bar{v}$ into Equation (5.7) gives

$$\bar{s} \, y \, \frac{\partial \bar{c}}{\partial x} - \frac{1}{2} \left(\frac{\partial \bar{s}}{\partial x}\right) y^2 \frac{\partial \bar{c}}{\partial y} = D \, \frac{\partial^2 \bar{c}}{\partial y^2} \qquad\qquad (5.13)$$

The boundary conditions are:

$$\bar{c} = 0 \quad\;\; \text{at } y = 0 \qquad 0 \le x \le L$$
$$\bar{c} = C_b \quad \text{at } y = \infty \qquad\qquad\qquad\qquad (5.14)$$
$$\bar{c} = C_b \;\;. \quad \text{at } x = 0$$

For a fluctuating concentration, substituting the expressions for u' and v' into Equation (5.7) and neglecting

the second order terms gives:

$$\frac{\partial c'}{\partial t} + \bar{s}\, y\frac{\partial c'}{\partial x} + s'\, y\frac{\partial \bar{c}}{\partial x} - \frac{1}{2}\left(\frac{\partial \bar{s}}{\partial x}\right) y^2\frac{\partial c'}{\partial y} - \frac{1}{2}\left(\frac{\partial s'}{\partial x}\right) y^2\frac{\partial c'}{\partial y} = D\,\frac{\partial^2 c'}{\partial y^2} \qquad (5.15)$$

The boundary conditions are:

$$\begin{aligned}
c' &= 0 \quad &\text{at } y = \infty \\
c' &= 0 \quad &\text{at } y = 0 \\
c' &= 0 \quad &\text{at } x = 0
\end{aligned} \qquad (5.16)$$

These equations can be simplified in each case and solved to relate the mass transfer coefficient to the velocity gradient at the wall.

A) Time-smoothed velocity gradient in a fully developed flow

For a fully developed flow, the velocity gradient s is no longer a function of x and the velocity, $\bar{v} = 0$. Hence Equation (5.13) is reduced to

$$\bar{s}\, y\, \frac{\partial \bar{c}}{\partial x} = D\,\frac{\partial^2 \bar{c}}{\partial y^2} \qquad (5.17)$$

The solution of Equation (5.17) together with the boundary condition given by Equation (5.14) gives the concentration profile, Mizushina [61], as:

$$\frac{\bar{c}}{C_b} = \frac{1}{\Gamma\left(\frac{4}{3}\right)} \int_0^n \exp(-n^3)\, dn \qquad (5.18)$$

where
$$n = y \left(\frac{\bar{s}}{9\,D\,x}\right)^{1/3} \qquad (5.19)$$

The length average mass transfer coefficient over the electrode surface is

$$\bar{k} = \frac{1.5}{9^{1/3} \Gamma(\frac{4}{3})} \left(\frac{D^2 \bar{s}}{L}\right)^{1/3} \tag{5.20}$$

Therefore

$$\bar{s} = 1.9 \frac{\bar{k}^3 L}{D^2} \tag{5.21}$$

B) Time-smoothed velocity gradient
   in the boundary layer

Using a similarity transformation, Mizushina [61], Equation (5.13) together with the boundary conditions (5.14) can be solved to give the concentration gradient at a position at the electrode surface as

$$\left.\frac{\partial \bar{c}}{\partial y}\right|_{wall} = \left(\frac{1}{9D}\right)^{1/3} \frac{C_b}{0.893} \frac{\bar{s}^{1/2}}{\left[\int_0^x \bar{s}^{1/2} \, dx\right]^{1/3}} \tag{5.22}$$

In the boundary layer, the variation of $\bar{s}$ over the small length of the electrode is negligible except in the region close to the front stagnation point in the case of cross flow. Assuming the velocity gradient $\bar{s}$ is constant over the electrode length, one can obtain a solution similar to the solution given by equation (5.21), Dimopoulos and Hanratty [63].

$$\frac{\bar{k}L}{D} = 0.807 \left(\frac{\bar{s}L^2}{D}\right)^{1/3} \tag{5.23}$$

Two simplifying assumptions were made in the derivation
of the mass balance equation (Equation (5.13); neglect of
diffusion in the x-direction, and neglect of natural
convection by density difference in the concentration boundary
layer. Dimopoulos and Hanratty [63] have studied flow
crossing a cylinder and obtained correction terms for these
assumptions. These are added to Equation (5.23) as follows.

$$\frac{kL}{D} = 0.807 \ (\frac{\bar{s}L^2}{D})^{1/3} + 0.19 \ (\frac{\bar{s}L^2}{D})^{-1/6} \pm 0.253 \ \frac{Gr_L}{Re_L} \ (\frac{Sc \ D}{\bar{s}L^2})^{1/3} \ \sin \theta$$

(5.24)

where (+) applies to aiding flows and (-) applies to
opposing flows. These two correction terms, however, were
found to be important only at very low Reynolds numbers and
near the separation point. For example, the correction was
not greater than 2.7% only where on the surface of a cylinder
[63] at Re = 339.

C) Fluctuating velocity gradient
    Pseudo-steady state solution

Assuming the boundary layer to be thin enough that
velocities normal to the surface can be neglected Equation
(5.7) can be reduced to

$$\frac{\partial C}{\partial t} + s \ y \ \frac{\partial C}{\partial x} = D \ \frac{\partial^2 C}{\partial y^2}$$

(5.25)

If a pseudo-steady state approximation is made whereby
the term $\frac{\partial C}{\partial t}$ is neglected, the relation between the instantaneous
mass transfer coefficient and the instantaneous velocity

is given by

$$\left(\frac{\bar{k}+k'}{D}\right) = 0.807 \left[\frac{(\bar{s}+s')L^2}{D}\right]^{1/3} \tag{5.26}$$

If $\frac{s'}{\bar{s}} \ll 1$ the above expression can be simplified to yield the relation

$$\frac{k'}{\bar{k}} = \frac{1}{3}\frac{s'}{\bar{s}} \tag{5.27}$$

and the mean-squared value of k' is given as

$$\frac{\overline{k'^2}}{\bar{k}^2} = \frac{1}{9}\frac{\overline{s'^2}}{\bar{s}^2} \tag{5.28}$$

The validity of the linearization assumption can be checked by a method similar to that outlined by Hinz [69] for the hot-wire anemometer. It was found [62] that for

$$\frac{(\overline{s'^2})^{1/2}}{\bar{s}}$$

less than 0.5 the error in using the linear model is less than 3%.

The pseudo-steady state approximation is valid for small frequencies. Fluctuations of small frequencies (less than 2c/sec) were observed in the mass transfer coefficient measurements of this study. Therefore, the use of the pseudo-steady state approximation was appropriate.

For high frequency fluctuations, the mass transfer fluctuations are smaller than predicted by Equation (5.28). A solution of Equation (5.25) for the general time dependent case can be obtained by treating the concentration boundary layer

like a linear element which responds to fluctuations introduced by the shear stress. Details of such a solution can be found in [65].

5.4 Description of the Experiments

The electrochemical technique as described above was used in this study to obtain the wall shear rate (velocity gradient) distribution along the walls of the arterial models under both steady and unsteady flow conditions. Time-averaged wall shear rates were calculated by means of Equations (5.5) and (5.21) from the experimentally measured current (i). Combining Equations (5.5) and (5.21) yields the working equation

$$\bar{s} = \frac{1.9}{(A F C_b)^3} \frac{L}{D^2} \, i^3 \qquad (5.29)$$

When circular electrodes are used instead of rectangular ones, the effective length in the direction of the flow is calculated by [68]:

$$L_e = 0.8136 \, d_{elec.} \qquad (5.30)$$

Fluctuation in the shear rate field was calculated from the corresponding mass-transfer coefficient fluctuation, Equation (5.28).

5.5 Experimental Apparatus and Equipment

5.5.1 Flow System

The same flow system used in the visualization study (described in detail in Section 2.4) was subsequently used

for the electrochemical measurements. Materials used in
the construction of this system were inert in the presence of
the electrolyte. Tank D (Figure 2.6) was used in this applica-
tion to maintain a positive nitrogen pressure on the surface
of the electrolyte solution so that the effect of the presence
of oxygen on the measurements was minimized.

5.5.2 Electrodes

The electrochemical reaction was carried out on
small circular nickel electrodes made from wire of diameter
1 mm. These wires were inserted through the walls of the models.
Undersize holes were drilled in the plastic walls and the
wires were pushed through from the outside until they were
solidly lodged in the holes then they were glued in place with
epoxy cement. The wires were then made flush with the wall by
hand sanding using progressively finer grades of emery paper
and finally buffing with a powered spindle covered with soft
cloth.

In order to attain good reproducibility of the measure-
ments, the electrodes were cleaned before each run with carbon
tetrachloride and buffed with rouge paper. They were also
cathodically cleaned in 5% sodium hydroxide solution at a
current density of 20 ma for approximately 15 minutes to
ensure elimination of chemical polarization for this redox
system. After the model was rinsed with distilled water it was
installed in the flow system. Following each run the model
was immediately disconnected from the flow system, rinsed with

distilled water and wiped dry with a clean rouge paper.
When the above procedure was followed the reproducibility of
the measurements ranged from 2 to 6%.

The anode was made of a large stainless steel ring
whose inner diameter was equal to the daughter tube inner
diameter. Placed downstream of the wire electrodes, the anode
ring was made flush with the wall of the daughter tube. The
5 cm long anode was large enough, compared to the size of the
wire electrode, so that the current is controlled by the
mass transfer at the cathode surface.

5.5.3 Electrolyte Solution

In all the experiments, the redox system used was
approximately 0.1 equimolar solution of potassium ferricyanide
$(K_3[Fe(CN)_6])$ and potassium ferrocyanide $(K_4[Fe(CN)_6])$ in
aqueous solution (2 molar) of sodium hydroxide (Na OH). The
sodium hydroxide acted as an indifferent electrolyte to eliminate
any migration due to ionic transference effects. The solutions
were prepared immediately prior to the runs using distilled
water. Nitrogen was previously bubbled through the distilled
water and the prepared solution to eliminate any dissolved
oxygen. The adverse effect of air-saturated solutions on the
electrochemical data is reflected by a change in the slope and
actual value of the limiting current curve. However, the
technique can be applied at up to 70% O_2 saturation with an
operating time of 275 minutes and still obtain results within
5% of the correct values [66]. Furthermore, precautions were

taken to keep the system away from exposure to light for a
long period. Potassium ferrocyanide is photosensitive and
slowly decomposes to form hydrogen cyanide which would poison
the electrodes [66]. However, decomposition of the ferro-
cyanide complex can be practically eliminated in alkaline
solutions in the absence of light.

The electrolytic reaction at the cathode electrode
was the reduction of ferricyanide ion to ferrocyanide ion. At
the anode ferrocyanide was reconverted to ferricyanide. This
redox couple was suitable in the present study, since in
alkaline solutions it was relatively stable, its reaction was
rapid, and the critical flow rate (where no diffusion controlled
region is present) [61] was not reached in these experiments.
The system has been extensively studied by other investigators
[67, 68 and 69] and as a result methods to determine its
physical properties are available in the literature.

The density of the solution was measured by means of
a 50 cc pycnometer equipped with a capillary and calibrated
with distilled water. Viscosity was measured by a Ubbelohde
type viscometer with an estimated error of less than $\pm$ 0.5%.
The diffusion coefficient of ferricyanide ion was calculated
by means of the following equation, Eisenberg et al. [67]:

$$\frac{D\mu}{T} = 2.50 \times 10^{-10} \frac{cm^2}{sec} \cdot \frac{Poise}{^{o}K} \qquad (5.31)$$

The electrolyte composition was maintained nearly
constant for all the experimental runs. Slight variations in

TABLE 5.1 Variation in Electrolyte Properties (18°C)

Ferricyanide concentration	0.087	–	0.106	molar
Ferrocyanide concentration	0.092	–	0.098	molar
Sodium hydroxide concentration	2.38	–	2.40	molar
Density	1.1441	–	1.0923	g./cm^3
Viscosity	1.7432	–	1.5991	centipoise
Diffusion coefficient	4.13×10^{-6}	–	4.55×10^{-6}	sq. cm/sec.
Schmidt number	3690	–	3300	

the properties were due to the amount of water used to make
up different electrolytes and the difference in temperature from
run to run. The electrolyte properties varied within the
limits shown in Table (5.1)..

5.5.4 Electrical Circuit

The electrical circuit used in this work is similar
to that used by Mitchell and Hanratty [63] and is shown in
Figure 5.3.

A 6-V battery supplied a constant D.C. voltage which
was attenuated across a 200 Ω potentiometer. The potentiometer
slide-wire was connected to the positive input and to the
chasis ground of a wide band D.C. amplifier (Hewlett Packard
467A Amplifier) which was operated in the open loop mode. The
cathode (test electrode) was connected to the negative input
and a feedback resistor (10K Ω) was connected between the
negative input and the output of the amplifier. This arrange-
ment was used in order to keep the cathode voltage constant
and equal to that at the positive input of the amplifier, even
though the current flowing through the electrochemical cell
might fluctuate. The current in the electrochemical cell was
measured as an iR drop across the feedback resistor at the output
terminal. Average iR drops between .5 to 4V (corresponding
to average cell current between 50 to 400 μA) were obtained
from this system without additional amplification.

The iR voltage measurements were obtained by using a
(Fluke 8300A) digital voltmeter and the fluctuations in the

92
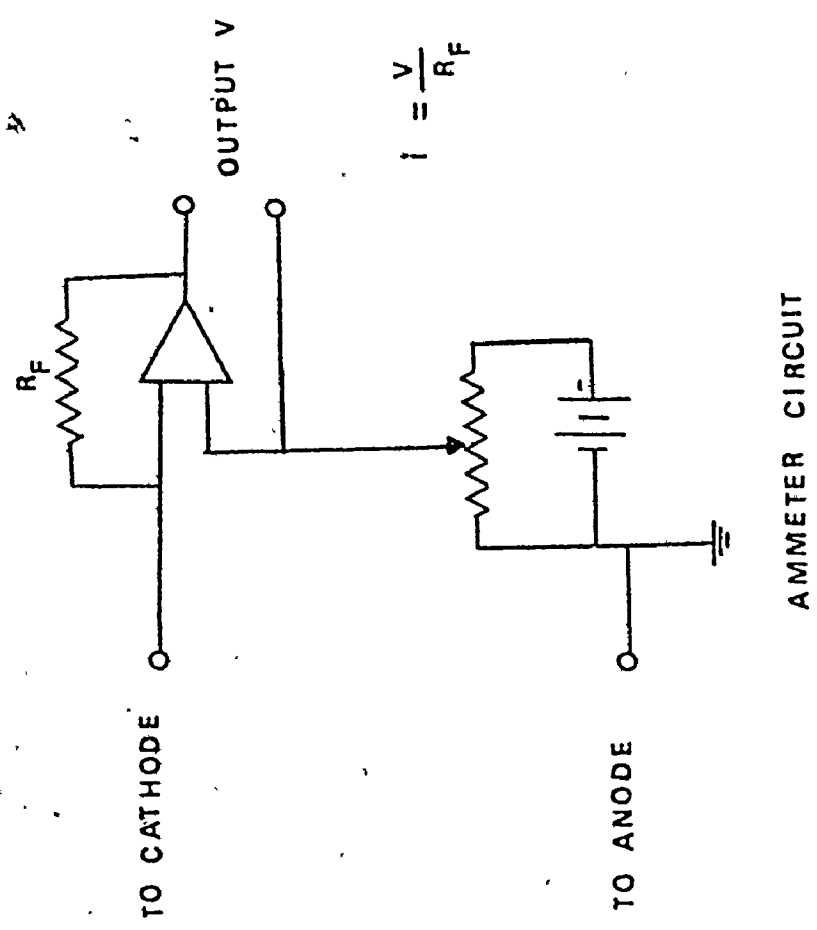
Figure 5.3 Electrical Circuit for Electrochemical
Current Measurements.

voltage were seen and recorded using an oscilloscope
(Tektronix Type 564B) and a recorder (Hewlett Packard Type
7702A).

5.6 Accuracy of the Electrochemical Technique

The use of average mass-transfer measurements to obtain
wall shear rate can be checked by comparing the measured
values of $\bar{K}$ with those calculated from Equation (5.21). This
has been done previously by others [62, 63, 68-7]. Tests in
a 2.54 cm (1 in) pipe [62, 69, 70] have shown that the electro-
chemical technique gives accurate values of the wall velocity
gradient over a Reynolds number range of 300-70,000. Also
measurements on the flow around a 2.54 cm (1 in.) cylinder
for Reynolds number ranges of 60-360 [63], and $5 \times 10^3 - 10^4$
[71] have shown good agreement with the boundary-layer solution
given by Schlichting [51]. Results of these studies are given
in Appendix D.

In this study, fully developed laminar flow in a
circular tube was used to check the accuracy of the technique
by comparing the measured mass-transfer coefficients with those
calculated by Equation (5.21).

Equation (5.21) can be written in the form

$$\bar{K} = 0.807 \ (\frac{D^2 \bar{s}}{L_e})^{1/3} \tag{5.32}$$

For fully developed laminar flow the velocity gradient
at the wall can be calculated from the measured volumetric flow
rate (Q) and the tube diameter (D) using the Hagen-Poiseuille

FLOW

ENTRY
SECTION

NICKEL
ELECTRODES

STAINLESS
STEEL ANODE

D

A   A

SECTION A-A
ELECTRODE CONFIGURATION
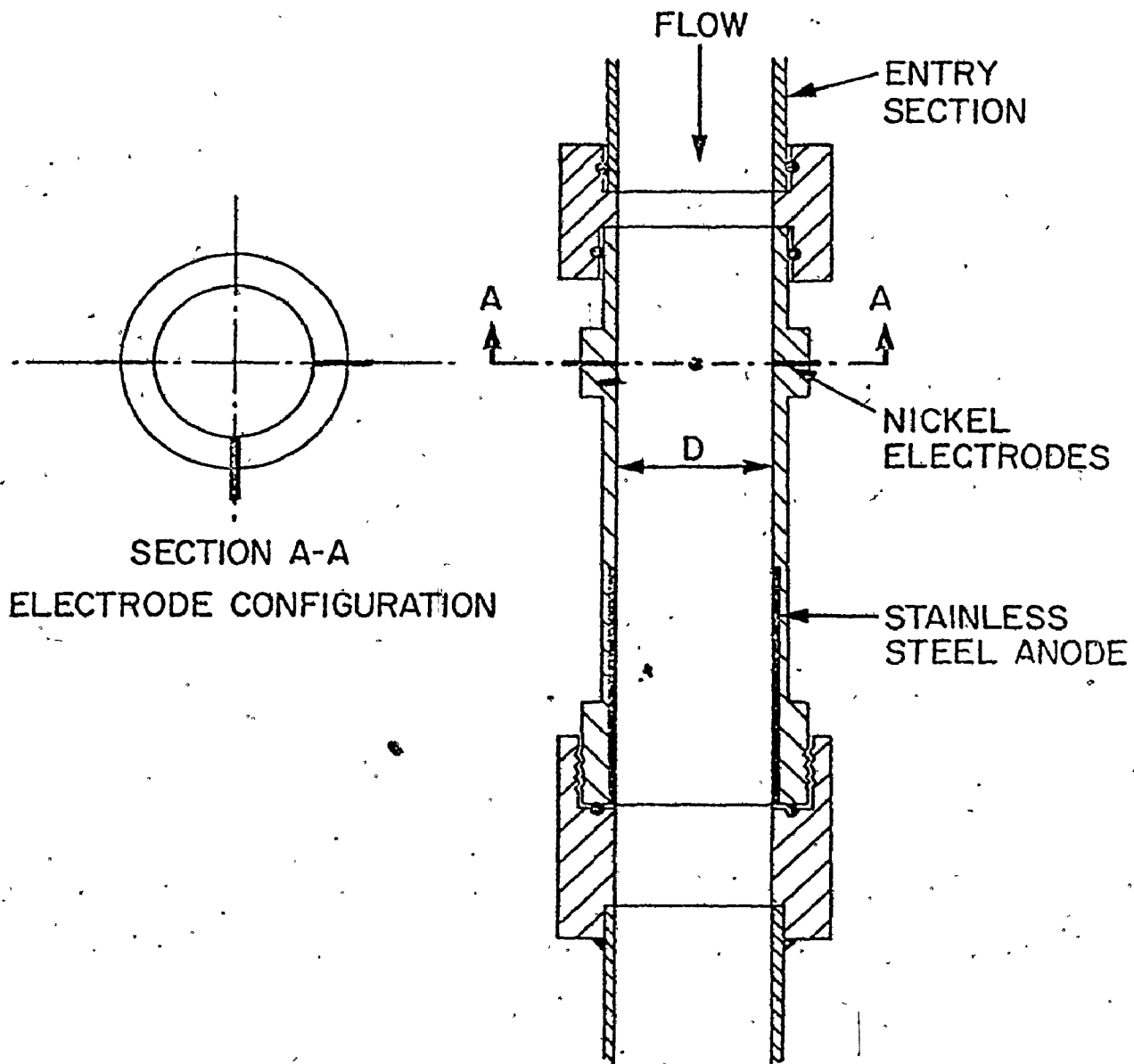
Figure 5.4   Test Section for Straight
Tube Experiment.

equation

$$\bar{s} = \frac{32}{\pi D^3} Q \qquad (5.33)$$

Measurements of mass transfer coefficients were carried out in two test sections made of round tubes of plastic. (See Figure 5.4). Two sizes of entry section and test section were used (D = 1.07 and 2.2 cm) to provide for a wide range of shear rate (20-250 sec^{-1}) under laminar flow conditions. Test electrodes were made of 3 sizes of nickel wires (d_e = .5, 1 and 1.6 mm). The electrolyte properties are given in Table (5.2).

Sodium hydroxide concentration	2.4	molar
Ferricyanide concentration	.106	molar
Ferrocyanide concentration	.098	molar
Density	1.0923	g./cc.
Viscosity	1.5991	Centipoise
Diffusion coefficient	4.55×10^{-6}	sq. cm./sec.

Table 5.2 Electrolyte Properties ($18^\circ C$)

An electrical potential was applied between the test electrode and the downstream anode, and the current in the circuit was measured. Plots of the cell current vs. the applied voltage (Figure 5.5) showed that after a certain voltage a limiting current was obtained. The limiting current value was dependent on Reynolds number. Mass transfer coefficient values
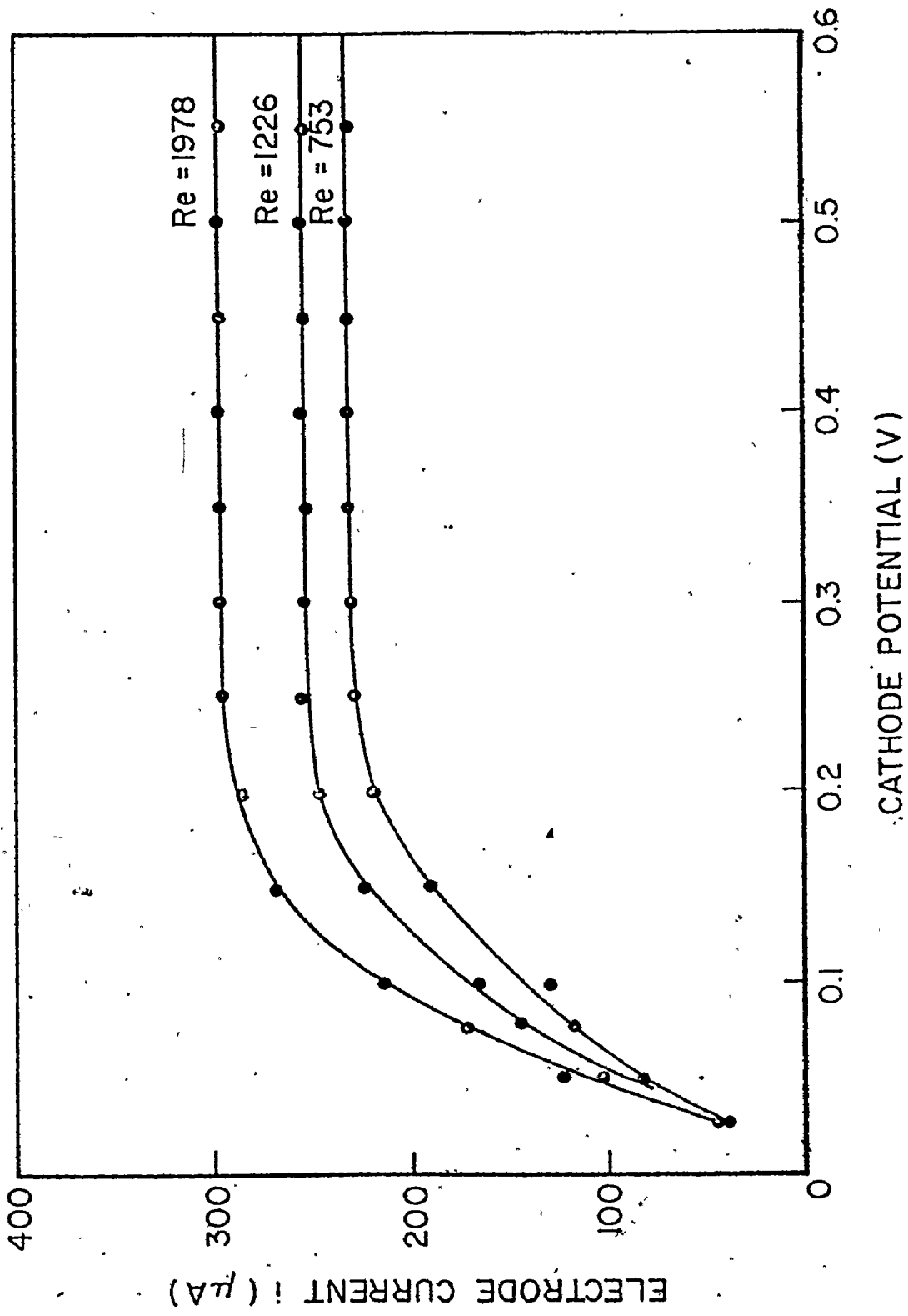
Figure 5.5   Polarization Curves for Straight Tube Experiments.

The figure is a polarization plot of ELECTRODE CURRENT i (μA) on the vertical axis (ranging 0 to 400) versus CATHODE POTENTIAL (V) on the horizontal axis (ranging 0 to 0.6). Three curves are shown, labelled Re = 1978, Re = 1226, and Re = 753.

were calculated from their respective limiting current values
by means of Equation (5.5) and plotted as a function of the
wall shear rate (Figure 5.6). Experimental values were within
$\pm$ 2% of the mass transfer coefficient values predicted by
Equation (5.32).

98
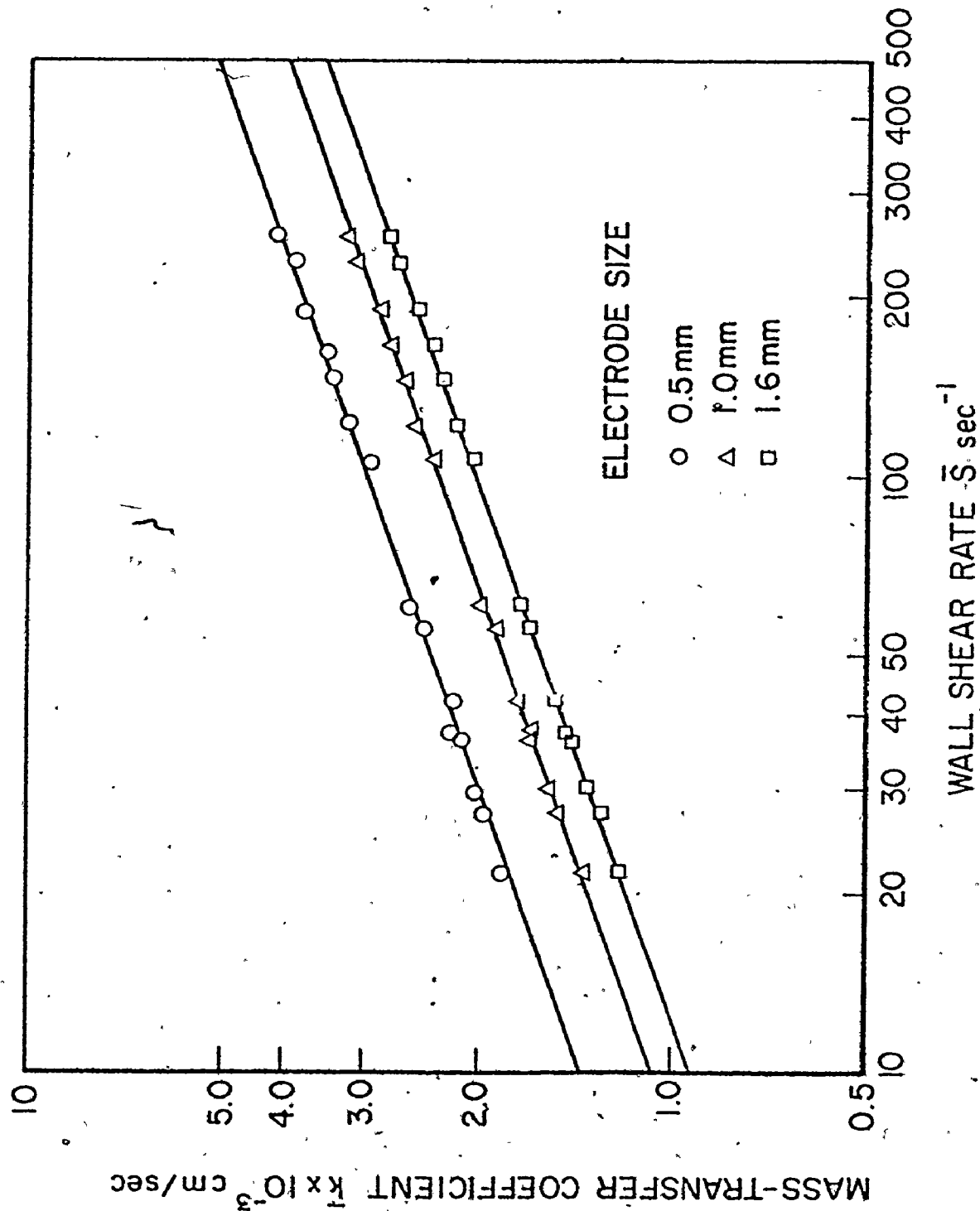
Figure 5.6   Comparison Between Electrochemical Mass-Transfer Coefficient Measurement
and Values Predicted by Equation (5.21). Wall Shear Rate is Calculated
from Flow Rates. (Equation (5.21) is Represented by Solid Lines.

CHAPTER 6

WALL SHEAR RATE STUDY

6.1   Wall Shear Rate Distribution

Since several theories on the formation of early
atherosclerotic lesions [2, 5-11] are dependent on the magni-
tude and direction of wall shear stress, it was important to
obtain accurate values of shear rate along the walls of the
arterial models used in this tudy. The use of the electro-
chemical technique described in the previous chapter provided
for precise measurements of this quantity at the fluid wall
interface over an extremely small surface area (the area of
the electrode surface). These measurements were used and
are applicable only for the magnitude of the velocity gradient
(shear rate) and not for its direction. Wall shear rate
patterns studied here were expected to go through a change in
direction as the flow near the wall separated. Since the flow
visualization study provided complete identification of reversal
flow sites, therefore the assignment of either positive or
negative sign to the local shear rate values was possible.

The steady-flow shear-rate patterns presented in this
section were obtained by measuring and recording the electro-
chemical-reaction limiting current from a number of test
electrodes (size 1 mm wires) implanted into the walls of the

arterial models. In all the runs reported here, the current signals were reasonably steady for locations on the flow divider and prior to the separation sites on the outside walls. However, within the separation site, the signals showed irregular fluctuations of low frequency. These fluctuating signals were time-averaged by integration from recorder samples over a period of up to 1 minute.

6.1.1 Wall Shear Rate Distribution in Model 1

A schematic presentation of Model 1 is given in Figure 6.1 in which the positions of various test electrodes are shown. Only the right side branch was studied in detail since the model was considered to be symmetrical about the parent tube axis. Measurements from three electrodes inserted in the wall of the other branch yielded the same results as their counterparts from the right side branch.

Figures 6.2 to 6.4 show the shear rate patterns at three different values of Q_i/Q_t (0.33, 0.5 and 0.84). Reynolds number (based on parent tube larger diameter D) was approximately the same in the three diagrams (Re = 1885 $\pm$ 59). Shear rate distributions along the inside wall of the daughter tube (Wall D) showed similar patterns for the three different flow division ratios. Shear rate was relatively high at the leading edge of the flow divider, electrode D1, and dropped to a relatively low value in a short distance. It reached its minimum value near electrode D2 before it increased again. The magnitude of the shear rate at D4 (4.5 daughter tube diameters
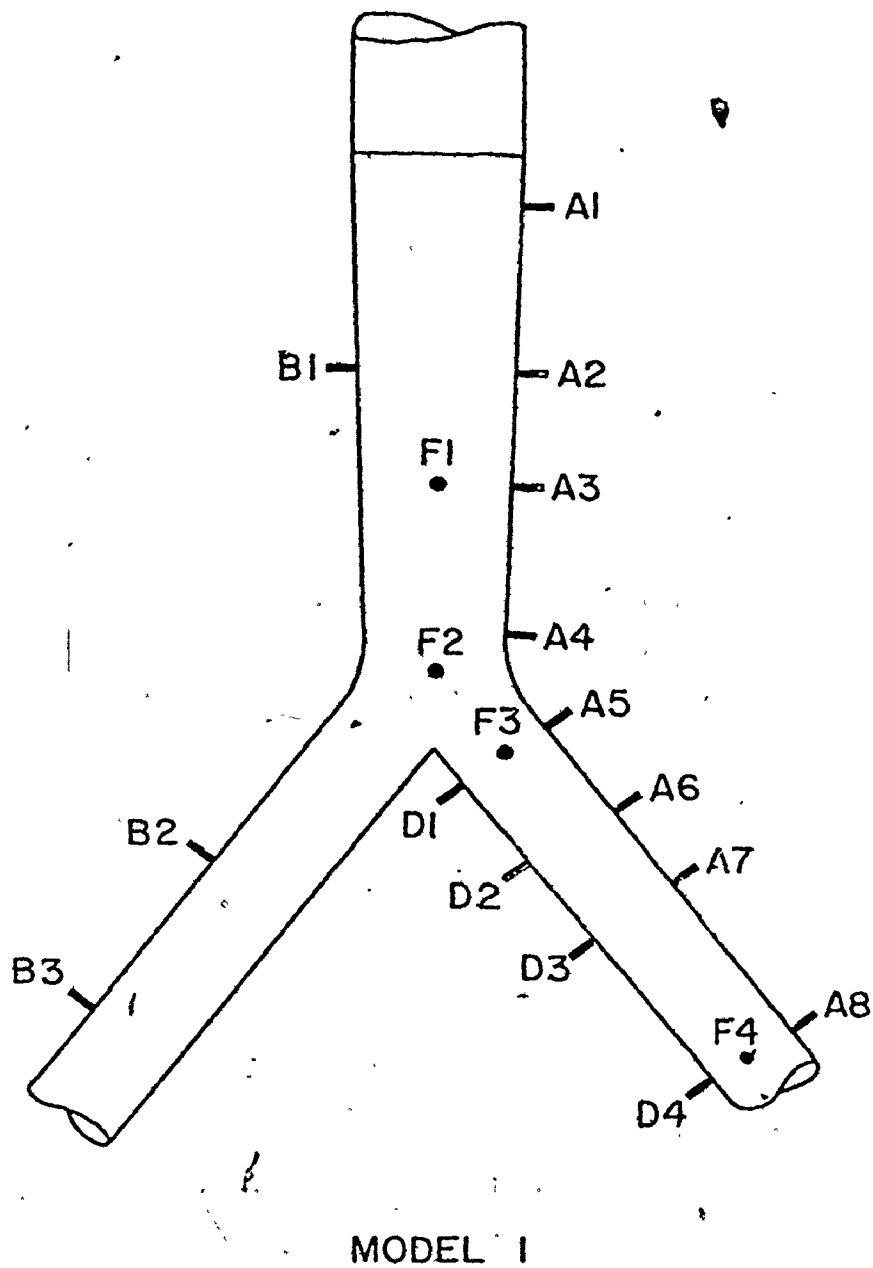
MODEL I

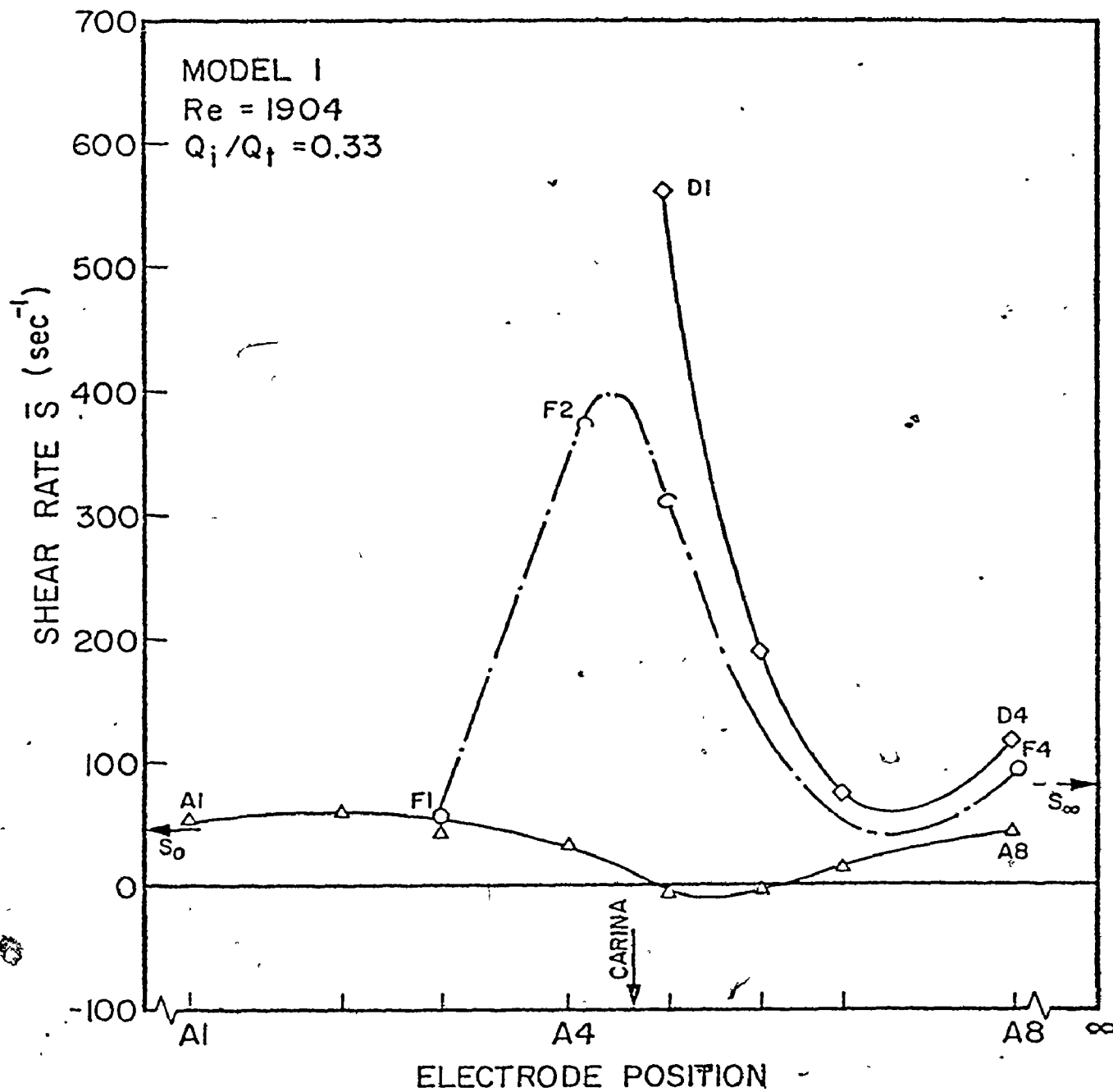Figure 6.1 Positions of Test Electrodes Imbedded
in the Walls of Model 1.

Figure 6.2 Shear Rate Distribution in Model 1.
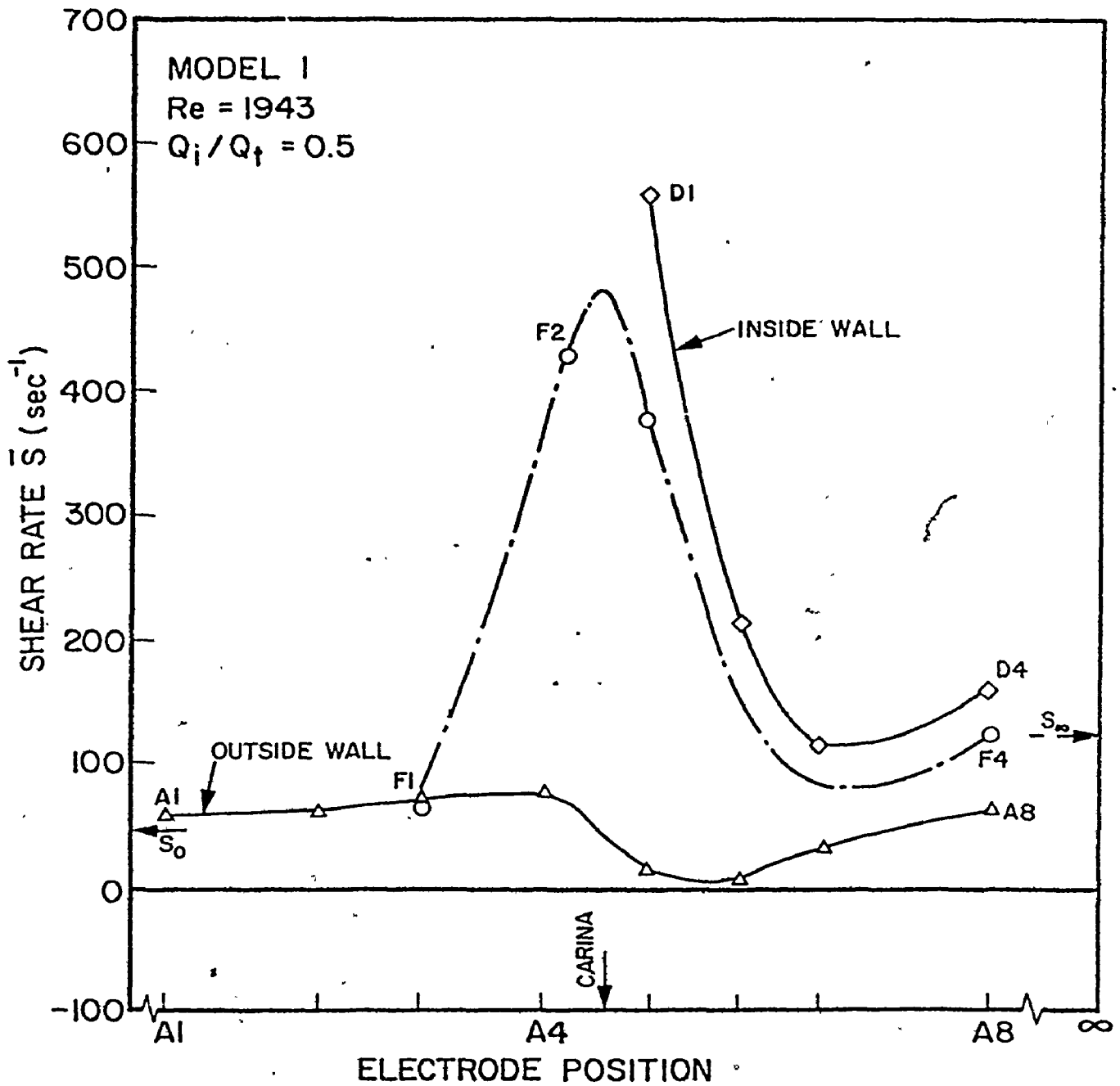Electrode Positions from Figure 6.1.

Figure 6.3 Shear Rate Distribution in Model 1.
Electrode Positions from Figure 6.1.

Figure.6.4   Shear Rate Distribution in Model 1.
Electrode Positions from Figure 6.1.

downstream from the carina) was slightly higher than that of the developed flow value expected downstream of the daughter tube (marked by S_∞ in the figures). This indicated that the flow near electrode D4 was developing. with distance downstream, the shear rate was expected to decrease once again and approached the developed flow value (S_∞) asymptotically. Although the shear rate distribution over the leading edge of the flow divider (2-3 diameters from the carina) was independent of the flow division ratio, it was influenced by the value of the branch flow rate further downstream.

On the other hand, shear rate distribution along the outside wall of the model (wall A) was influenced primarily by the flow division ratio (Q_i/Q_t). While a similar increase. in the shear rate due to the taper of the parent tube was observed over electrodes A1 and A2, for different Q_i/Q_t values, variations in the flow division ratio resulted in distinct changes in the pattern over electrodes A3 to A8. The initial gradual increase in the shear rate values over their upstream developed-flow value (S_0) can be related to the taper of the parent tube in this section which was responsible for a reduction in the flow area and hence, local increase in shear rate. Further downstream, the influence of the branch flow rate was significant. At low branch flow rate (Figure 6.2, $Q_i/Q_t = 0.33$), flow separation associated with flow reversal was predicted (from the flow visualization results, see Figures 4.11 and 4.15), to occur on the outside wall of the branch. The shear rate pattern showed a gradual decrease till

it reached the point of vanishing shear (separation point, see Figure 4.15), then the shear rate changed its direction over electrodes A5 ·and A6. Downstream of the reattachment point the shear rate increased once again and approached its developed value in the daughter tube. At high branch flow rate (Figure 6.4, $Q_i/Q_t = 0.84$), the pattern showed a considerable deviation from that of low Q_i/Q_t. ·Downstream from electrode A2, shear rate continued to increase till it reached its peak value near electrode A4 then dropped to a minimum value near electrode A6. The appearance of a peak in the shear rate distribution was probably due to the strong secondary flow resulting from switching more than 80 percent of the total flow rate into the branch. The intermediate flow division ratio ($Q_i/Q_t = 0.5$) shown in Figure 6.3, showed a gradual transition between the two patterns described above with a moderate level of shear rate and a minimum value near electrode A6.

Distribution of shear rate on the front wall (Electrodes F1-F4) showed a peak value at the intersection between the two daughter tubes and the parent tube followed by a decrease in the shear rate as the flow entered the daughter tube. Within the daughter tube, shear rate values on the front wall were less than those on the inside wall and expected to follow a similar downstream development as reported in references [16] and [17].

There was an increase in the wall shear rate values upon increasing the total flow rate (Reynolds number). This is shown in Figures 6.5 and 6.6. Wall shear rate distributions

Figure 6.5   Shear Rate Distribution in Model 1.
Electrode Positions from Figure 6.1.
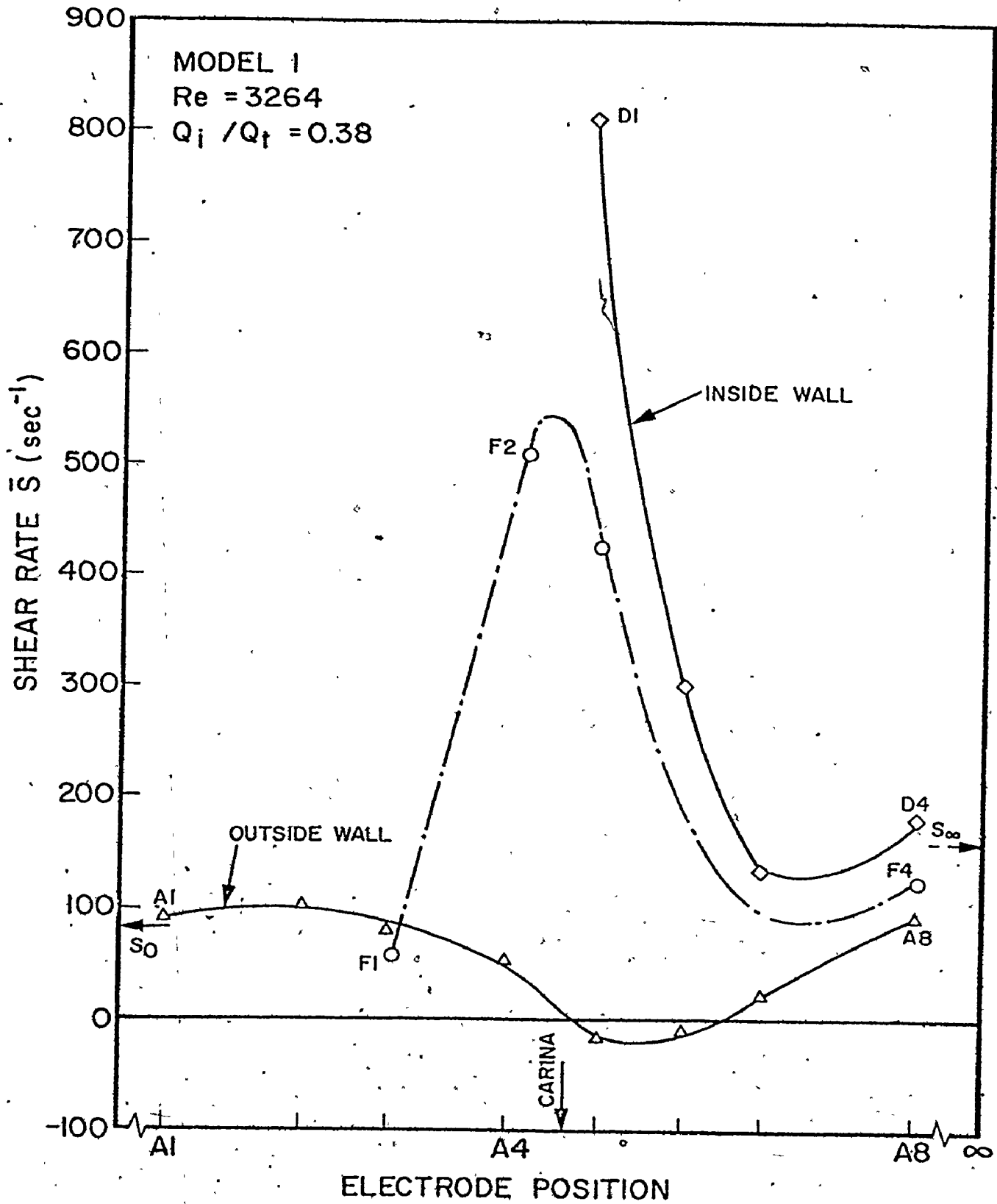
Figure 6.6   Shear Rate Distribution in Model 1.
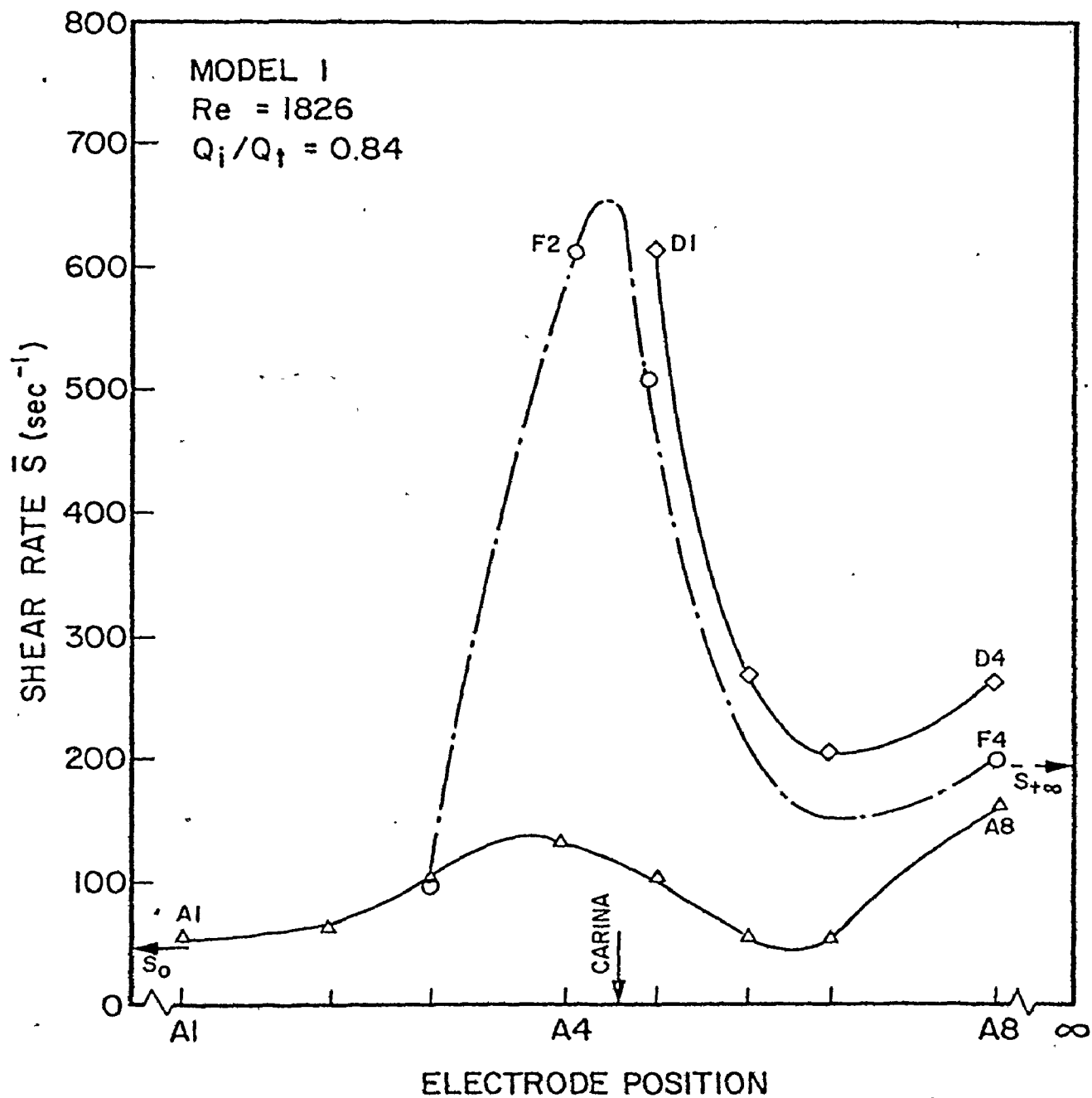Electrode Positions from Figure 6.1.

on both the inside and outside walls of the model were found
to be functions of the total flow rate (Reynolds number)
and proportional directly to its value except near the branch
carina and the separation region. Near the carina (electrodes
D1 and D2) wall shear rate distribution was approximately
proportional to the square root of the Reynolds number.

6.1.2 Wall Shear Rate Distribution in Model 2

Figure 6.7 shows the position of various electrodes
along the walls of Model 2. Since the model geometry is
asymmetric, measurements of shear rate were made along the
walls of both the right and left branches under the same flow
conditions. In Figures 6.8 to 6.11 the shear distribution
for the right branch is given by solid-line curves and is given
by dotted-line curves for the left branch. The shear rate
values S_o, S_R, and S_L represent those of the fully-developed
flow shear values corresponding to the parent tube, the right
branch and the left branch respectively.

Figures 6.8 to 6.10 show the shear rate distribution
along the walls of the model at approximately the same Reynolds
number (Re = 1779 $\pm$ 40). Shear rate patterns corresponding
to three different flow division ratios are presented in these
figures. These flow division ratios were expressed as functions
of the flow rate in the left branch (Q_L/Q_t = 0.156, 0.39 and
0.67). They represent different flow conditions for flow
separation which were shown in Figure 4.12 and given by zones
A, B and C in the figure.

MODEL 2

Figure 6.7   Positions of Test Electrodes Imbedded
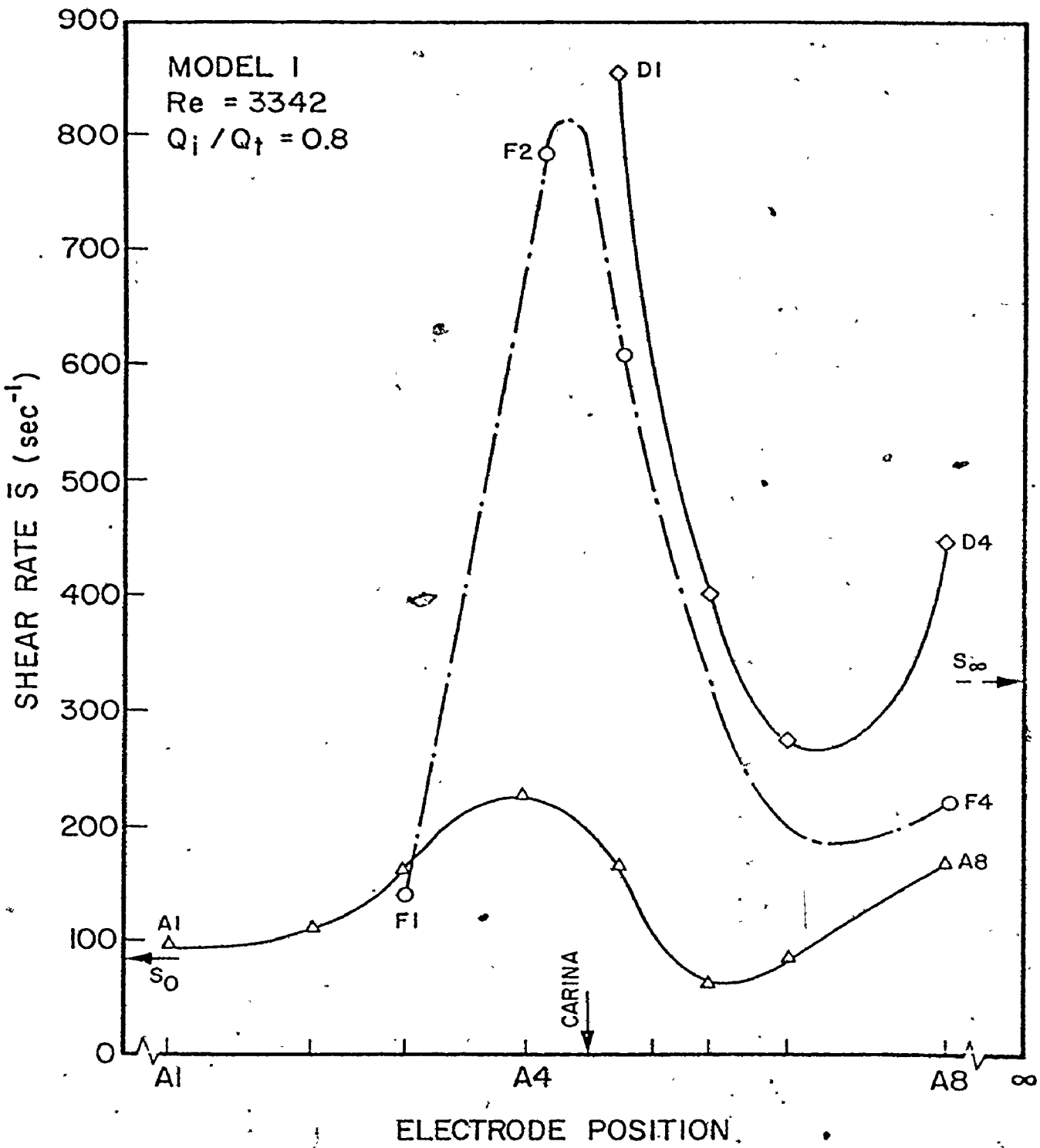in the Walls of Model 2.
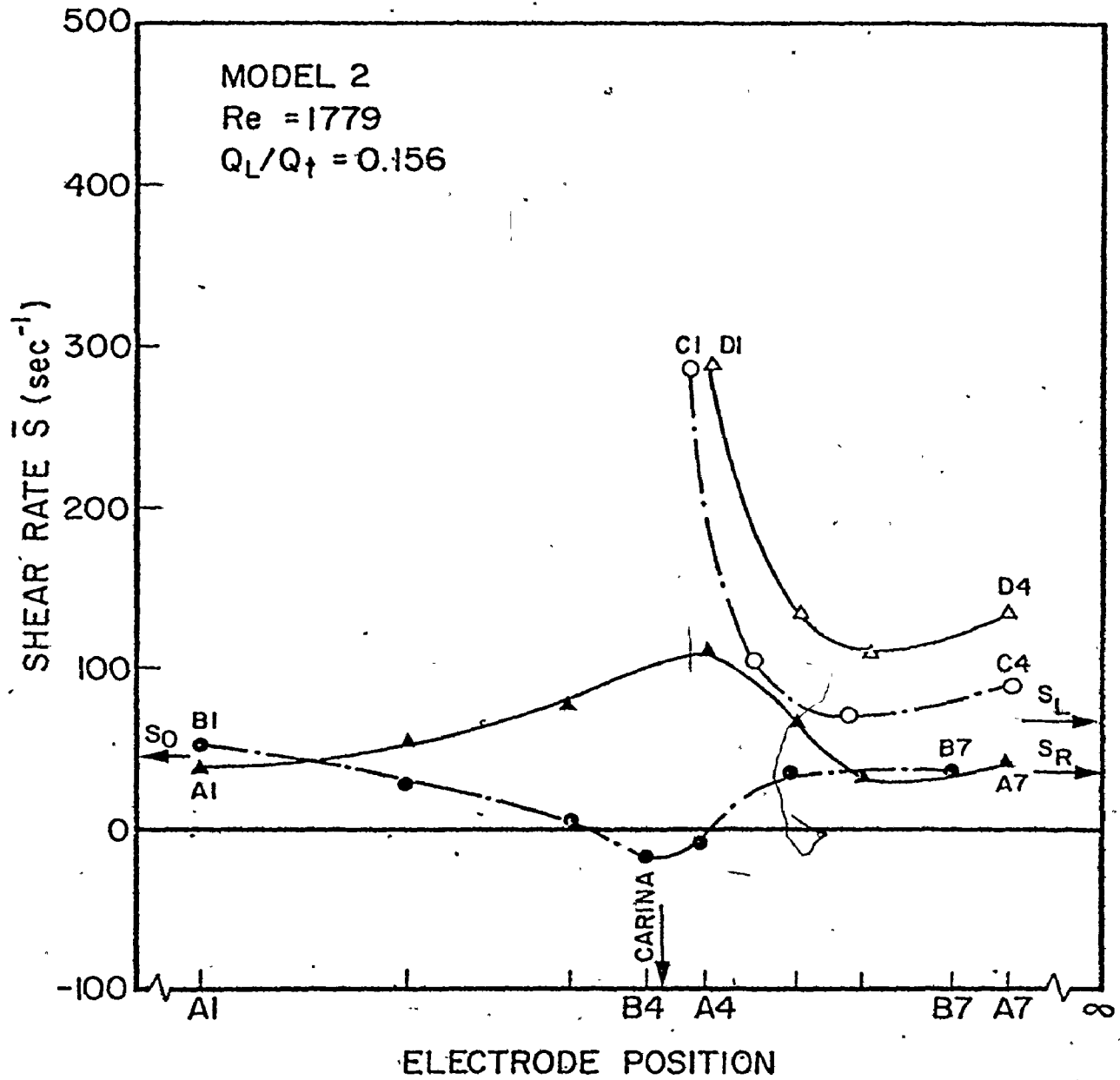
Figure 6.8   Shear Rate Distribution in Model 2.
Electrode Positions from Figure 6.7.

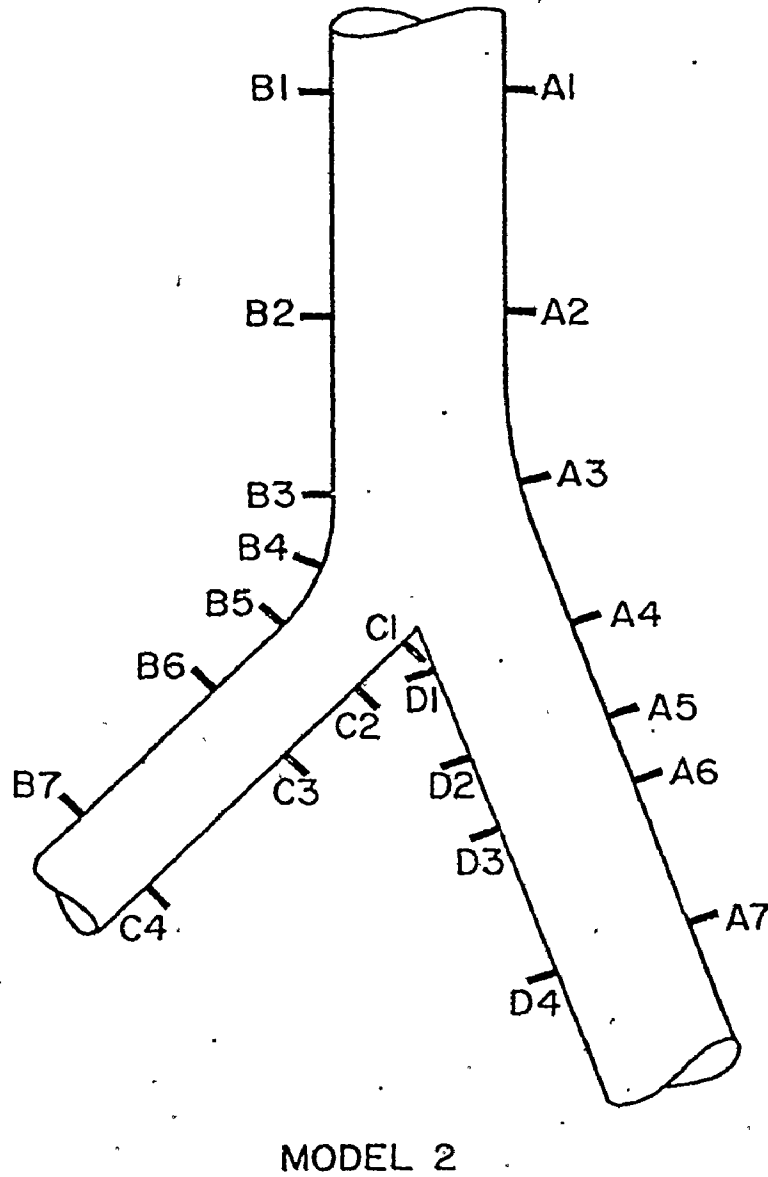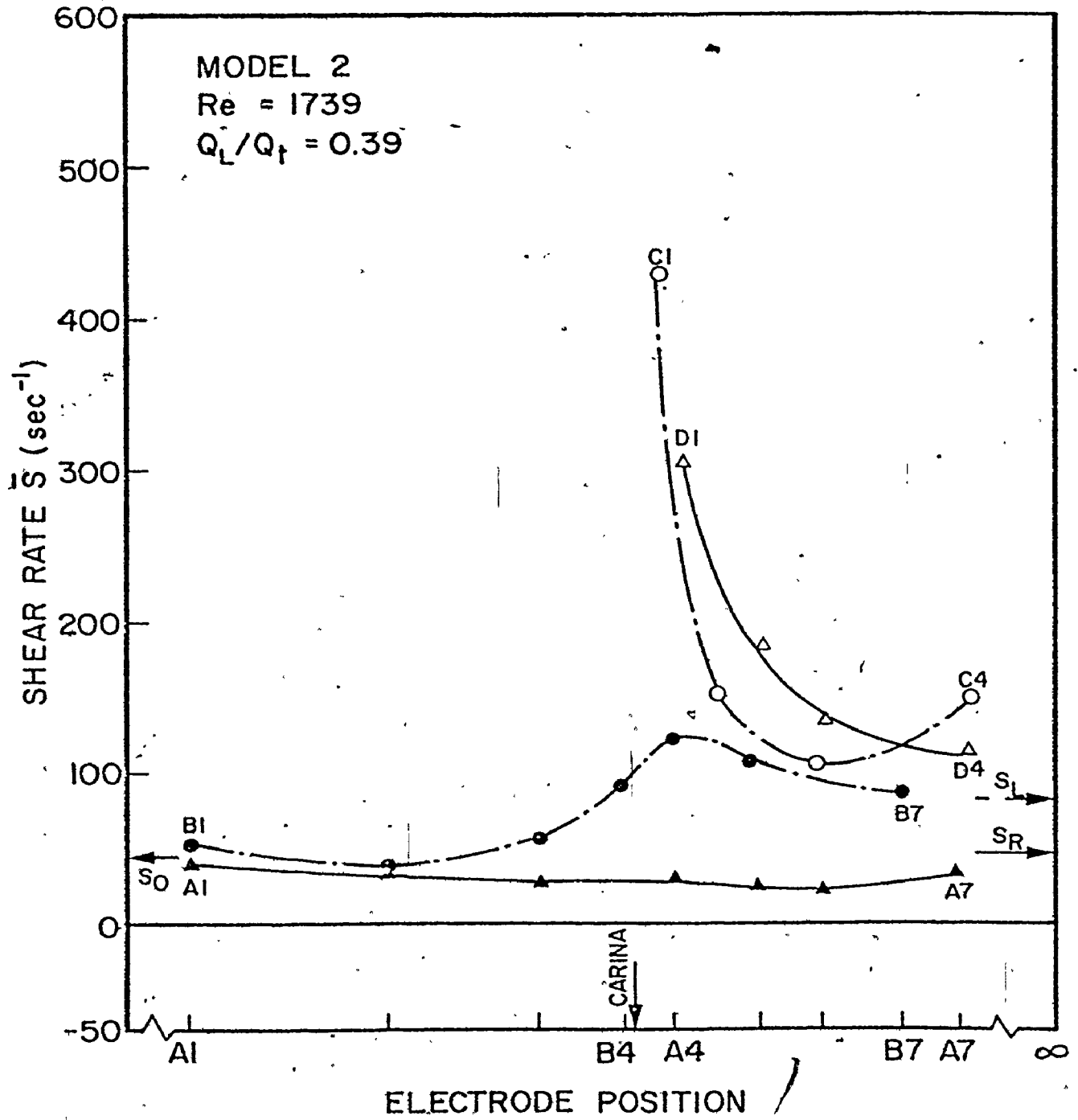Figure 6.9   Shear Rate Distribution in Model 2.
Electrode Positions from Figure 6.7.
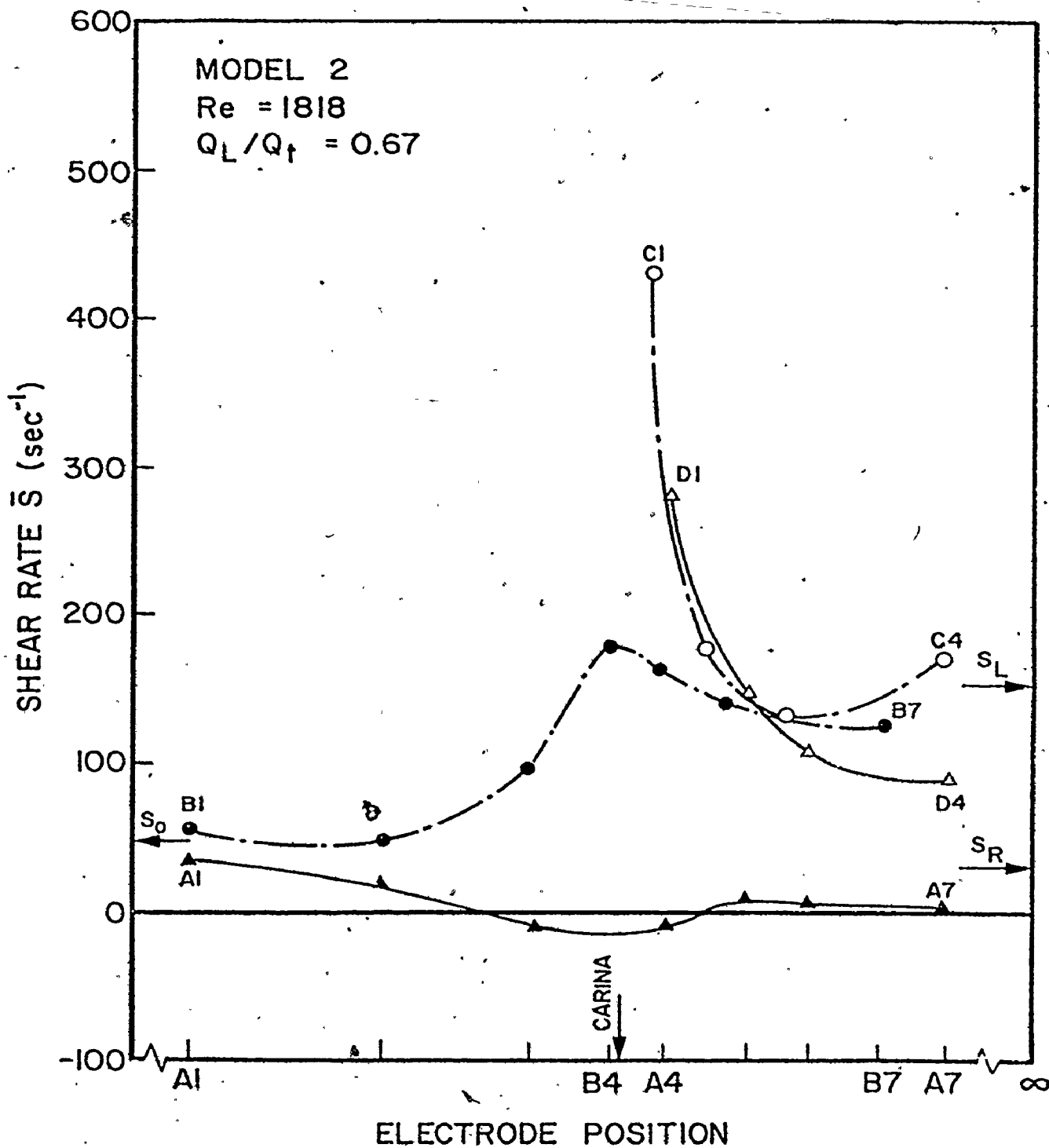
Figure 6.10   Shear Rate Distribution in Model 2.
Electrode Positions from Figure 6.7.

The general shape of the shear rate patterns on both
sides of the flow divider (walls C and D) were similar to
each other and to that on the flow divider of Model 1. The
shear rate was always highest at the leading edge of the flow
divider and fell off abruptly with distance downstream,
analogous to flow over a flat plate. Variations in the flow
division ratio did not have an effect on the general pattern
of shear along the walls of the flow divider. However, they
influenced its magnitude at some locations. An increase in
the left branch flow rate caused a rise in the shear rate value
at electrode C1 from 285 sec^{-1} to 435 sec^{-1} upon increasing
the flow ratio (Q_i/Q_t) from 0.156 to 0.67. However, the same
change in the flow conditions caused almost no change in the
shear rate measured at electrode D1 on the opposite side of the
flow divider. This was probably due to the difference
between the take-off angles of the two branches. The right
branch with a small take-off angle (20°) can be considered as a
continuation of the parent tube. Secondary flows formed on
the outside of this branch were not expected to be strong
enough to influence the value of the velocity approaching the
branch inside wall (wall D) which was a function of the upstream
flow rate only. Unlike the right branch, the left branch
had a large take-off angle (45°) and strong secondary flows
were expected to help the flow maneuvering its way into the
branch. These secondary flows were a function of the flow
division ratio and they were expected to influence the velocity
approaching the branch inside wall (wall C).
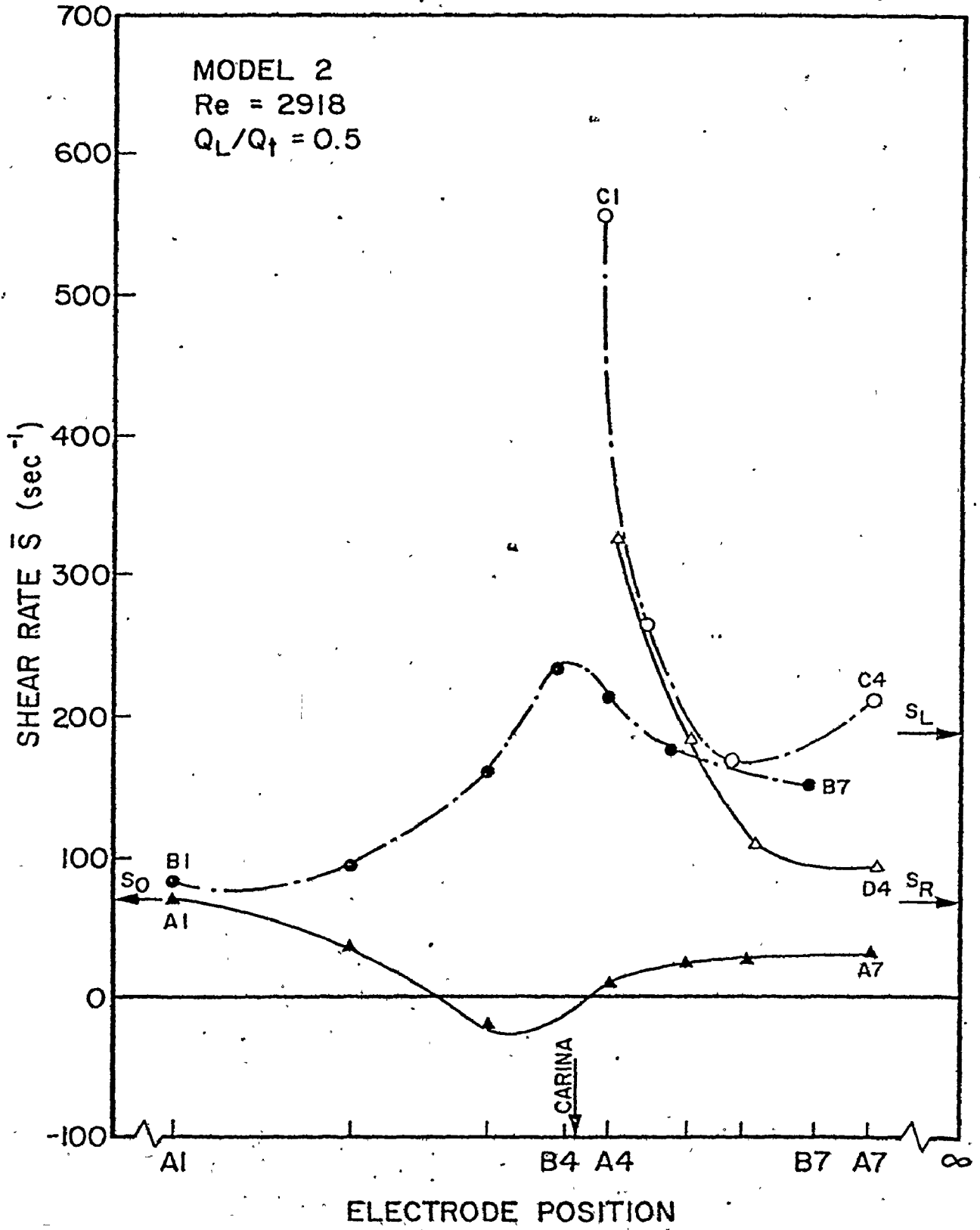
Figure 6.11 Shear Rate Distribution in Model 2.
Electrode Positions from Figure 6.7.

A significant change can be observed in the shear rate pattern on the outside walls upon varying the ratio of the flow division. At low ratio (Figures 6.8, $Q_L/Q_t=0.156$) the shear rate on wall B dropped significantly to its zero level upon the formation of the separated flow vortex, whereas shear rate on the other wall (wall A) rose gradually to its maximum level near electrode A4. At high flow ratio (Figure 6.10 $Q_L/Q_t=0.67$) a completely different shear rate pattern resulted. The shear peak was formed on wall B near electrode B4 instead whereas it dropped to its zero level and changed its direction on wall A. The intermediate flow ratio in Figure 6.9 showed a transition pattern between those of the low and high flow ratios.

An increase in the total flow rate (Figure 6.11, Re = 2918) resulted in an increase in shear values at the entrance section and over the flow divider, however, the increase over electrodes C1 and D1 was less than expected. This may be due to the fact that the approaching velocity for turbulent flow (Re = 2918) is less than that for laminar flow at the same flow rate (more flatter profile).

6.1.3 Wall Shear Rate Distribution in Model 3

Figure 6.12 shows Model 3 and the locations of various electrodes implanted into the walls of this model. This model represents a 45° side branch emanating from the main tube. The straight continuation of the main tube downstream of the carina is referred to as the right branch and the side branch is referred to as the left branch. The straight wall of the
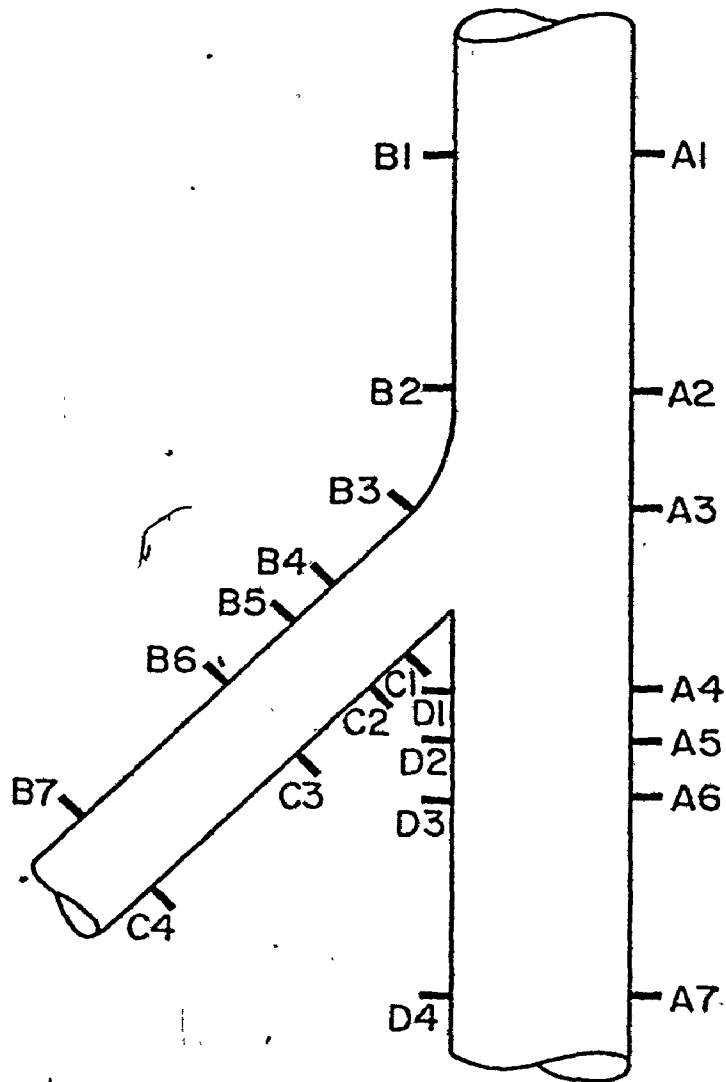
MODEL 3

Figure 6.12   Positions of Test Electrodes Imbedded
in the Walls of Model 3.

main tube is wall A whereas the opposite outside wall of
the model is wall B. Walls C and D are the flow divider
walls in the left and right branch respectively.

The wall shear patterns for three different values of
flow ratio are shown at a common parent tube Reynolds number
of 1672, in Figures 6.13-6.15. The low flow ratio Q_L/Q_t = 0.11
resulted in flow separation on the outside wall of the side
branch, wall B, while the other two flow ratios (Q_L/Q_t = 0.34
and 0.48) resulted in flow separation on the main tube outside
wall (wall A), see the results of the visualization study
(Figure 4.13). The shear rate pattern on wall B was greatly
influenced by the flow rate in the side branch. If the branch
flow rate was decreased below the critical separation value
(given by Figure 4.13), then the shear rate decreased pro-
gressively towards its zero level (separation point) near
electrode B4 and changed its direction within the separation
region. Conversely, if the side branch flow rate was increased,
then the shear rate increased progressively and a shear peak
was observed near electrodes B4 and B5. Compared with the
outside wall of the side branch, the shear rate pattern on the
outside wall of the main tube was uniform and its magnitude
was low. Also the change in the shear magnitude upon varying
the flow division ratio was small even when it changed its
direction as a result of the formation of separated flow.

On both walls of the flow divider, the shapes of the
shear patterns were similar, but the magnitudes varied. An
interesting result was that of the effect of flow ratio varia-

Figure 6.13   Shear Rate Distribution in Model 3.
                Electrode Positions from Figure 6.12.

Figure 6.14   Shear Rate Distribution in Model 3.
Electrode Positions from Figure 6.12.

Figure 6.15   Shear Rate Distribution in Model 3.
Electrode Positions from Figure 6.12.

tion on the shear rate values at electrodes D1 and C1 near
the flow divider lip. An increase in the side branch flow
rate caused an increase in shear value at electrode C1 and
a drop in the shear value at D1. This drop at D1 is in
contrast to the almost constant shear values measured at
electrode D1 of Model 2 upon variation of flow division. Unlike
Model 2 where Wall D was located at the centre of the parent
tube, Wall D in Model 3 is an extension of the parent tube
side wall and the approaching velocity is expected to be a
function of the forces directing the flow to this wall. These
forces are responsible for the secondary flow motion and are
a function of the flow ratio. The rise in the shear value at
electrode C1 upon increasing the side branch flow rate was
observed only up to a flow division ratio of $Q_L/Q_t = 0.34$.

In Figures 6.16 to 6.18, the flow ratio was kept constant
at approximately 0.25 while Reynolds number was varied. No
change in the shapes of the shear patterns on walls C and D
were observed. Although the shear magnitudes, especially
those at C1 and D1 were greatly influenced by changes in the
total flow rate. An increase in the total flow rate of about
75 percent (from Re = 948 to Re = 1672) caused more than a
four fold increase in the shear rate measured at electrodes
C1 and D1. However, when the high flow rate was almost
doubled (from Re = 1672 to Re = 3412), the percentage increase
in shear rate was 50% at electrode D1 and only 22% at electrode
C1. This irregular increase in the shear rate upon increasing
the total flow rate is probably due to the transition of the

Figure 6.16   Shear Rate Distribution in Model 3:
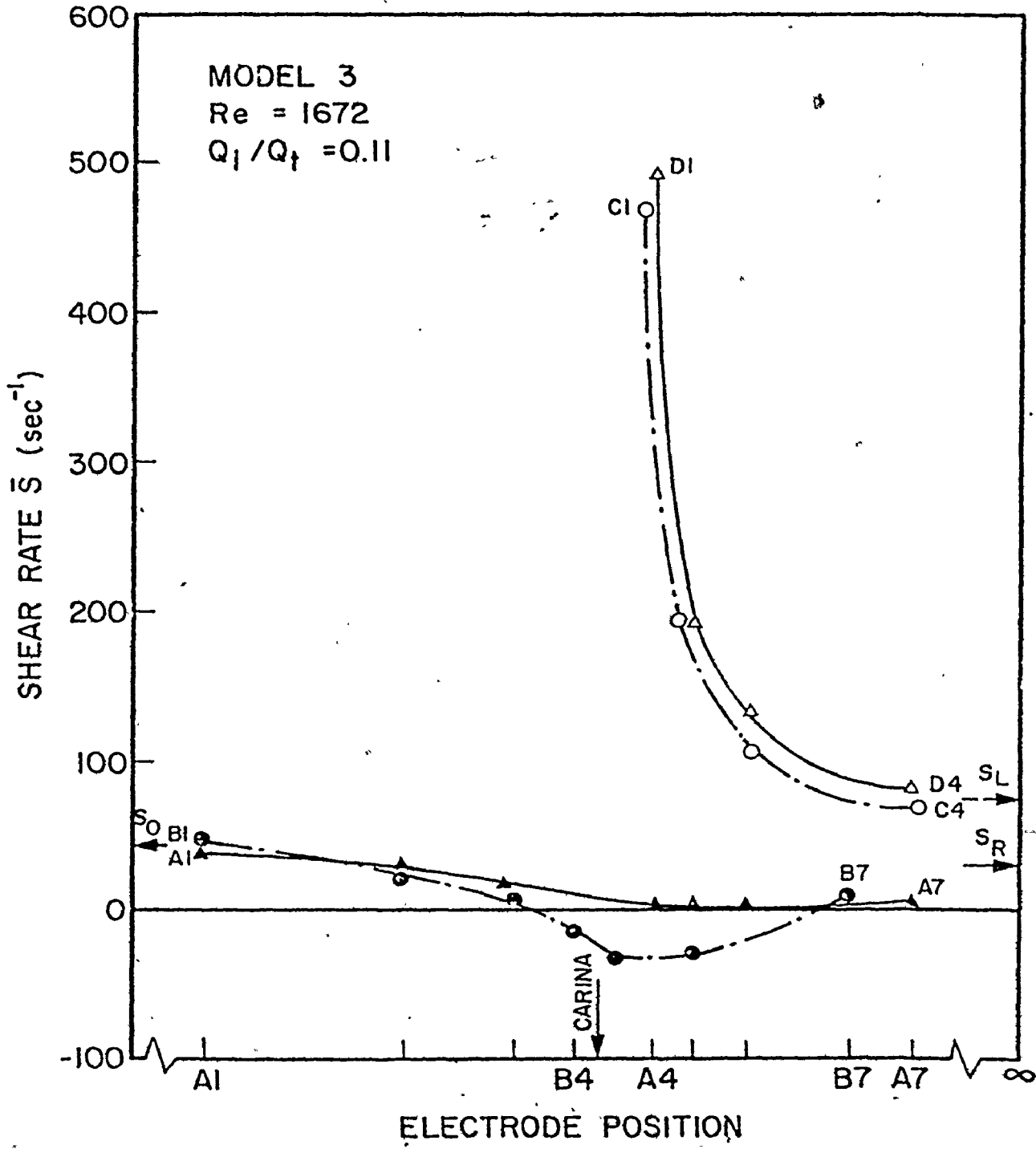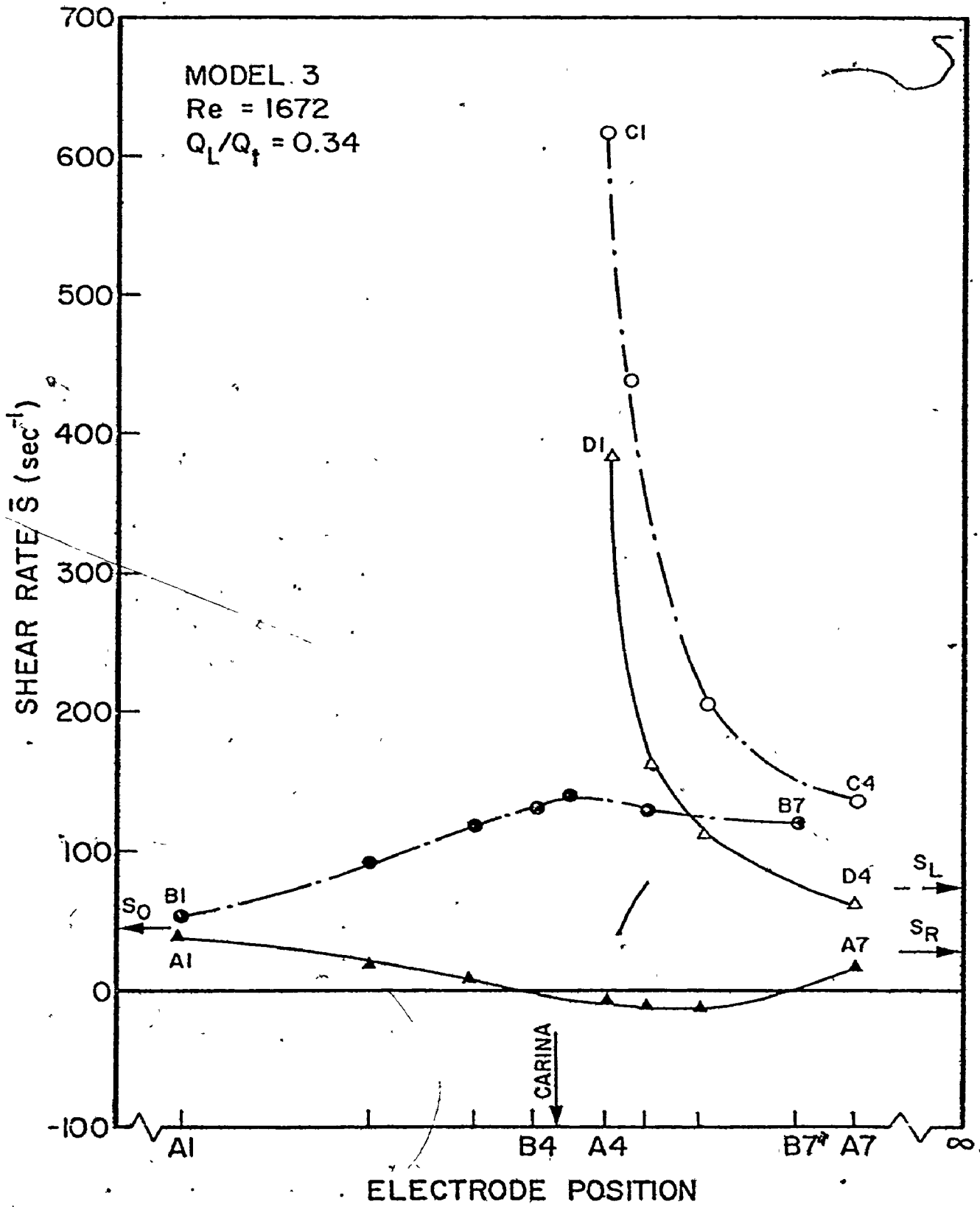Electrode Positions from Figure 6.12.

Figure 6.17   Shear Rate Distribution in Model 3.
          Electrode Positions from Figure 6.12.

Figure 6.18 Shear Rate Distribution in Model 3.
Electrode Positions from Figure 6.12.

flow from a laminar to turbulent regime. The shear rate at the leading edge of the flow divider is a function of the approaching velocity profile in the upstream inlet tube. Since the velocity profile for fully developed turbulent flow in a circular pipe has a flatter velocity profile than that for laminar flow, the approaching velocity for turbulent flow (Re > 2300) is expected to be less than that for laminar flow at the same flow rate.

Variations of the total flow rate were responsible for major changes in the shear patterns along the outside walls. A low Reynolds number (Re = 948) the shear pattern was unidirectional on both walls [Figure 6.16]. At a higher Reynolds number (Re = 1672) flow separation occurred at wall A and shear rate declined to its zero level then reversed its direction upon entering the separation region. At the highest Reynolds number (Re = 3412) flow separation occurred at both walls of the model (see Figure 4.13).

It is of interest to study the wall shear pattern in the model at high Reynolds numbers (Re $\geq$ 3000) and high flow division ratios ($Q_L/Q_t \geq$ .6). Under these flow conditions, a region of separated flow was observed in the flow visualization study on the inside wall of the side branch (near electrode C2), see section 4.1. Shear rate measurements at Re = 3412 and a flow ratio of .58 (Figure 6.19 did not show any distinctive change in the shear pattern near electrode C2. However, an increase in the flow ratio to a value equal to 0.64 (Figure 6.20) showed an abrupt drop in the shear value at

Figure 6.19   Shear Rate Distribution in Model 3.
                Electrode Positions from Figure 6.12.
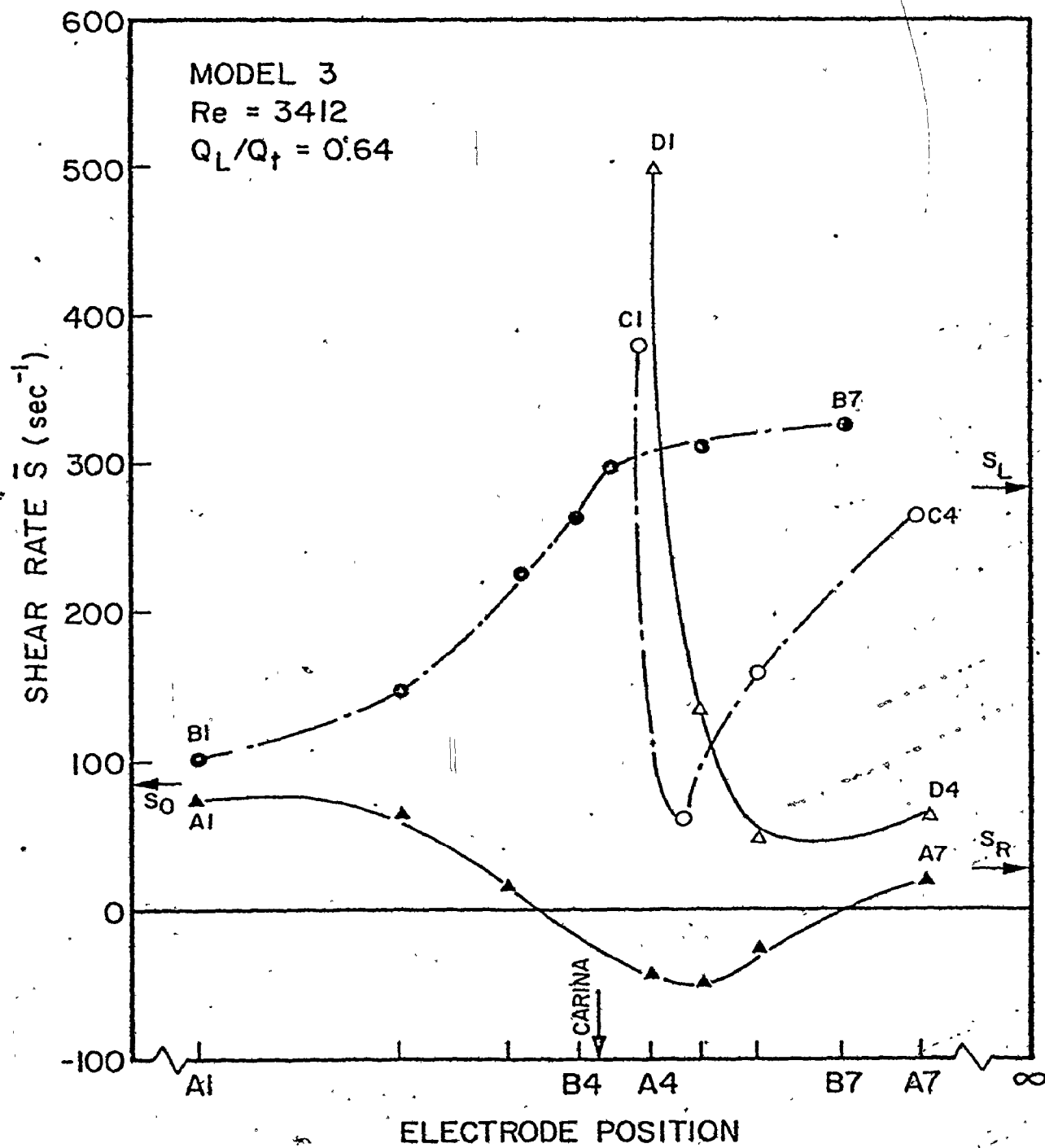
Figure 6.20 Shear Rate Distribution in Model 3.
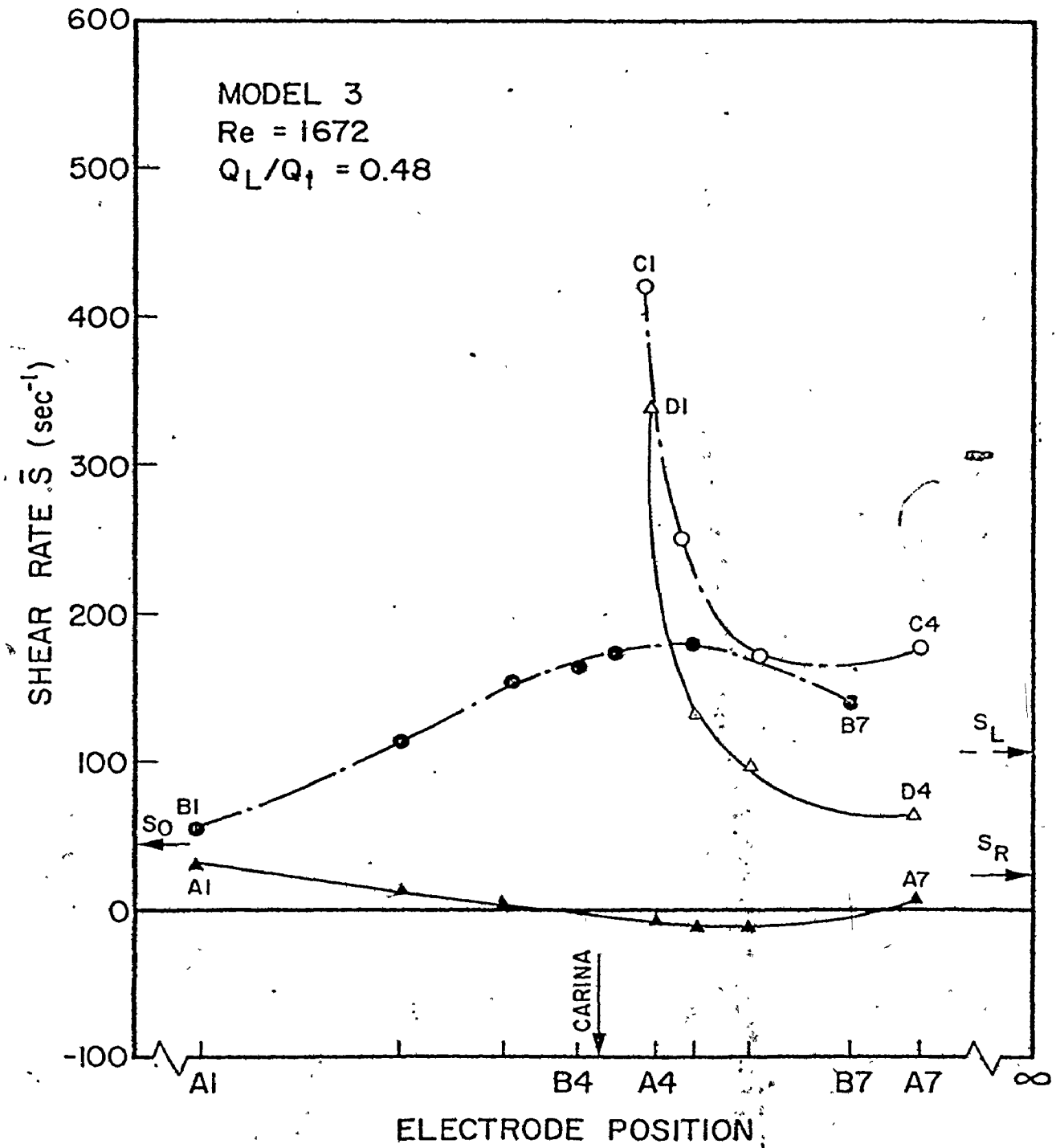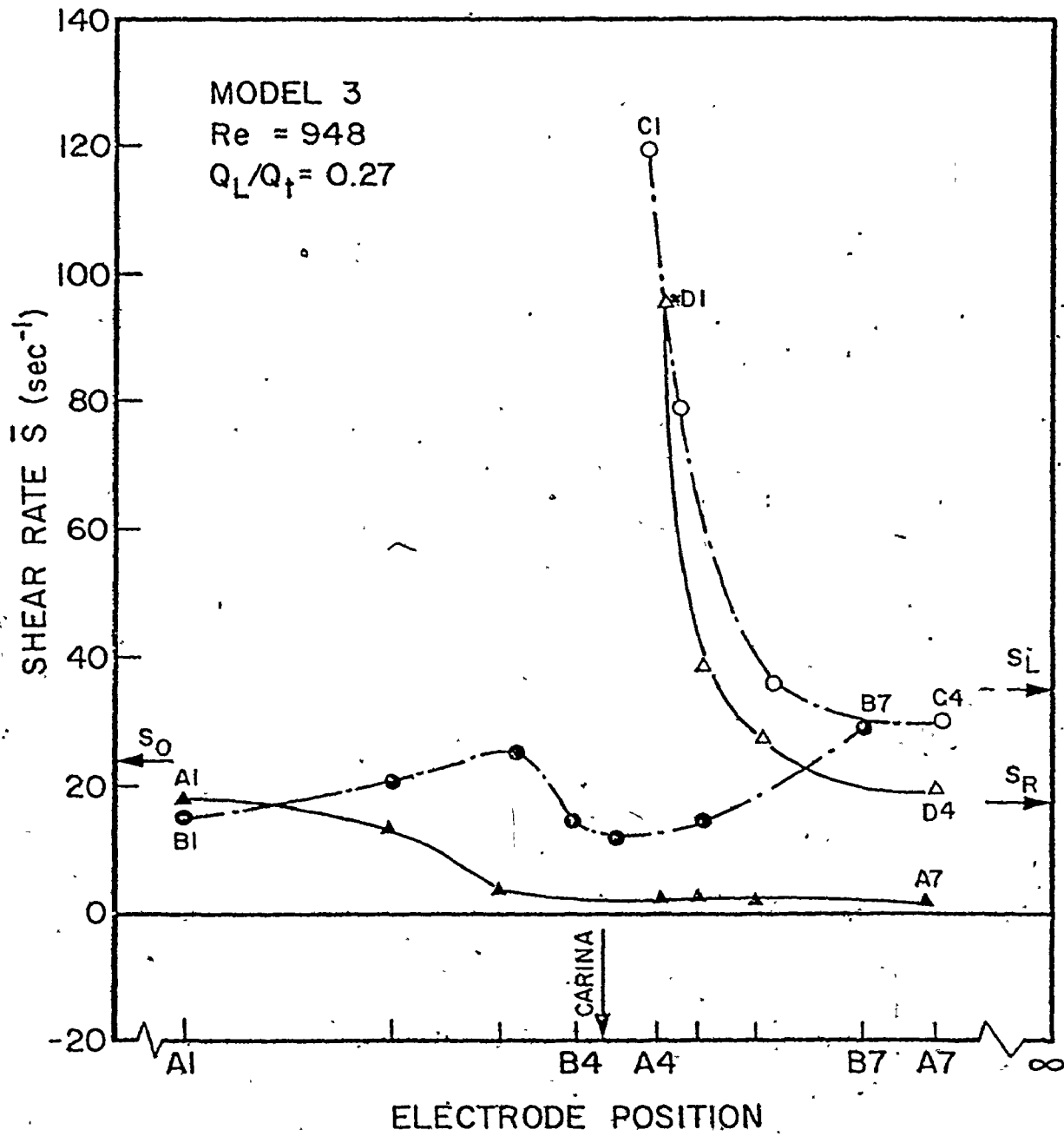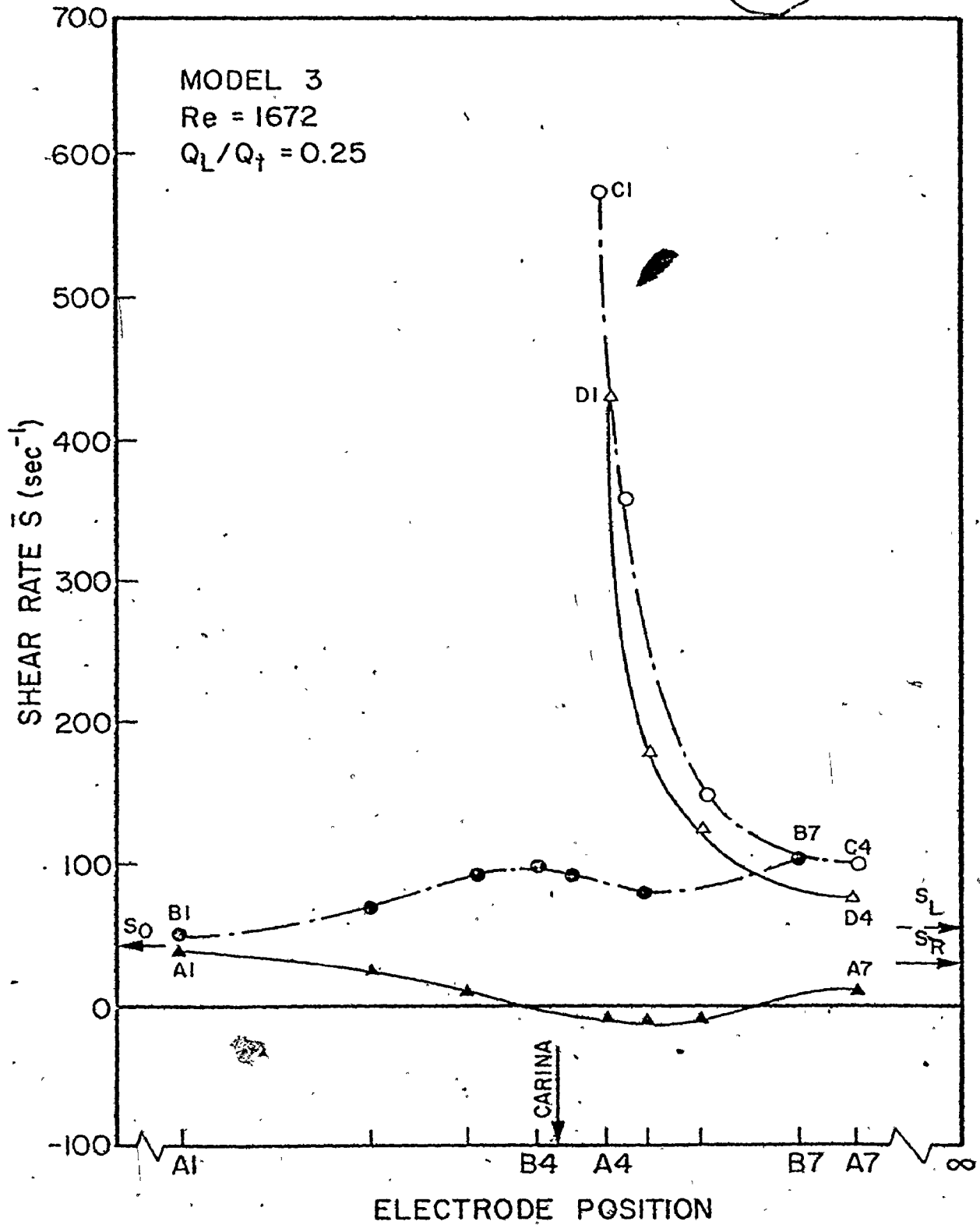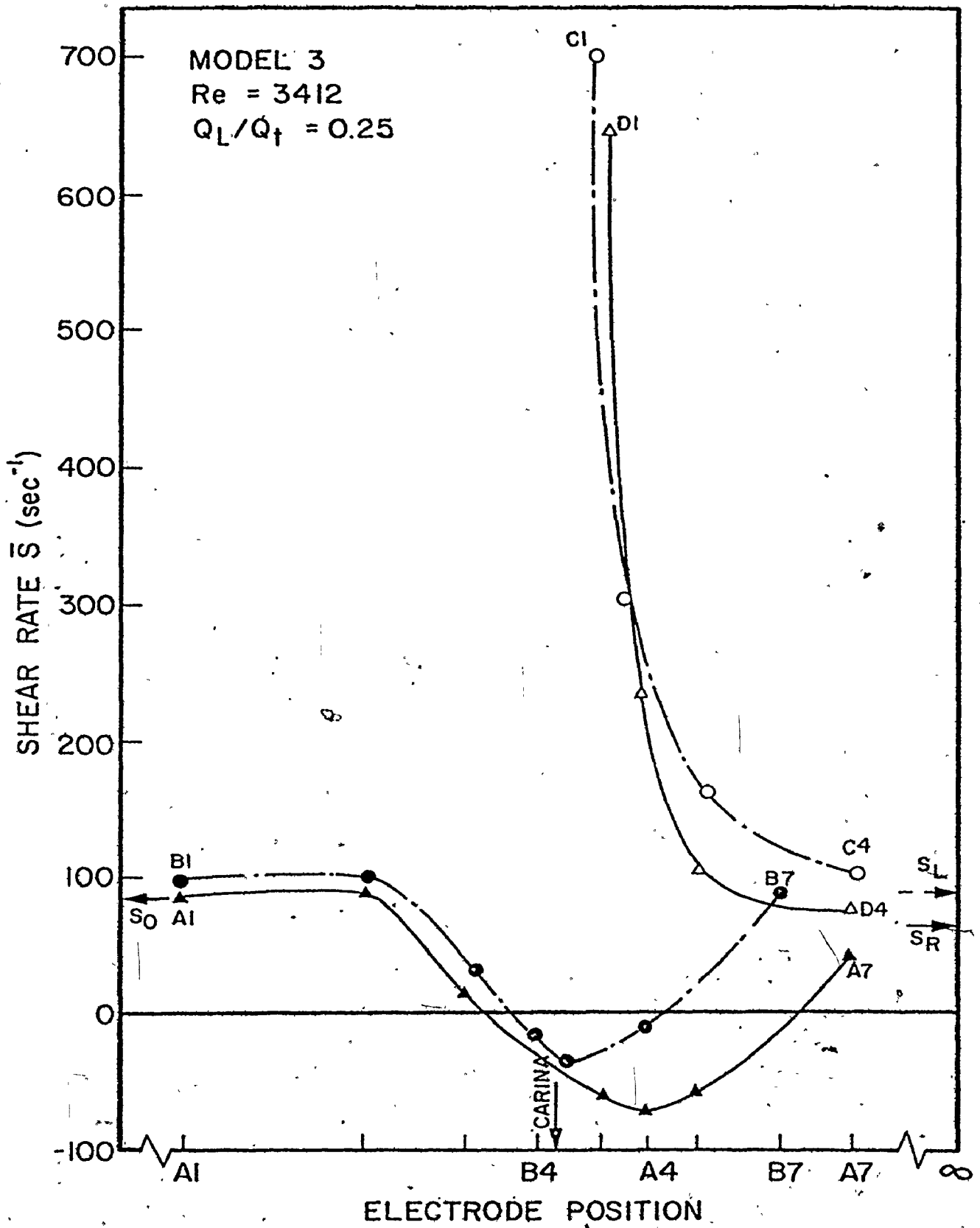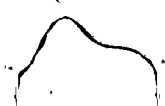Electrode Positions from Figure 6.12.

electrode C2. This indicates that the critical flow division ratio for separation flow on this wall is in the range of $Q_L/Q_t = 0.58 - 0.64$. A critical value of approximately $Q_L/Q_t = 0.6$ was predicted from the visualization study for this phenomenon (Figure 4.15).

6.1.4 Wall Shear Rate Distribution in Model 4

Figure 6.21 shows the locations of the test electrodes inserted through the walls of Model 4. This model is similar to Model 3 in that they both have a side branch emanating from a straight-walled main tube. However, the take-off angle and dimensions of the side branch are different. The side branch in Model 4 is representative of a single renal artery which takes off at a right angle to the aortic trunk. Comparison of wall shear rate patterns in both models provides for evaluation of the effect of take-off angle and side branch dimensions on shear rate pattern.

Shear rate distribution along the walls of Model 4 is given in Figure 6.22 at a Reynolds number equal to 1632 and a flow division ratio of 0.11. These flow conditions are within the physiological range of renal flow under rest conditions. The most striking feature of this shear pattern was the unexpected high shear values measured at electrodes B4 and B5 on the outside wall of the side branch. This site has been shown to experience negative and relatively small shear rates under the same flow conditions in Model 3 (Figure 6.13). This indicated that the higher take-off angle (90° compared to 45°)
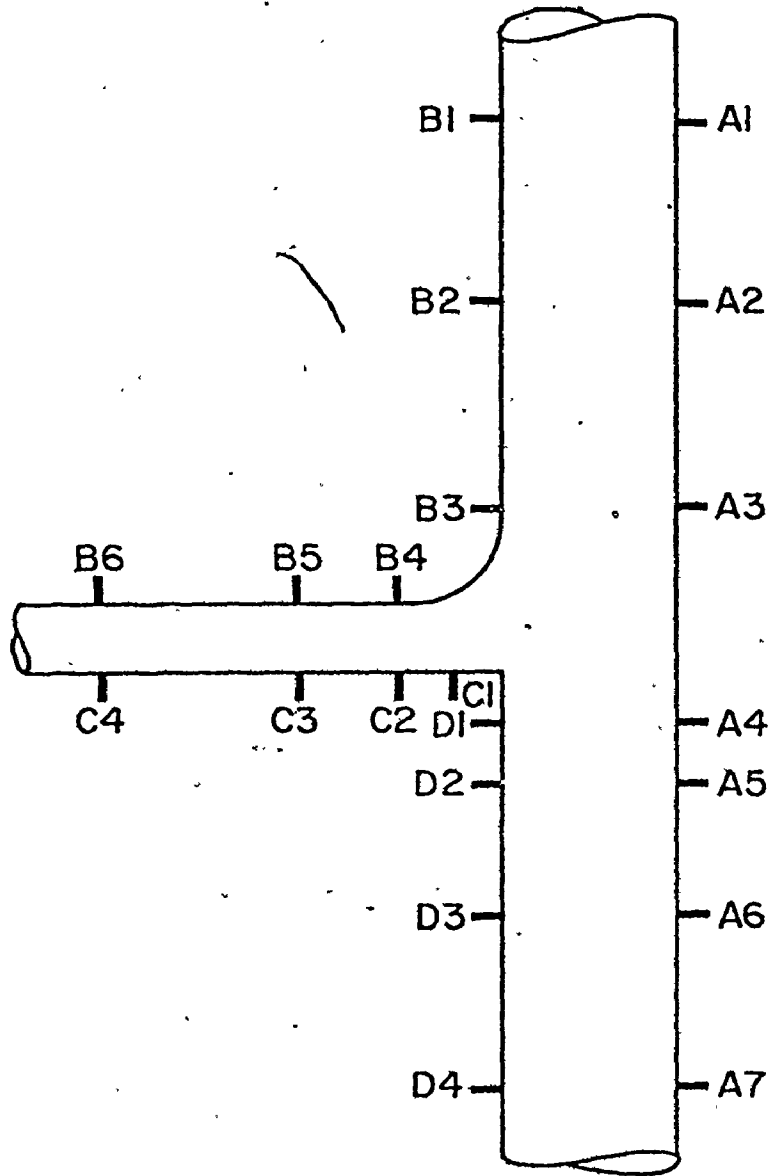
MODEL 4

Figure 6.21   Positions of Test Electrodes Imbedded
in the Walls of Model 4.
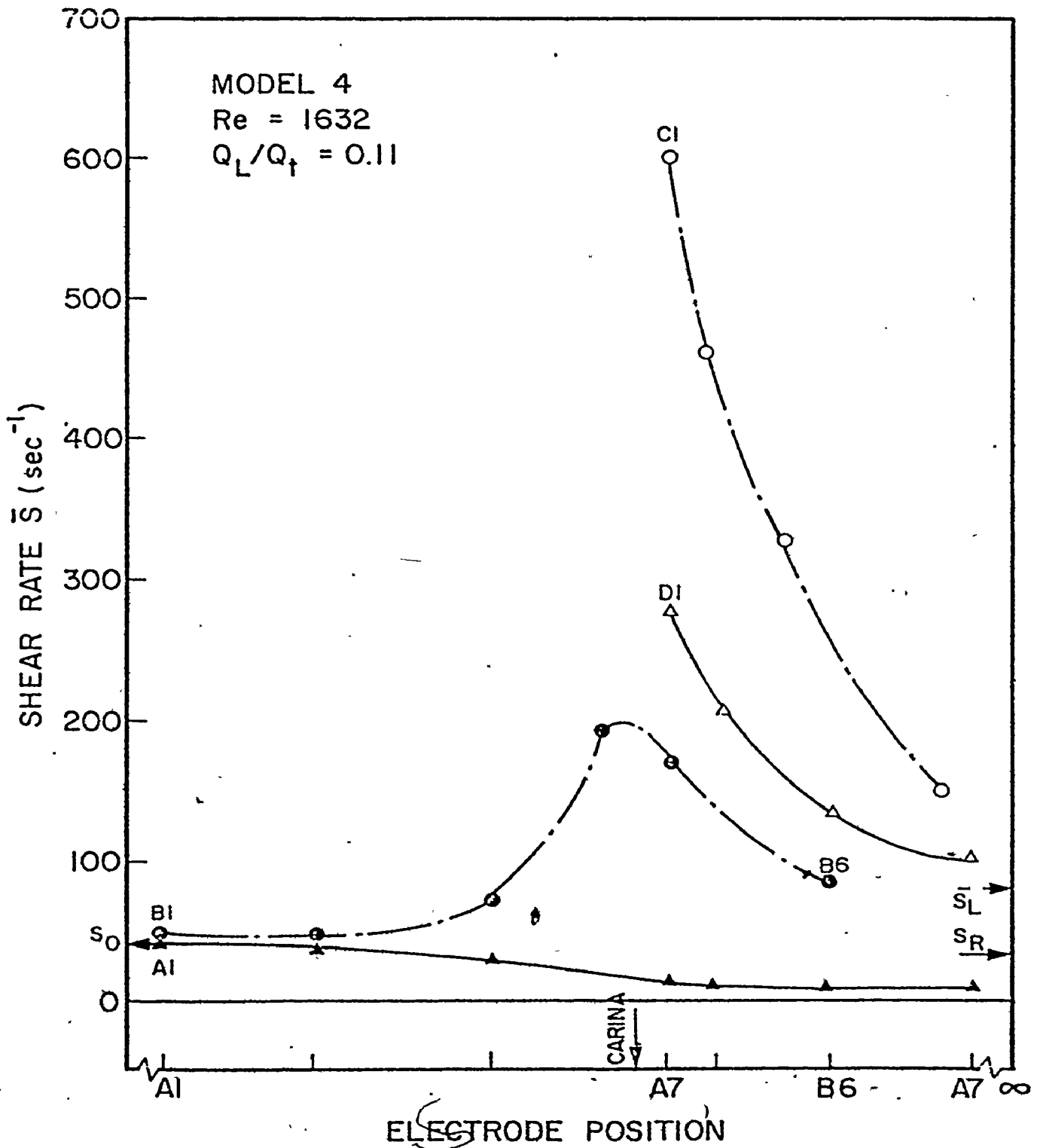
Figure 6.22   Shear Rate Distribution in Model 4.
              Electrode Positions from Figure 6.21.

and the smaller branch diameter (1.27 cm compared to 1.8 cm) resulted in a stronger secondary flow motion that prevented flow separation and caused a rise in the shear rate values at electrodes B4 and B5. These parameters were also responsible for steeper shear patterns compared to those in Model 3 on the walls of the flow divider (walls C and D).

Exercise is known to cause changes in blood flow distribution in the cardiovascular system. The increase in the cardiac output and the drop in the renal flow rate is an example [44]. Wall shear distribution along the walls of Model 4 under representative conditions of light exercise is given in Figure 6.23. The distinctive difference in the shear pattern from that under rest conditions (Figure 6.22) was observed in the shear distribution along the outside wall of the side branch. Flow separation occurred on this wall near electrode B3 and B4 as observed in the visualization study. This caused the shear rate to decline to its zero level. After reattachment it increased abruptly and reached a peak (210 sec^{-1}) within 1 cm distance downstream. This dramatic variation in the shear patterns, where both negative and positive low shear and high shear were found on the same wall in close proximity, is one of the interesting features of this model when compared with other models.

On the other hand, an increase in the side branch flow rate (Q_L/Q_t = 0.31) caused the shear peak on the side branch outer wall to increase to a high shear level (320 sec^{-1}) while the shear rate measured at electrode C1 was dropped to a value
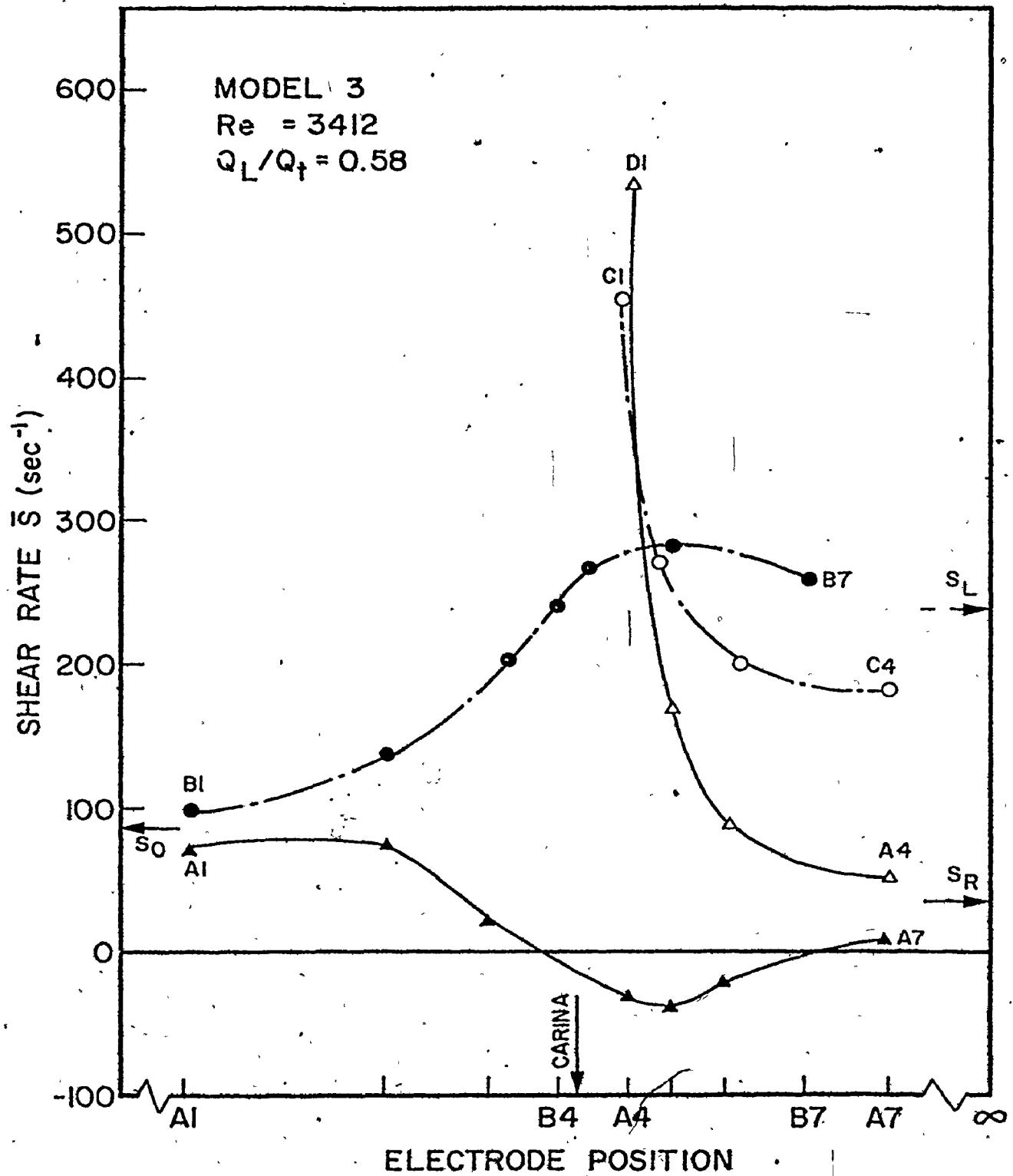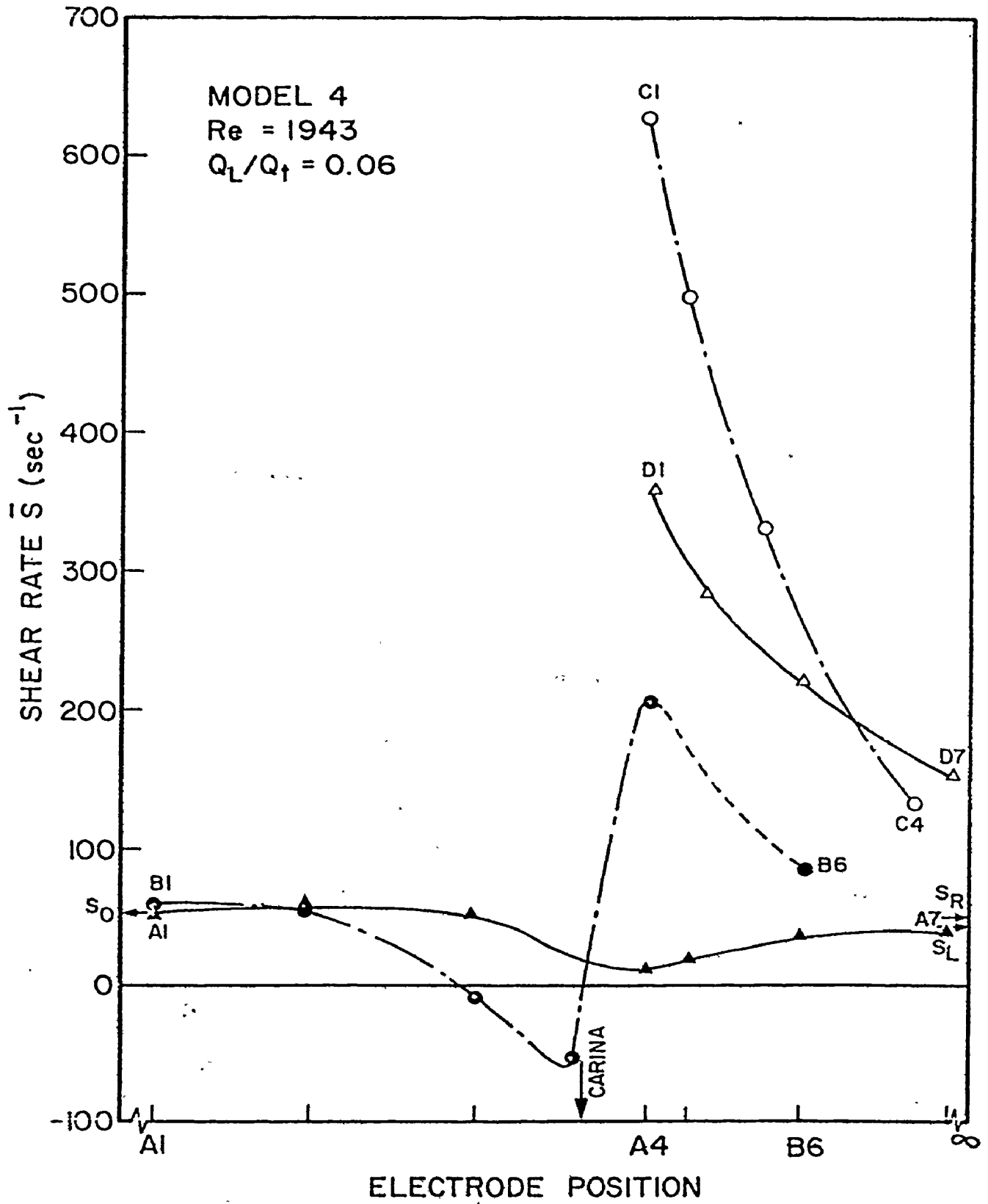
Figure 6.23   Shear Rate Distribution in Model 4.
Electrode Positions from Figure 6.21.
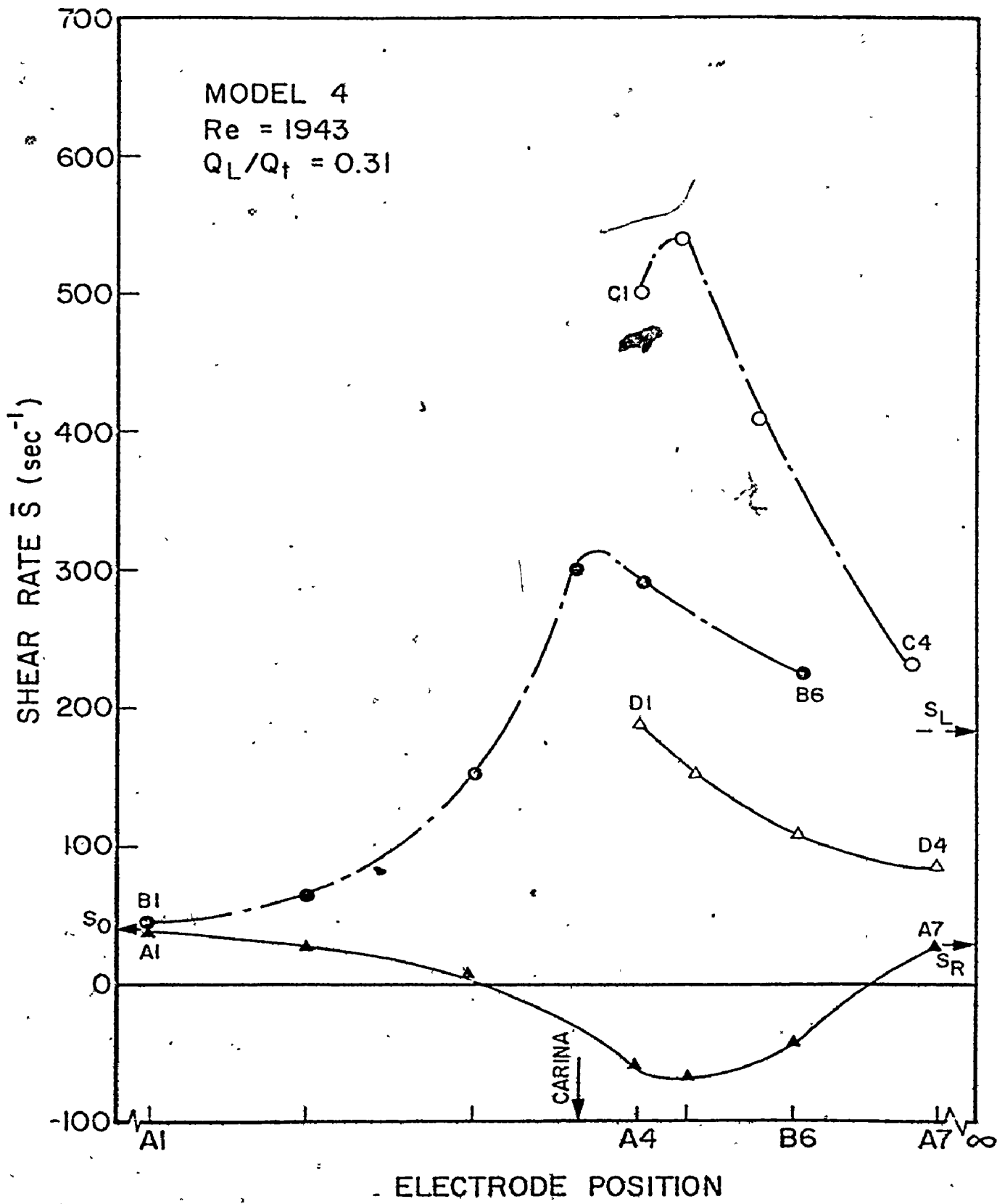
Figure 6.24   Shear Rate Distribution in Model 4.
Electrode Positions from Figures 6.21.

less than that measured at C2. An expected drop in shear
rate values along the walls of the main tube downstream of
the carina was also observed. This was due to the reduction
in this branch flow rate. (See Figure 6.24)

6.2 Shear Rate Fluctuations

Disturbed flow patterns near the vessel wall have
been implicated as key factors in atherogenesis [72]. Direct
evidence from electronmicroscopic studies of vascular endo-
thelium in swine have shown that endothelial cell injury and
loss occur at positions adjacent to disturbed flow regions
[60]. In recent in vitro studies [73, 74], fluctuations in
both pressure and shear stress were implicated as indications
of flow disturbances.

Values of wall shear rates reported in this study
were obtained through measurements of the current flowing in
the electrode circuit. This current is directly proportional
to the rate of mass transfer to the electrode surface and the
fluctuations in the current are also directly proportional to
fluctuations in the rate of mass transfer (see Section 5.2).
Since the thickness of the concentration boundary layer
for the system used here is much smaller than that of the
momentum boundary layer, fluctuations in the mass transfer
rate reflect fluctuations in the velocity field close to the
wall.

In order to qualitatively study the shear rate
fluctuations, experimental output from the different electrodes
was displayed on the oscilloscope screen and was also recorded.

This output was the voltage drop across a standard resistance and was proportional directly to the electrode current. Examples of the output signals from electrodes of Model 1 are presented in this section.

Figures 6.25 and 6.26 show signals from electrodes A2-A7 on the outside wall of Model 1 (positions of these electrodes are given in Figure 6.1) at approximately the same Reynolds number (Re $= 1943$ and 1964 for Figures 6.25 and 6.26 respectively) while flow division ratios are different ($Q_i/Q_t = 0.5$ and 0.33). For the higher flow ratio ($Q_i/Q_t = 0.5$, Figure 6.26), fluctuations of small and constant frequency (2-3 c/sec) and small amplitude were present on electrodes A4-A6, though flow separation was not expected to occur under these flow conditions (see Figure 4.11). When the flow division ratio was reduced ($Q_i/Q_t = 0.33$, Figure 6.26) to induce separation in this branch, fluctuations on electrodes A5 and A6 became more irregular with a noticeable increase in their amplitude. This phenomenon was observed in all the models under separated flow conditions.

There existed a local area on the outside wall which showed wide ranges of shear rate magnitude and fluctuation depending on the flow conditions in the branch vessel. The region near electrode A5 could represent either low (positive or negative) or high shear stress, and possibly zero shear stress (reattachment point). This can be seen from Figure 6.27 where the absolute shear rate values were normalized by dividing by the upstream fully-developed shear rate (proportional

MODEL 1 OUTSIDE WALL
Re = 1943 Q_i/Q_t = 0.5

Figure 6.25   Current Fluctuations from Electrodes on the
Outside Wall of Model 1:   Electrode Positions
are given in Figure 6.1.

MODEL I OUTSIDE WALL

Re = 1904 Q_i / Q_t = 0.33
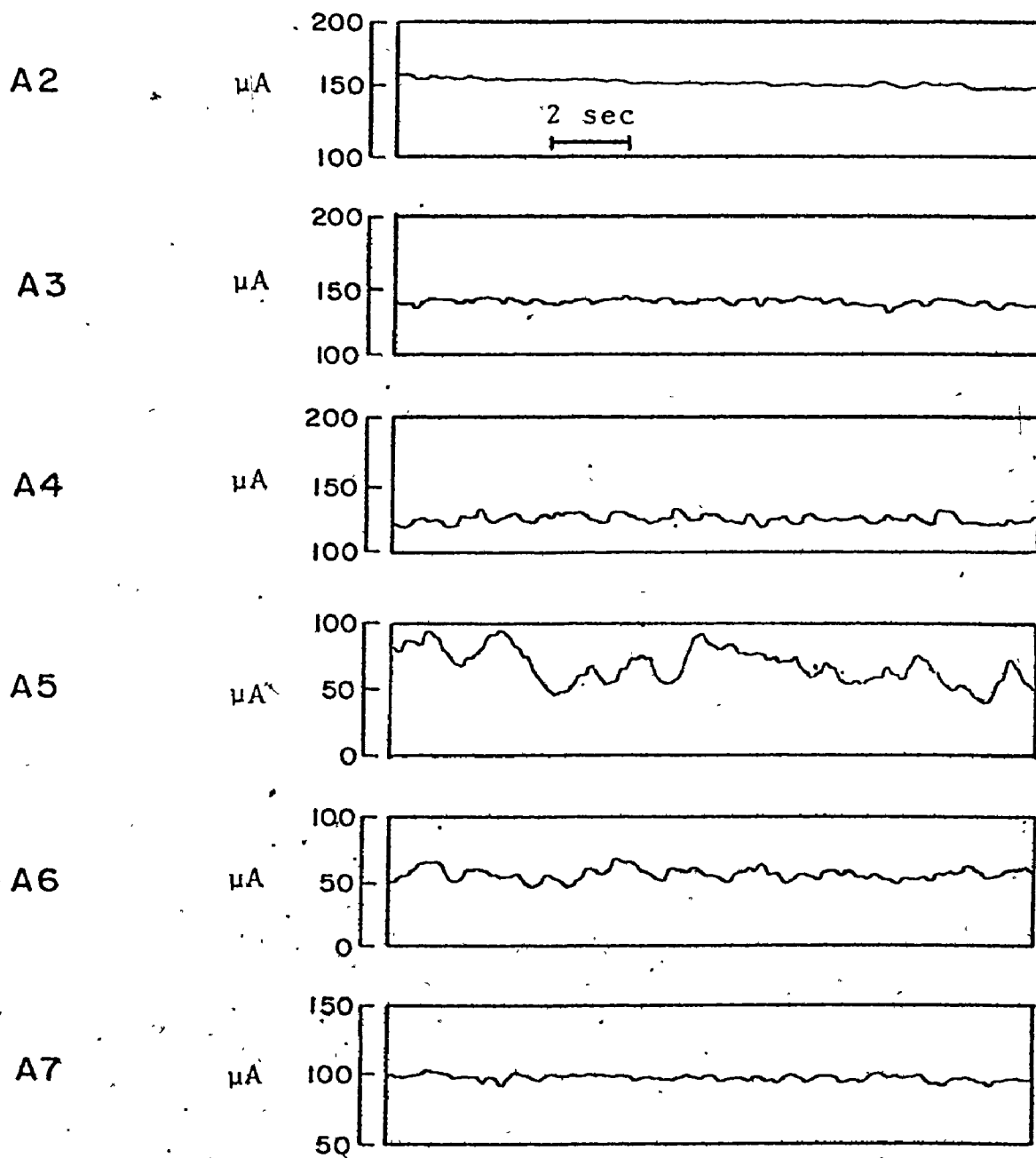
Figure 6.26 Current Fluctuations from Electrodes on the Outside Wall of Model 1. Electrode Positions are given in Figure 6.1.
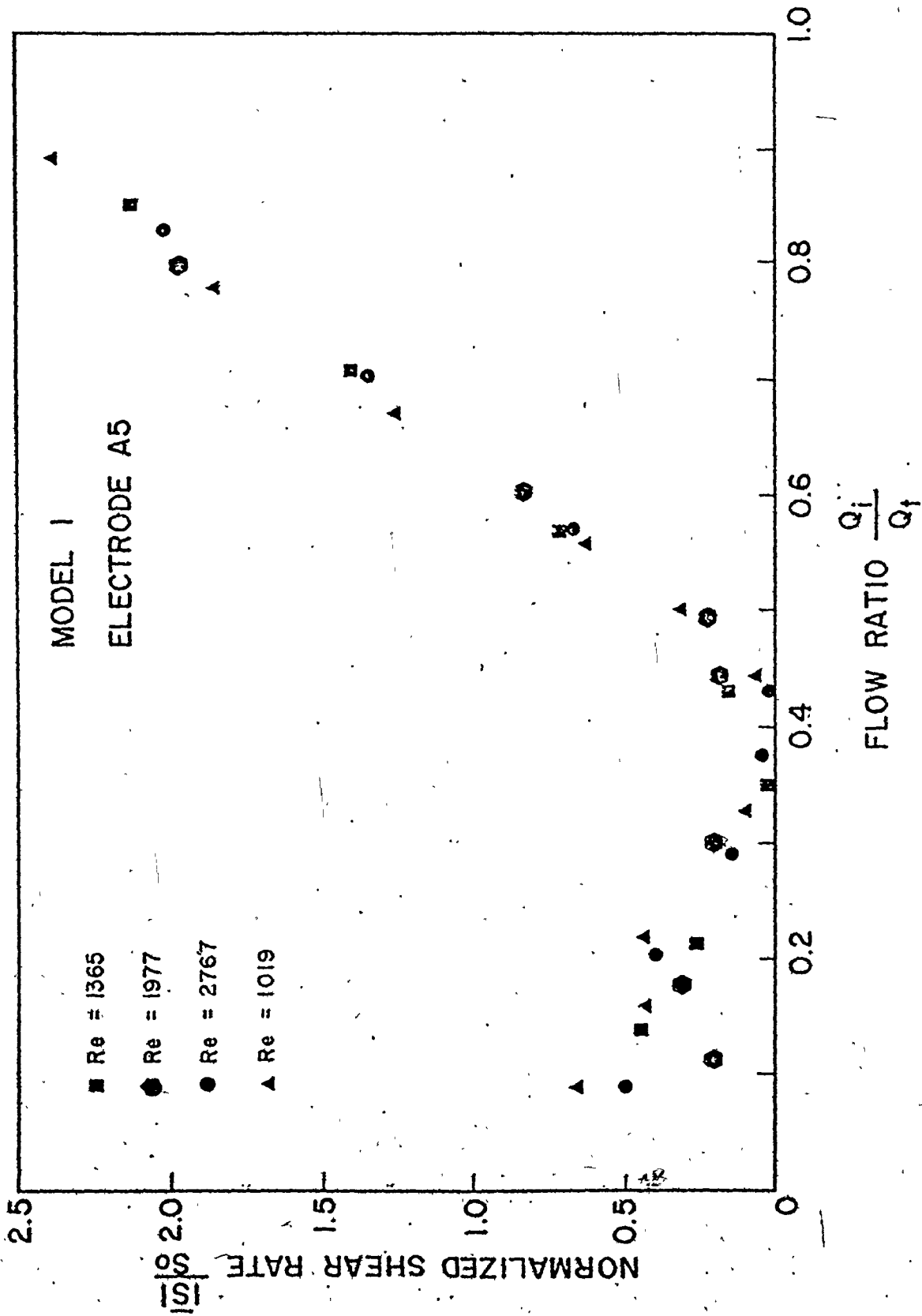
Figure 6.27 Normalized Absolute Values of Shear Rate for Electrode A5 as a Function of Flow Ratio Q_i/Q_t.

MODEL I   ELECTRODE A5
Re = 1977

$Q_i/Q_t = 0.3$ μA

$Q_i/Q_t = 0.4$ μA

$Q_i/Q_t = 0.5$ μA

$Q_i/Q_t = 0.6$ μA

$Q_i/Q_t = 0.7$ μA

$Q_i/Q_t = 0.8$ μA
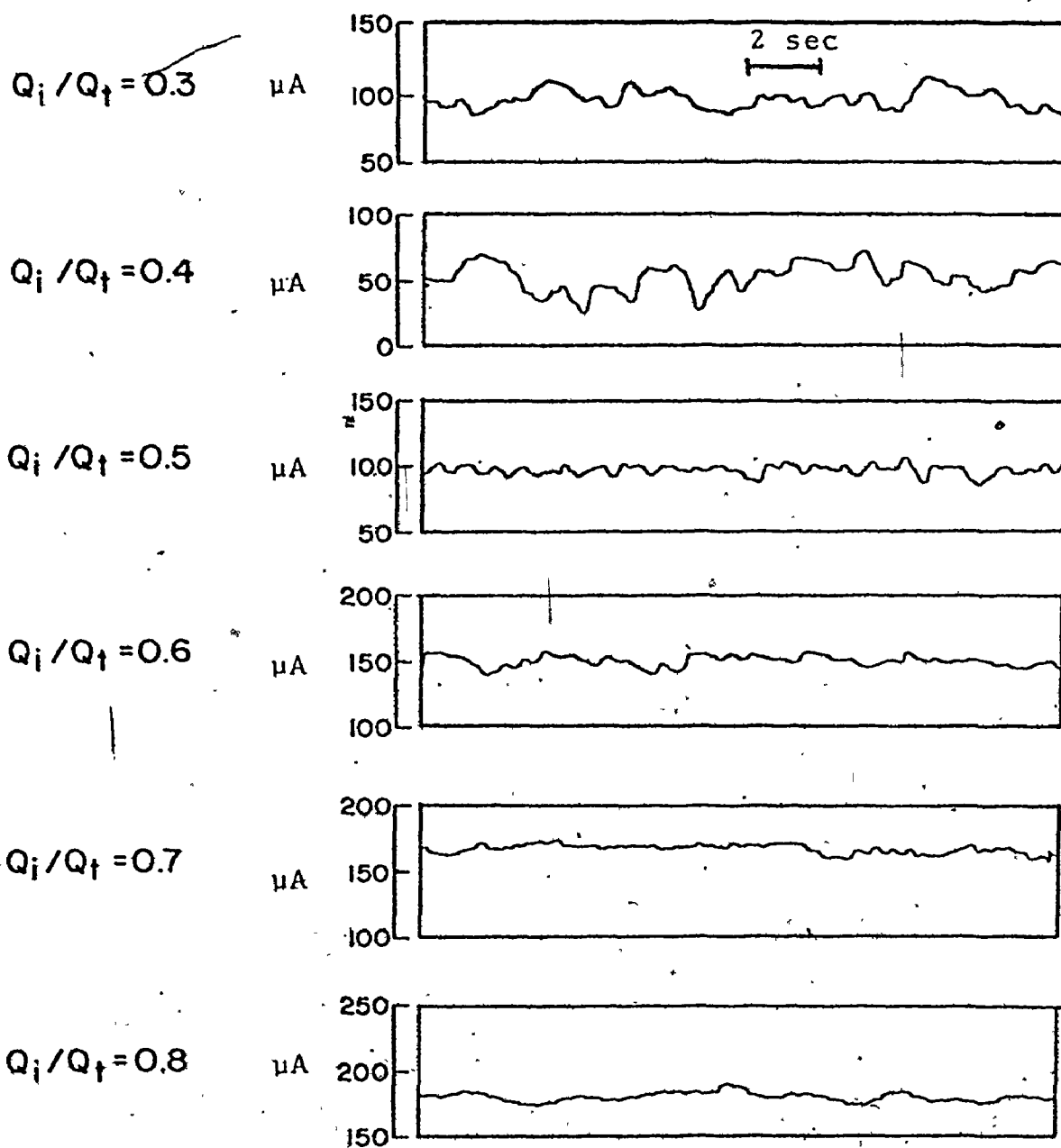
Figure 6.28 Current Fluctuation from Electrode A5 of
Model 1 at Different Q_i/Q_t Values.

to Reynolds number). Prior to separation ($Q_i/Q_t > 0.4$) the plotted data showed that the normalized shear rate was dependent and directly proportional to the flow division ratio Q_i/Q_t. However this relationship was not present over flow-separation conditions ($Q_i/Q_t < 0.4$). Fluctuations in the shear rate pattern were also dependent on the flow division ratio. Figure 6.28 shows these fluctuations presented by samples of the current signals for different Q_i/Q_t values. At low flow ratio ($Q_i/Q_t \leq 0.4$) the current signals were unstable and showed irregular fluctuations of relatively high amplitude. As the flow ratio increased ($Q_i/Q_t > 0.4$), the current signals became reasonably steady and stable.

Fluctuations in the shear pattern over the flow divider wall can be seen from the current signals of electrodes inserted along this wall (Electrodes D1-D4). Figure 6.29 shows these signals at two different Reynolds numbers (Re = 1826 and 3342). At the lower Reynolds number the signals were reasonably steady while at the higher Reynolds number fluctuations were present. These fluctuations had relatively higher frequencies when compared with fluctuations observed on the outside wall. This difference suggests a difference in the cause of fluctuation. Fluctuations observed on the flow divider wall at high Reynolds number (Re = 3342) may be due to the flow being in the turbulent regime while fluctuations observed on the outside wall at much lower Reynolds number are the result of local instabilities associated with flow separation [51].
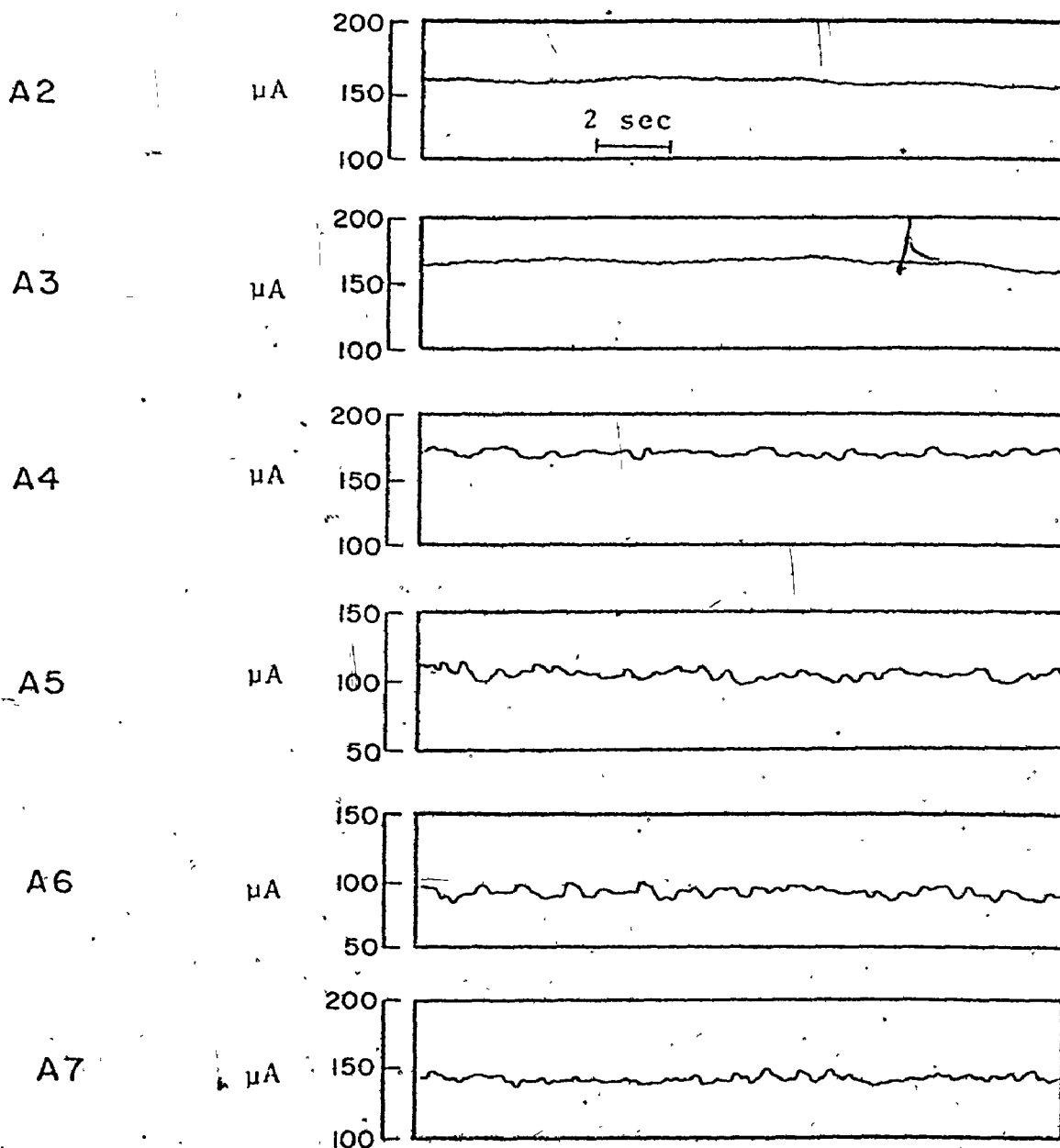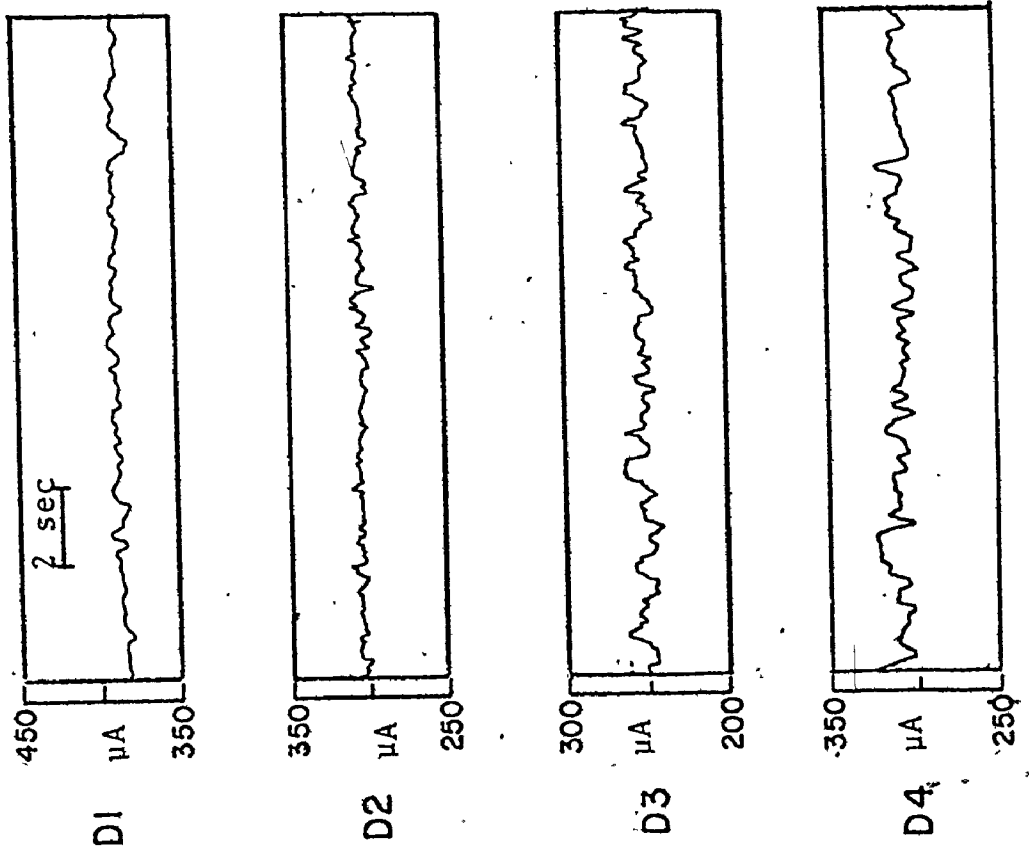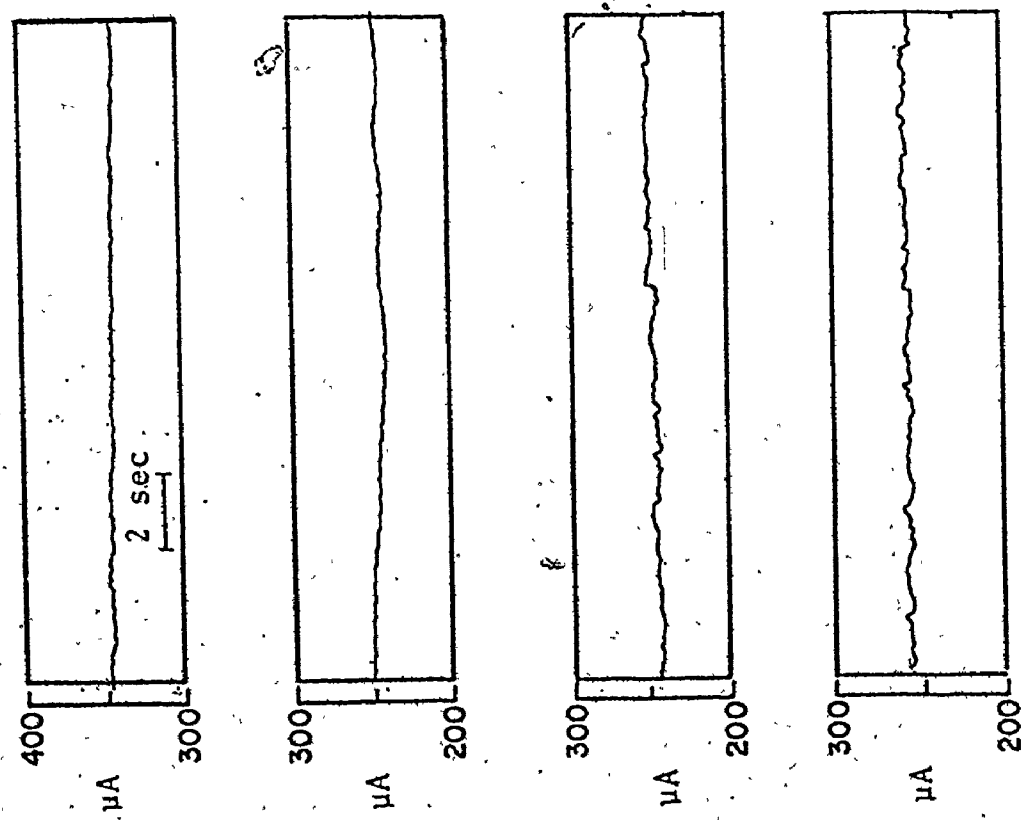
Figure 6.29 Current Fluctuation from Electrodes on the Inside
Wall of Model 1. Electrode Positions are given
in Figure 6.1.

6.3 Pulsatile Flow

Depending on the magnitude and stability of the shear stress pattern as well as the duration of exposure to the stress, certain intimal structural and functional changes have been shown to occur [8]. Endothelial cell erosion may occur in regions exposed to high levels of shear stress (400 dynes/cm^2), [8]. One of the flow parameters which has been known to elevate the shear stress level is pulsatility [32].

In this work, a limited investigation aimed at defining differences in the time-averaged shear patterns between pulsatile and steady flows was undertaken. Physiological pulsatile flow was approximated by the sum of a sinusoidal and a steady flow components. Model 1 was selected for this limited investigation. Frequencies in the range of .34 to .61 sec^{-1} were chosen corresponding to α values from 12 to 18 and velocity amplitude ratio (λ) in the range 0.8 to 1.2 was used. Two mean flow rates corresponding to Reynolds numbers 1315 and 1977 were studied. These flow conditions represented a wide range of physiological flow conditions found in the abdominal aorta in man. Time-averaged current values were obtained from the recorded current signals by numerical integration after digitizing the signals over a period of 1 minute with a step width of 0.2 sec.

Table 6.1 summarizes the calculated time-averaged current from different electrodes on the walls of Model 1 at a Reynolds number equal to 1315. In this set of experiments, flow division ratio was kept constant ($Q_i/Q_t = 0.5$) while both

TABLE 6.1 Time-averaged current values for steady and pulsatile flow.

MODEL 1   Re = 1315

$$Q_i/Q_t = 0.5$$

Electrode	Time-averaged current values $\bar{i}$ (μA)						
	Steady Flow	Pulsatile Flow					
		$\lambda = 0.8$			$\lambda = 1.2$		
	f = 0.0	.34	.42	.61	.34	.42	.61
A1	130.4	131.3	130.8	132.2	131.7	132.6	132.1
A2	135.2	134.8	133.9	135.1	135.2	135.7	136.3
A3	138.6	138.1	138.7	138.6	137.2	136.1	137.4
A4	146.5	146.2	143.2	147.1	150.2	148.3	146.8
A5	89.3	84.3	83.6	87.2	83.3	84.8	88.1
A6	84.1	83.2	79.3	84.4	81.3	83.0	84.1
A7	126.6	124.3	126.6	126.4	125.2	127.6	127.8
A8	139.4	140.0	142.0	142.6	143.2	138.6	139.1
D1	293.0	295.6	296.1	290.0	297.7	296.1	292.2
D2	221.8	218.3	220.3	224.2	220.2	223.8	221.2
D3	185.3	186.1	187.2	188.4	188.3	191.1	186.2
D4	196.1	198.3	198.2	196.6	202.5	199.2	195.1

MODEL I INSIDE WALL

ELECTRODE D4

Re = 1315

$Q_i/Q_t = 0.5$

f = 0.42 c/sec

f = 0.61 c/sec

f = 0.0 (steady flow)

f = 0.34 c/sec

2 sec

μA
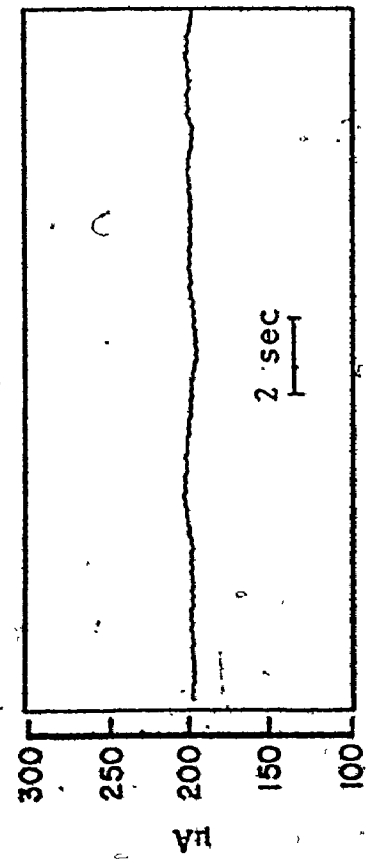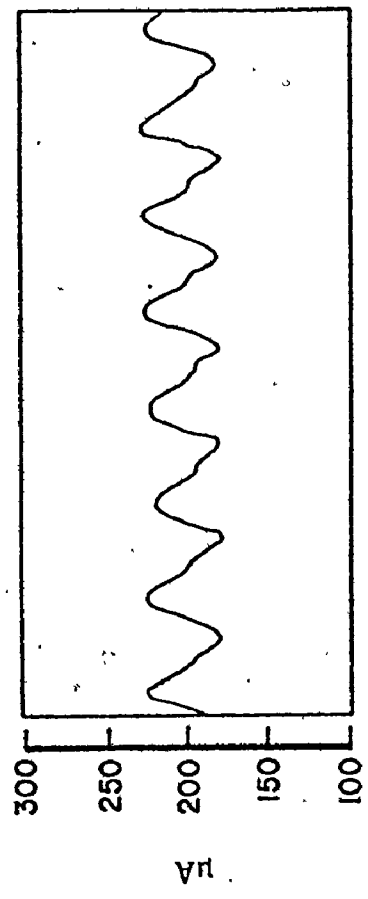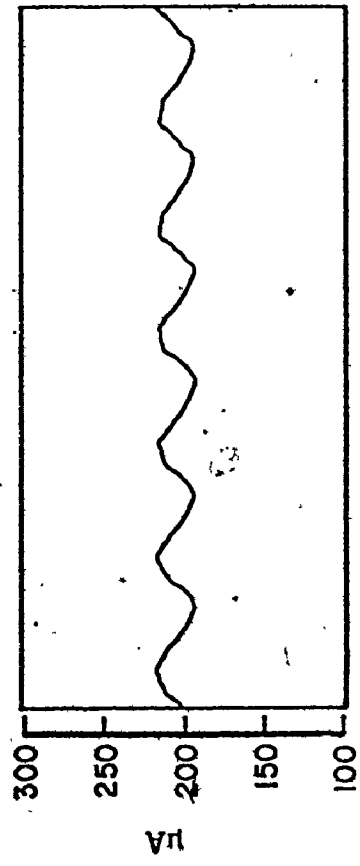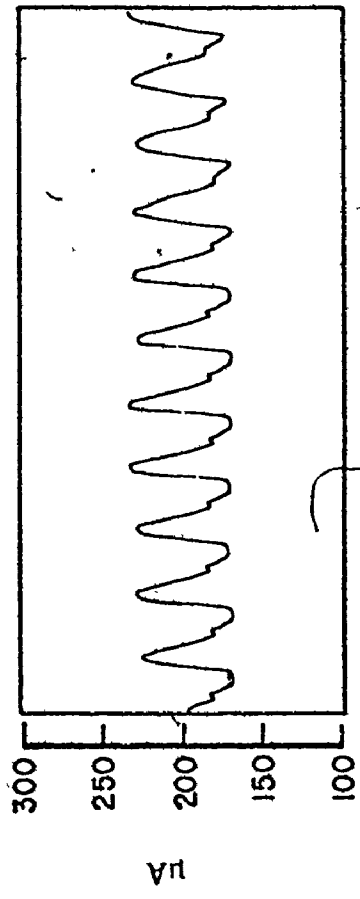
Figure 6.30 Current Signals from Electrode D4 of Model 1 Under Pulsatile Flow Conditions.

TABLE 6.2 Time-averaged current values for steady and pulsatile flow.

MODEL 1   Re = 1977, $\lambda = 1.0$

Time-averaged Current Values $|\bar{i}|\mu A$

Electrode	$Q_i/Q_t = 0.3$			$Q_i/Q_t = 0.4$			$Q_i/Q_t = 0.6$		
	f = 0.0	0.42	0.6	f = 0.0	0.42	0.6	f = 0.0	0.42	0.6
A2	157.1	157.3	157.2	158.3	158.4	158.8	159.2	159.6	159.0
A3	132.3	132.8	133.4	161.8	163.1	163.2	172.4	174.5	171.6
A4	121.1	118.6	119.5	166.3	164.6	166.8	188.1	188.8	187.2
A5	78.6	84.6	83.2	63.6	68.3	59.3	141.3	136.6	141.2
A6	63.6	66.4	67.7	76.8	76.5	72.3	131.8	133.3	132.7
A7	84.4	84.2	83.3	122.3	122.1	121.2	133.6	138.1	135.5
D1	330.0	332.3	332.5	331.2	331.8	332.2	334.7	335.6	336.7
D2	220.5	221.3	224.1	231.1	228.6	230.5	238.0	238.4	239.6
D3	153.5	153.3	157.2	181.6	180.2	184.3	222.1	223.3	224.5
D4	183.4	183.8	18417	209.1	208.5	211.7	234.3	234.3	236.3

147

Figure 6.31 Current Signals from Electrode A5 of Model 1 at Different Q_i/Q_t Values Under Pulsatile Flow Conditions.

frequency and amplitude of the pulsation were variable. These data showed that the time-averaged rate of mass transfer, and hence rate of shear, were not appreciably changed by pulsatile flow. This also held true for a higher Reynolds number (Re = 1977) and different values of flow division ratio (see Table 6.2). The small changes in the time-averaged current values (maximum of $\pm$ 5%) given in Tables 6.1 and 6.2 did not show a consistent functional trend with the pulsatile flow parameters. They were probably due to experimental error resulting from adjusting the flow rates. Samples of the current signals are shown in Figures 6.30 and 6.31.

In Figure 6.30, the signals showed near sinusoidal oscillations of constant frequency which are identical to those of the applied flow oscillations. Non-linear response of the mass transfer rate to the applied sinusoidal flow rate wave appeared as a minor distortion in the signals at high frequencies (f = 0.42 and 0.61 sec^{-1}).

Disturbed flow patterns were observed in pulsatile flow to be similar to those in steady flow. This can be seen in Figure 6.31 where current signals from Electrode A5 are presented. Under separated flow conditions ($Q_i/Q_t \leq 0.4$, see Figure 4.11) irregular fluctuations superimposed upon the sinusoidal signals were observed for all the range of frequencies studied (0.3 to 0.6 sec^{-1}).

6.4 Discussion

In the foregoing sections of this chapter, data was presented for shear rate distribution along the walls of four

rigid-walled models. These models represented three-dimensional realistic geometries of prediseased arterial vessels in man that have been shown to be prone to atherosclerosis. Values of shear rate were obtained through the use of a diffusion-controlled electrochemical technique. The current in the electrochemical cell was measured precisely at the fluid-wall interface over a very small surface area (test electrode surface). Thus, these measurements represent the most detailed set of data on wall shear rate in three-dimensional branching vessels that is currently available.

Previous work in this regard has been limited to the symmetrical branch [16,50,75]. Brech and Bellhouse [16] have measured the wall shear stress in a symmetrical branch ($\beta = 1.12$, $\alpha = 45^{\circ}$) using a hot-film anemometer. The symmetrical model used in this study (Model 1) had the closest geometrical feature of that of Brech and Bellhouse and the shear rate measurement in both models were in the same order of magnitude. However, these authors found that the shear rate everywhere along the walls of the model to vary directly and linearly with the mean input velocity, a result not found in this work where no such simple relationship was obtainable.

The other published work in this regard was by El Masry [50] where he calculated the wall shear rate from velocity profiles obtained via a tracer particle technique. A series of symmetric bifurcations were used in this study with the area ratio as a variable ($\alpha = 0.75$, 1.02 and 1.29). In order to facilitate a comparison between that study and the present

work, one must extrapolate the data given for the smallest
area ratio model (α = 0.75) to a comparable Reynolds number
of that of Model 1. At Reynolds number equal to 1315 the
shear rate values calculated from the velocity profiles were
approximately (40% and 15%) higher than that measured here at
positions 2 and 4 diameters downstream of the carina respect-
ively, though the general characteristics of the shear patterns
were similar. These differences in the shear values may be
attributed to differences in the geometries, i.e., area ratio,
taper of the parent tube and sharpness of the flow divider.

The shear measurements presented in this work have
shown a number of similarities in the shear rate patterns of
the four models. The general feature of these patterns was
that the shear rate distribution is highly non-uniform. Regions
of high and low shear were found in close proximity. The
highest shear rate was found on the leading edge of the flow
dividers. Shear rate approximately 6-10 times as high as it was
in the parent tube were measured at a distance .4-.7 cm
downstream of the carina. Shear rate distribution over the flow
divider was in general stable and unidirectional. Shear rate
was also relatively high at the outside wall (near the corner)
under extreme flow conditions (high total flow rate and high
branch flow ratio). Shear values near Electrodes B4 and B5
in Models 3 and 4 were typically 3 to 5 times as high as the
shear value in the parent tube. However, these areas on the
outside wall experienced low levels of shear rate at different
flow conditions.

Low shear rate levels (less than the parent tube developed flow value) were found on the outside walls of the models under certain flow conditions (low branch flow ratio). Negative shear rate can also exist over these areas under separated flow conditions (see Figures 4.11 to 4.14).

Unstable shear patterns were found at local discrete regions (flow separation regions) on the outside walls of the models under separated flow conditions. Fluctuations in these shear patterns were observed to increase as the branch flow ratio decreases.

For pulsatile flow, time-averaged shear rate values were found appreciably unchanged by variations in the oscillation parameters. Instability in the shear patterns similar to that observed in steady flow and under similar flow conditions was found in pulsatile flow.

CHAPTER 7

BIOLOGICAL IMPLICATIONS

The quality of flow in the vascular system has been related to the sites of predilection of atherosclerosis. Level and stability of pressure and shearing stresses [8, 72], as well as flow separation [4] and vortex formation [23], have been implicated. Consequently, while realizing that other physiological and biochemical factors play an important role in the development of the disease, the present study was focussed on the experimental determination of the hemodynamic field in a number of arterial models and the possible influence of this field on atherogenesis. Detailed fluid dynamic evalution of flow patterns and flow separation phenomenon were carried out. Subsequently, wall shear rate patterns were measured along the walls of the models. Experiments were designed to examine the quality of steady flow over a wide range of physiological flow parameters. A limited investigation aimed at defining differences between pulsatile and steady flows was also undertaken.

The results of this study, when interpreted within the framework of current hypotheses on atherogenesis, indicate that some of the required flow conditions for lesion initiation do exist at branching sites. Some of these conditions are

discussed here in the light of the present work.

Flow Separation

Flow separation phenomenon known also as boundary-
layer separation is characterized by reverse fluid movement
adjacent to the vessel's surface and a recirculating vortex
region. It may occur as a result of cross-sectional area
changes along a conduit [56]. A transition to fluid motions
within the recirculating region (vortex) which are more random,
displaying fluctuating bursts, are also possible at higher flow
rates [57]. These flow conditions are referred to as disturbed
flows. Sites of branching display such cross-sectional area
variation where both in vitro and in vivo vortex motion and
random fluctuation in local velocity have been reported [58-60].

The present work has clearly demonstrated the complex
nature of three-dimensional flows within models of arterial
branches. It has further indicated that arterial shapes are
prone to generate flow separation regions at certain focal
locations. The detailed flow visualization study has shown
that disturbed flows associated with flow separation are not
apt to occur within a range of physiological flow conditions
(Zone B in Figures 4.11 to 4.14). However, exercise is a re-
situation under which cardiac output is increased and flow
distribution occurs, thus, potentially creating conditions
suitable for flow separation. During moderate exercise,
cardiac output may increase 300 percent 6L/min to 18 L/min.

while renal flow decreases by 50 to 80 percent (1.2 L/min normally) and flow to the mesentery decreases substantially [44, 76]. Digestion is another condition resulting in redistribution of blood flow; here flow to the superior mesenteric artery may increase by as much as 132 percent [46]. At rest, the mean flow to a single renal artery is at least 11 percent of flow in the abdominal aorta, corresponding to conditions of no flow separation for most of the cardiac cycle, i.e., Zone B of Figures 4.13 and 4.14 for Models 3 and 4. With exercise, Reynolds number increases and flow division ratio (Q_L/Q_t) decreases, thus creating conditions more suitable for flow separation, i.e., Zones A or AC of Figures 4.13 and 4.14 for Models 3 and 4. It is unlikely, from the present results, that digestion would create flow separation but more likely a shift from the left to the right portion of Zone B of Figure 4.3.

The separated flows observed in all the four models studied here had open recirculating vortex regions. This means that fresh upstream fluid entered and left the separation region simultaneously. This is in contrast to flows downstream of a symmetrical expansion which displays continuously circulating vortex streamlines [57]. In ex vivo stagnation flow, platelet aggregates have been generated both for vortices with closed (symmetrical) and open (asymmetrical) streamlines [77]. Under conditions of higher degrees of asymmetry and greater flow, aggregates were not formed, this was explained in terms of decreased platelet collision frequency and residence time within the vortex. It is possible then that

the separation regions demonstrated here could be areas where platelet aggregates form, possibly dependent on the degree of vortex asymmetry and other flow parameters. It is also known that platelet aggregate formation occures concurrently with the platelet release reaction which liberates such substances as adenine nucleotides (AMP, ADP, ATP), serotonin [38], and a factor necessary for smooth muscle cell proliferation in culture [79]. One may then speculate that over long time periods, months to years, vessel walls adjacent to continuously or discontinuously separated flow could be injured biochemically by such substances.

Mechanical stress fluctuations associated with flow separation have been observed in this work and other in vitro studies [58, 59]. Random velocity fluctuations and localized turbulent bursts akin to those found in vitro models occur in vivo at the junction of the abdominal aorta and iliac artery in dogs [25] and also at the ilioaortic junction in pigs [60]. These flow disturbances were related to the loss of endothelial cell viability leading to defects of the surface. These defects permit free access of plasma to the arterial wall. In the event of a lipoprotein-rich plasma content, atherogenesis is conceived to be more favorable in such locations [60].

In this study, measurements of wall shear rate have shown that areas prone to flow separation exhibit fluctuating shearing stress. These fluctuating patterns were observed to remain localized to relatively discrete regions which were defined visually as separated flow regions. Although the time-

averaged shear level for these fluctuations was not high
enough to cause direct endothelial cell injury [7], shear
rate amplitude was high. Exposure of the adjacent areas of
endothelium to these repeated fluctuating components of shear
over a long period of time could possibly cause structure and
functional changes in the endothelium [8] and set the stage
for atherosclerotic plaque formation.

Wall Shear Rate

Several studies have shown that the transport of
macromolecules into the endothelial surface of arteries
depends upon the level of wall shear rate [9, 10, 11]. Such
dependence has been implicated as a key factor in the develop-
ment of atheroma [2, 72]. In an attempt to elucidate the
fundamental mechanisms by which the transport of macromolecules
across the arterial endothelium is enhanced by mechanical
factors such as pressure and shearing stresses and/or fluctua-
tions in these stresses, both theoretical and experimental
models have been advanced in this regard [9, 10, 11]. Although
these studies have shown that the uptake process is strongly
dependent on mechanical stress exerted on the vessel lining
by the adjacent blood flow, the detailed mechanism of this
process is still obscure.

Depending on the magnitude and stability of the stress
pattern, as well as the duration of exposure, certain intimal
structural and functional changes have been observed to occur
[8]. These processes have widely differing time constants

(T.C., the approximate amount of time from the onset of the stress stimulus until a response becomes apparent). The most salient of these "stress-response" processes and their approximate time constant have been summarized by Fry [8] as follows:

(1) Acute exposure of the endothelial surface to an increased mechanical stress is associated with an increased transendothelial flux of protein into the arterial intima (T.C. ∿ minutes).

(2) A steady unidirectional shear stress orients the endothelial cell and subjacent connective tissue in the direction of the applied stress (T.C. ∿ weeks to months).

(3) Intimal regions chronically exposed to moderately elevated values of unidirectional stress developed intimal fibrous characterized by a dense, highly oriented, subendothelial collagenous sheet that is sparsely populated with smooth muscle and connective tissue cells (T.C. ∿ months to years).

(4) Intimal regions that appear to be exposed to an unstable stress pattern tend to manifest a more exaggerated intimal thickening characterized by an increased population of smooth muscle and connective tissue cells, and a predilection for lipid deposition (T.C. unknown).

(5) Endothelial cell erosion occurs in regions exposed to stresses in excess of about 400 dyn/cm^2 (T.C. minutes to hours).

(6) Endothelial erosion is followed by an exaggerated repetitive response characterized by extraordinary intimal smooth muscle and connective tissue cell proliferation (T.C. ∿ weeks to months).

The relationship of these processes to the shear patterns presented in this work is discussed below.

In order to estimate in vivo shear rate values in similar arterial geometries at comparable Reynolds numbers, one must use a scaling scheme. Since both geometrical and dynamical similarity were maintained in modeling the branching vessels, solution of the non-dimensional Navier-Stokes equation [80] suggested that the non-dimensional velocity gradient at any local position will be the same for the model (M) and the physical system (P). Non-dimensional velocity gradient is defined as $S^* = \frac{\partial u^*}{\partial r^*}$, where $u^* = \frac{u}{\bar{u}}$ and $r^* = \frac{r}{R}$, thus

$$\left(\frac{\partial u^*}{\partial r^*}\right)_P = \left(\frac{\partial u^*}{\partial r^*}\right)_M \tag{7.1}$$

or

$$\left(\frac{\partial u}{\partial r}\right)_P \left(\frac{R}{\bar{u}}\right)_P = \left(\frac{\partial u}{\partial r}\right)_M \left(\frac{R}{\bar{u}}\right)_M \tag{7.2}$$

For geometrically similar conduits R_P is equal to R_M and Equation (7.2) can be written as

$$S_P = S_M \frac{\bar{u}_P}{\bar{u}_M} \tag{7.3}$$

Equation (7.3) means that local in vivo shear rate is equal to that measured from the model multiplied by the ratio between the mean velocities. The viscosity of the test solution used in the present work was approximately one third of that of blood; therefore, the mean velocity used in the model was scaled down by the same ratio, 3, to maintain the same

Reynolds number as that at _in·vivo_ situation.

This study demonstrates clearly the nature and characteristics of the shear stress patterns on the walls of four models of arterial vessels which are prone to athersclerotic plaque formation. Although it was not specifically stated earlier, these models represent pre-disease arterial vessels. If this is the case, then the results of this study predict _in vivo_ maximum shear stresses of the order of 70-100 dynes/cm^2 to occur near the lip of the flow divider in all the four models. These levels of shear stress are well below the level of stress known to cause endothelial cell erosion (ca 400 dynes/cm^2) and mentioned above in shear response processes 5 and 6. Although the maximum shear stress values were measured at distances .3-.7 cm from the flow·divider point, extrapolation of the shear rate values to this point showed that shear stresses of magnitudes of the order of 400 dynes/cm^2 are not likely to occur anywhere in all models even under extreme physiological conditions (high flow rate and high flow division ratio). Since the minimum time constant for any of the above shear response processes is in the order of a few minutes, instantaneous high shear levels occurring at the peak flow rate during the cardiac cycle and last for a fraction of a second are probably not as significant as the time-averaged values. In this work, measurements of time-averaged shear rate under pulsatile flow conditions showed that pulsation has no effect on this quantity. However, it should be noted that the pulsation wave was represented here by a sum of a·sinusoidal and a steady

flow component.

Flaherty et al. [81] studied the detailed topo-
graphic distribution of atherosclerotic lesions in colonies of
swine and dogs that were on an atherogenic regimen. In that
work, the local region of the apex of the flow divider was
shown to be free of lipid deposition in most branch orifices
in both atherosclerotic dogs and swine. A thin but dense
sheet of oriented collagen fibers was prominent beneath a single
layer of endothelial cells in this apical region. The results
of the present study showed that although this region exper-
ienced high shear stress, this stress was stable and unidirectional
(Section 6.2). Even under pulsatile flow conditions flow
reversal was not observed over this region (Section 4.3).
Further downstream from this region the shear stress was observed
to drop abruptly. There, lipid deposition was shown to
localize in the adjacent intimal pads [81].

In contrast to the above, the intimal areas of
curvature of the wall of different branch vessels (branch
outside wall) were shown to experience severe atheromatous
involvement [81]. The present study showed these areas to
experience a wide range of shear stress magnitude depending
on the division of the flow between the branches. The regions
near electrodes A3-A6 in Models 1 and 2 and near electrodes B3-
B5 in Models 2, 3 and 4 (see Section 6.1) could represent either
low or high shear, and possibly negative shear upon occurrence of
flow separation. In addition, these regions experienced unstable
shear patterns characterized qualitatively by high shear

amplitudes, though the frequency of its fluctuations is small. These dramatic variations in shear patterns were the results of variations in flow conditions (total flow rate and flow division ratio) in the conduit. Some physiological conditions (exercise and digestion are two examples) could attribute to these variations.

The forgoing discussion of the shear patterns observed in this study shows that some of the necessary flow conditions for lesion initiation as suggested by Fry [8] can exist within the arterial system. A correlation appears to be valid between the sites of variable and unstable stress patterns and those at which lipid deposition has been shown to develop and between the sites of high, stable and unidirectional shear stress and those which have been shown to be free of lipid deposition. However, it should be mentioned that the relation- ship between shear stress exposure and the subsequent develop- ment of atherosclerosis is not likely to be a simple direct one, but other physiological and biochemical factors must be taken into account. Thus, the suggested correlation will remain pure speculation until the critical studies are done to establish more firmly the detailed interrelationships among the shear-response mechanism, macromolecules transport, vascular tissue lipid metabolism, and connective tissue physiology [8].

CHAPTER 8

SUMMARY AND CONCLUDING REMARKS

Definition of flows in the arterial tree has been recognized as an important step in the understanding of the problem of developing atherosclerosis in man's large arteries. Although physical engineering science has for some time known of the mathematical structure and has had tools for measuring time variant local flows, a complete detailed picture of _in vivo_ fluid mechanics has not emerged. Computation of time and position variant flows, in complex three-dimensional shapes through which non-Newtonian fluids flow, is currently beyond the capabilities of modern computers and mathematical know-how. Experimental tools such as the hot-wire anemometer, the laser doppler anemometer and the electrochemical current measurement probes as well as techniques such as the visualisation techniques are yielding good but incomplete information. It remains to piece together information from various computational and experimental techniques to yield the results for a picture of current understanding.

In the present work, flow patterns in four models representing major arterial vessels in man were studied using two experimental techniques. Neutrally buoyant tracer particle technique was utilized with high speed photography for qualita-

tive study of flow streamline patterns and quantitative defini-
tion of those flow conditions leading to flow separation.
The other technique was a diffusion-controlled electro-
chemical technique. This technique was used to measure the
shear rate distribution patterns along the walls of the models.

This _in_ _vitro_ investigation was carried out in four
three-dimensional rigid-walled models representing the
aortic bifurcation, iliac bifurcation, superior and inferior
mesenteic branches and renal artery branch. The study was
done primarily under steady flow conditions with a limited
set of pulsatile flow experiments aimed at defining differences
between pulsatile and steady flows. Total volumetric flow
rate in the parent tube (Reynolds number) and flow division
ratio between daughter vessels were selected as the key experi-
mental variables, since substantial variation in these is
possible under normal physiological conditions. The pulsatile
flow was represented by a sum of sinusoidal flow and steady
flow components. Fluids used in this study were Newtonian
fluids.

The visualization studies have dealt with qualitiative
observations of flow streamlines and quantitative definition of
flow conditions leading to flow separation over a wide range of
steady flow Reynolds numbers (1000-4000) and a complete range
of flow divisions between daughter vessels. The following
conclusions can be drawn for this part of the work:

1.   The flow patterns in the four models are complicated and characterized by secondary flow motions. Vessel geometry, Reynolds number and flow division ratio are all important in determining the actual flow patterns.

2.   Flow separation is inducible through alteration of flow division between daughter vessels or by an increase in flow rate.

3.   Each of the four models has distinct combinations of flow rate and flow division ratio which give: (1) no flow separation, or (2) flow separation at the outside wall of one of the daughter tubes. Models 3 and 4 also have regions of simultaneous separation on the outside walls of both daughter tubes at high flow rates.

4.   The site of the separation point is approximately constant with the reattachment points occurring further down- stream as Reynolds number increases and as the flow rate in the separation branch decreases.

5.   The separated flows observed here display streamlines forming an open vortex with flows entering and leaving.

6.   For pulsatile flow, flow separation occurs at values of mean flow rates and flow division ratio equal to those for flow separation in steady flow. Both flow conditions for separation and separation point location are independent of pulse frequency in the range of this work ($0.2-0.6$ sec^{-1}).

A diffusion-controlling electrochemical technique was used to measure the shear rate distribution along the walls of the models. This technique is based on an oxidation-reduction

reaction carried out at electrodes implanted in the walls. A very high spatial resolution was achieved by precisely measuring the shear rate over an extremely small surface area of test electrodes at the fluid wall interface. It is believed that the shear data presented in this work represents the first accurate measurements of this quantity in realistic three-dimensional geometries that is currently available. The major conclusions based on this data can be summarized as follows:

1. Distribution of wall shear rate of the branching site in the four models is found to be non-uniform. The actual distribution pattern is a function of the geometry, total flow rate and most importantly the flow divison ratio.

2. A steady and unidirectional high shear stress (70-100 dynes/cm^2) is associated with the leading edge of the flow dividers.

3. Unstable shear stress patterns exist at sites where flow separation is expected to occur. These unstable patterns are characterized by small frequencies and high shear amplitudes.

4. Branch entrance regions (outside wall of the branch) experience a wide range of shear stress depending on the branch flow division ratio. These regions could represent either high or low shear, and possibly negative shear at the onset of separation.

5. The time-averaged rate of shear is not appreciably changed by oscillations introduced by pulsatile flow.

6. A correlation is found between sites of unstable flow and extremes of shear rate exposure with sites at which

atherosclerosis has been shown to develop.

7.   The study points out that flow variables are as important as vessel geometry in defining the local shear stress conditions. Thus it becomes particularly important that _in vivo_ studies which purport to link pathological conditions such as atherosclerosis with hemodynamic phenomena carefully define flow variables.

In closing it should be mentioned that it is unlikely that the level of resolution achieved in the present measurements can even be achieved in the _in vivo_ situation, therefore, future progress towards a solution for this problem will continue to depend on careful _in vitro_ modeling with parallel _in vivo_ studies.

REFERENCES

1. McMillan, G. C., "Development of Arteriosclerosis", The American Journal of Cardiology, Vol. 31, May 1973, pp. 542-546.

2. Caro, C. G., Fitz-Gerald, J. M. and Schroter, R., "Atheroma and Arterial Wall Shear," Proc. of the Royal Society of London, B, Vol. 177, 1971, pp. 109-159.

3. Mustard, J. F., Murphy, E. A. Roswell, H. C. and Downie, H. G., "Platlets and Atherosclerosis", J. of Atherosclerosis Research, Vol. 4, 1964, pp. 1-28.

4. Fox, J. A. and Hugh, A. E., "Localization of Atheroma: A Theory Based on Boundary Layer Separation", Brit. Heart J., Vol. 28, 1966, pp. 388-399.

5. Fry, D. L., "Acute Vascular Endothelial Changes Associated with Increased Blood Velocity Gradients", Circulation Research, Vol. 22, Feb. 1968, pp. 165-197.

6. Caro, C. G. and Nerem, R. M., "Transport of ^{14}C-4 Cholesterol between Serum and Wall in the Perfused Dog Common Carotid Artery", Circulation Res., Vol. 32, 1973, pp. 187-205.

7. Fry, D. L., "Certain Histological and Chemical Responses of the Vascular Interface to Acutely Induced Mechanical Stress in the Aorta of the Dog", Circulation Res., Vol. 24, 1969, pp. 93-109.

8. Fry, D. L., "Responses of the Arterial Wall to Certain Physical Factors" In Atherogenesis: Initiating Factors, Ciba Foundation Symposium 12 Assosc. Scientific Publ., Amsterdam, 1973, pp. 93-125.

9. Caro, C. G., "Transport of ^{14}C-4-Cholesterol between Perfusing Serum and Dog Common Carotid Artery: A Shear Dependent Process", Cardiovascular Res., Vol. 8, 1974, pp. 194-203.

10. Siflinger, A., Parker, K. and Caro, C. G., "Uptake of ^{125}I Albumin by Endothelial Surface of the Isolated Dog Common Carotid Artery: Effect of Certain Physical Factors and Metabolic Inhibitors", Cardiovascular Res., Vol. 9, 1975, pp. 478-489.

11. Weinbaum, S. Lewis, C. and Caro, C. G., "Theoretical Models and Electronmicroscopic Studies on the Transport of Macromolecules across Arterial Endothelium and their Uptake by the Arterial Wall". In NSF Specialists Meeting on Fluid Dynamic Aspects of Arterial Disease, Ohio State University, Columbus, Ohio (1974).

12. Knox, W. R., "An Experimental Investigation of the Steady Flow of a Viscous Fluid in Circular, Branched Tubes", M.Sc. Thesis, University of Minnesota (1962).

13. Schroter, R. C. and Sudlow, M. F., "Flow Patterns in Models of the Human Bronchial Airways", Respiration Physiology, Vol. 7, 1969, 341-355.

14. Pedley, T. J., Schroter, R. C. and Sudlow, M. F., "Flow and Pressure Drop in Systems of Repeatedly Branching Tubes", J. Fluid Mechanics, Vol. 46, 1971, pp. 365-383.

15. Schreck, R. M. and Mockros, L. F., "Fluid Dynamics in the Upper Pulmonary Airways". In AIAA Fluid and Plasma Dynamics Conf., 3rd, Los Angeles, 1970.

16. Brech, R. and Bellhouse, B. J., "Flow in Branching Vessels", Cardiovascular Res., Vol. 7, 1973, pp. 593-600.

17. El Masry, O. A., "Flow Patterns and Wall Shear Rates in a Series of Symmetric Bifurcations", M.Eng. Thesis, McMaster University, Hamilton, Canada (1974).

18. Roach, M. R., Scott, S. and Ferguson, G. G., "The Hemodynamic Importance of the Geometry of Bifurcations in the Circle of Willis (Glass Model Studies)", Stroke, Vol. 3, 1972, pp. 255-267.

19. Rodkiewicz, C. M. and Roussel, C. L., "Fluid Mechanics in Large Arterial Bifurcations", Trans. ASME, 1973, pp. 108-112.

20. Rodkiewicz, C. M., "Localization of Early Atherosclerotic Lesions in the Aortic Arch in the Light of Fluid Flow", J. Biomechanics, Vol. 8, 1975, pp. 149-156.

21. Talukder, N., "An Investigation on the Flow Characteristics in Arterial Branching", Paper 75-APMB-4, Symp. Biomech., 1975, Troy, New York.

22. Goldsmith, H. L., "The Flow of Model Particles and Blood Cells and its Relation to Thrombogenesis", Progress in Hemostasis and Thrombosis, Vol. I (ed. T.H. Spaet), 1972, pp. 97-139, New York, Grune and Stratton.

23. Yu, S. K. and Goldsmith, H. L., "Behaviour of Model Particles and Blood Cells at Spherical Obstruction in Tube Flow", Microvasc. Res., Vol. 6, 1973, pp. 5-31.

24. Murphy, E. A., Rowsell, H. C., Downie, D. V. M., Robinson, G. A. and Mustard J. F., "Encrustation and Atherosclerosis: The Analogy between Early In Vivo Lesions and Deposits which Occur in Extracorporeal Circulations", Canad. Med. Assoc. J., Vol. 87, No. 6, 1962, pp. 259-274.

25. Gutstein, W. H., Farrell, G. A. and Schneck, D. J.,
    "In Vivo Demonstration of Junctional Blood Flow Disturbance
    by Hot Wire Anemometry", Atherosclerosis, Vol. 11, 1970,
    pp. 485-496.

26. Schultz, D. L., Tunstall-Pedoe, D. S., Lee, G., DeJ.,
    Grunning, A. J. and Bellhouse, B. J., "Velocity Distribu-
    tion and Transition in the Arterial System", Circulatory
    and Respiratory Mass Transport, A Ciba Foundation Symposium
    (ed. G. E. W. Wolstenholme and J. Knight) Churchill,
    London (1969).

27. Lew, H. S., "Low Reynolds Number Equi-bifurcation Flow in
    Two-dimensional Channel", J. Biomechanics, Vol. 4 (1971),
    pp. 559-568.

28. Lew, H. S., "The Dividing Streamline of Bifurcation Flows
    in a Two-dimensional Channel at Low Reynolds Number",
    J. Biomechanics, Vol. 6, 1973, pp. 423-432.

29. Lynn, N. S., Fox, V. G. and Ross, L. W., "Computation of
    Fluid-dynamic Contribution to Atherosclerosis at Arterial
    Bifurcations", Biorhealogy, Vol. 9, 1972, pp. 61.

30. Lamir, M. and Roach, M. R., "Blood Flow of a Two-dimensional
    Bifurcation", J. Theor. Biol., Vol. 42, 1973, pp. 33-48.

31. Ehrlich, L. W., "Digital Simulation of Periodic Fluid Flow
    in a Bifurcation", Computers and Fluids, Vol. 2, 1974,
    pp. 237-247.

32. Friedman, M. H., O'Brian, V. and Ehrlich, L. W.", Calculation
    of Pulsatile Flow through a Branch", Circulation Res.,
    Vol. 36, 1975, pp. 277-285.

33. Ray, G. and Davids, N., "Shear Stress Analysis of Blood-
    Endothelial Surface in Inlet Section of Artery with
    Plugging", J. Biomechanics, Vol. 3, 1970, pp. 99-110.

34. Davids, N. and Cheng, R. C., "Transient Laminar Flow in
    Ducts of Arbitrary Cross-Section by Finite Element Methods",
    J. Biomechanics, Vol. 5, 1972, pp. 485-499.

35. Mitchell, J. R. A. and Schwartz, C. J., "Arterial Diseases",
    Blackwell Scientific Publications, Oxford (1965).

36. Gray, H., "Anatomy of the Human Body", Twenty-eighth edition,
    Lea and Febiger (Philadelphia), 1976.

37. Guyton, A. C., Textbook of Medical Physiology, 4th ed.,
    W. B. Saunders Co., Philadelphia, 1971.

38. Fry, D. L., Griggs, D. M. and Greenfield, J. C., Jr.,
     In Vivo Studies of Pulsatile Blood Flow", In Pulsatile
     Blood Flow (Edited by Attinger., E. O.) McGraw-Hill,
     New York (1964).

39. Ling, S. C., Alabek, H. B. and Carmody, J. J., "Pulsatile
     Flow in Arteries", 12th International Congress of Applied
     Mechanics, 1968.

40. Vander Werff, T. J., "Significant Parameters in Arterial
     Pressure and Velocity Development", J. Biomechanics,
     Vol. 7, 1974, pp. 437-447.

41. Gosling, R. G., Newman, D. L. Bowden, N. L. R., and Twinn,
     K. W., "The Area Ratio of Normal Aortic Junctions" Br. J.
     Radial., Vol. 44, 1971, pp. 850-853.

42. Zeller, H., Talnkder, N. and Lorenz, J., "Model Studies
     of Pulsating Flow in Arterial Branches and Wave Propagation
     in Blood Vessels", AGARD Conférence Proceedings #65 on
     Fluid Dynamics of Blood Circulation and Respiratory Flow,
     May 1970.

43. Burton, A. C., "Physical Principles of Circulatory Phenomena",
     Handbook of Physiology.

44. Andersen, K. L., "The Cardiovascular System in Exercise".
     In Exercise Physiology, Edited by Falls, H. B.,
     Academic Press, New York, 1968, pp. 79-127.

45. De Bakey, M. E., Burch, G.; Ray, T. and Ochsner, A.,
     "The Borrowing-Landing Hemodynamic Phenomenon and its
     Theraputic Application in Peripheral Vascular Disturbances",
     Annals of Surgery, Vol. 126, 1947, pp. 850-865.

46. Fronek, K. and Fronek, A., "Combined Effect of Exercise
     and Digestion on Hemodynamics in Concious Dogs", Am. J.
     Physiol., Vol. 218, 1970, pp. 555-559.

47. Womerseley, J. R., "Method for the Calculation of Velocity,
     Rate of Flow and Viscous Drag in Arteries' when the
     Pressure Gradient is Known", J. Physiol., Vol. 127,
     553-563, 1955.

48. Attinger, E. O., "Hydrodynamics of Blood Flow", in Advances
     in Hydrescience, Vol. 3, ed. V. T. Chow, Academic Press,
     New York, 1966, pp. 111-152.

49. Kuchar, N. R., and Ostrach, S., "Unsteady Entrance Flow
     in Elastic Tubes with Application to the Vascular System",
     AIAA Journal, Vol. 9, pp. 1520-1527, 1971.

50. Feuerstein, I. A., El Masry, O. A. and Round, G. F., "Arterial Bifurcation Flows: Effect of Flow Rate and Area Ratio", Can. J. Physio. Pharm., Vol. 54, No. 6, 1976, pp. 795-808.

51. Schlichting, H., "Boundary Layer Theory", 6th Edition, McGraw-Hill, 1968.

52. Despard, R. A. and Miller, J. A., "Separation in Oscillating Laminar Boundary Layer Flows", J. Fluid Mech., Vol. 47, 1971, pp. 21-32.

53. Schneck, D. J. and Ostrach, S., "Dependence of Unsteady Flow Separation on Frequency of Oscillation", Proceedings of 26th ACEMB, Minneapolis, Minnesota, Sept. 1973.

54. Feuerstein, I. A. and Woods, D. R., " A Photographic Technique for Measuring Fluid Velocities with Tracer Particles", J. SMPTE, Vol. 82, 1973, pp. 916-923.

55. Pike, G. K., "Laminar Flow Development Downstream of an Abrupt Circular Channel Expansion", M.Eng. Thesis, McMaster University, Hamilton, Canada, 1973.

56. Macagne, E. O. Hung, T. K., "Computational and Experimental Studies of a Captive Annular Eddy", J. Fluid Mech., Vol. 28, 1967, pp. 43-64.

57. Back, L. and Roschke, E., "Shear Layer Flow Regimes and Wave Instabilities and Reattachment Lengths Downstream of an Abrupt Circular Channel Expansion", J. Appl. Mech., Vol. 39, 1972, pp. 677-681.

58. Gutstein, W. H. and Schneck, D. J., "In Vitro Boundary Layer Studies of Blood Flow in Branched Tubes", J. Atheros. Res., Vol. 7, 1967, pp. 295-299.

59. Gutstein, W. H., Schneck, D. J. and Marks, J. O.", In Vitro Studies of Local Blood Flow Disturbance in a Region of Separation", J. Atheros. Res., Vol. 8, 1968, pp. 381-388.

60. Gutstein, W. H., Farrell, G. A. and Armellini, C., "Blood Flow Disturbance and Endothelial Cell Injury in Preatherosclerotic Swine", Lab. Invest., Vol. 29, 1973, pp. 134-149.

61. Mizushina, T., "The Electrochemical Method in Transport Phenomena". In Irvin, T. F. and Hartnett, J. P. (Eds.): Advances in Heat Transfer", Academic Press, New York, New York, 1971, pp. 87-161.

62. Mitchell, J. E. and Hanratty, T. J., "A Study of Turbulence at a Wall Using an Electrochemical Wall Shear Stress Meter", J. Fluid Mechanics, Vol. 26, part 1, 1966, pp. 199-221.

63. Dimopoulos, H. G. and Hanratty, T. S., "Velocity Gradeints at the Wall for Flow Around a Cylinder for Reynolds Numbers between 60 and 360", J. Fluid Mechanics, Vol. 33, part 2, 1968, pp. 303-319.

64. Hinze, J. O., "TURBULENCE: An Introduction to Its Mechanism and Theory", McGraw-Hill, New York, 1959, pp. 75-112.

65. Fortuna, G. and Hanratty, T. J., "Frequency Response of the Boundary Layer on Wall Transfer Probes", J. Heat Mass Transfer, Vol. 14, 1971, pp. 1499-1507.

66. Knudsen, J. G. and Sutey, A. M. "Effect of Dissolved Oxygen on the Redox Method for the Measurement of Mass Transfer Coefficients", I & EC Fundamentals, Vol. 6, No. 1, 1967, pp. 132-139.

67. Eisenberg, M., Tobias, C. W. and Wilke, C. R., "Selected Physical Properties of Ternary Electrolytes Employed in Ionic Mass Transfer Studies", J. of the Electrochemical Society, Vol. 103, No. 7, 1956, pp. 413-416.

68. Reiss, L. P. and Hanratty, T. J., "Measurements of Instant-aneous Rates of Mass Transfer to a Small Sink on a Wall", A.I.Ch.E. Journal, Vol. 8, No. 2, 1962, pp. 245-247.

69. Reiss, L. P. and Hanratty, T. J., "An Experimental Study of the Unsteady Nature of the Viscous Sublayer", A.I.Ch.E. Journal, Vol. 9, No. 2, 1963, pp. 154-160.

70. Son, J. S. and Hanratty, T. J., "Limiting Relation for the Eddy Diffusivity Close to a Wall", A.I.Ch.E. Journal, Vol. 13, No. 4, 1967, pp. 689-696.

71. Son, J. S. and Hanratty, T. J., "Velocity Gradients at the Wall for Flow Around a Cylinder at Reynolds Numbers from 5×10^3 to 10^5". J. Fluid Mech., Vol. 35, part 2, 1969, pp. 353-368.

72. Fry, D. L., "Localization Factors in Arteriosclerosis", In Likoff, W., Segal, B. L., Insull, W. and Moyer, S. J. (Eds.): Atherosclerosis and Coronary Heart Disease, Grune and Stratton Inc., New York, N.Y., 1972, pp. 85-104.

73. Clark, C., "Turbulent Velocity Measurements in a Model of Aortic Stenosis", J. Biomechanics, Vol. 9, 1976, pp. 677-687.

74. Fredberg, J. J. "Turbulent Wall Pressure Fluctuations in Stenosed Arteries", M.I.T. Fluid Mechanics Laboratory Report 74-1, Cambridge, Massachusetts, 1974.

75. Round, G. F., El Masry, O. A. and Feuerstein, I. A., "Wall Shear Rate as Related to Thrombus and Atheroma Generation in Bifurcations", 5th Canadian Med. Biol. Engg. Conf., Digest of Papers, Montreal, Quebec, Sept. 1974.

76. Carlsten, A., and Grimby, G., "The Circulatory Response to Muscular Exercise in Man", Springfield, Charles C. Thomas, 1966, p. 16.

77. Morton, W. A., Pormentier, E. M. and Petschek, H. E., "Study of Aggregate Formation in Region of Separated Blood Flow", Thrombos. Diathes. Haemorrh., Vol. 34, 1975, pp. 840-854.

78. Mustard, J. F., and Packham, M. A., "Factors Influencing Platelet Function: Adhesion Release and Aggregation", Pharmacol. Rev., Vol. 22, 1977, pp. 97-187.

79. Ross, R., Glomset, J., Kariya, B., and Harker, J., "A Platelet-Dependent Serum Factor that Stimulates the Proliferation of Arterial Smooth Muscle Cells in Vitro", Proc. Natl. Acad. Sci., U.S.A., Vol. 71, 1974, pp. 1207-1210.

80. Yuan, S. W., "Foundations of Fluid Mechanics", Prentice-Hall Inc., Englewood Cliffs, New Jersey, 1967.

81. Flaherty, J. T., Ferrans, V. J., Pierce, J. E., Carew, T. E. and Fry, D. L., "Localizing Factors in Experimental Atherosclerosis", In Likoff, W., Segal, B. L., Insull, W., and Mayer, S. J. (Eds.): Atherosclerosis and Coronary Heart Disease, Grune and Stratton, Inc., New York, N.Y., 1972, pp. 40-83.

82. Bergel, D. H., "The Dynamic Elastic Properties of the Arterial Wall", J. Physiol., Vol. 156, (1961), 458-469.

83. Peterson, L. H., Jensen, R. E., and Parnell, J., "Mechanical Properties of the Arteries In Vivo", Circulation Res., Vol. 8, 1960, 622-636.

84. Patel, D. J., Greenfield, Jr., J. C. and Fry, D. L., "In Vivo Pressure-Length-Radius Relationship of Certain Blood Vessels in Man and Dog", in Pulsatile Blood Flow, E. Attinger, Ed., McGraw-Hill, New York, 1964, pp. 293-305.

85. Whitmore, R. L., "Rheology of the Circulation", Pergamon Press, 1968.

86. Segré, G. and Silberberg, A., "Behaviour of Macroscopic Rigid Spheres in Poiseuille Flow, Part 2: Experimental Results and Interpretation", J. Fluid Mech., Vol. 14, 1962, pp. 136.

87. Jeffrey, R. C. and Pearson, J. R. H., "Particle Motion in Laminar Vertical Tube Flow", J. Fluid Mech., Vol. 22, 1965,

88. Brenner, H. in Advances in Chemical Engineering, Vol. 6, Edited by Drew, T. B., et al., Academic Press, New York, 1966.

89. Brenner, H. and Bungay, P. M., "Rigid-Particle and Liquid Droplet Models of Red Cell Motion in Capillary Tubes", Federation Proceedings, Vol. 30, 1971.

90. Lighthill, M. J., "Physiological Fluid Dynamics: a Survey", J. Fluid Mech., Vol. 52, part 3, 1972, pp. 475-497.

APPENDIX A

ASSUMPTIONS USED IN THE STUDY

1. Assumption Regarding the Arterial Vessel Wall

The local rheological properties of the arterial vessel
wall are determined by the relative amounts of the basic
wall constituents: elastin, collagen and smooth muscle fibers.
The single-cell layer lining the inner wall of the vessel, the
endothelium, does not contribute to the mechanical response of
the wall [82]. The contribution of elastin, collagen and
muscle to the structure of the vessel wall varies as a function
of vessel size, space and time. Since these components deter-
mine the mechanical properties of the vessel wall their relative
importance would be different in models which represent arteries
of different size or at different locations [82].

The fact that the wall displacement associated with
the pressure pulse is small has been confirmed by a number of
investigators [82, 83]. The corresponding changes in cross
section are usually less than 2% for vessels with a radius in
the range around 0.5 cm., less than 5% for the aorta and 10-15%
for the pulmonary artery, both in man and in dogs [84]. Except
for the pulmonary artery (12%) and the ascending aorta (5%) the
longitudinal strain is of the order of 1% for arteries.

The assumption used in this study that the wall is rigid
for models of the large branches and bifurcations of the

abdominal aorta is justified for steady flow, where only a mean static pressure acts on the wall and causes no wall motion. For pulsatile flow Lighthill [90] argued that in addition to the fact that the variation of the cross section as a pulse passes is small, also the pulse propagation speed is much higher than the maximum blood velocity so that pressure changes are felt over short distances (such as those involved in this study) in times which are much shorter than the characteristic flow time.

2. Assumption Regarding the Newtonian Behaviour of Blood

Blood is a suspension of some formed elements [40-50% of its volume) mainly the red blood cells, which are highly flexible disk-shaped bodies, white blood cells and platelets, in a transparent fluid, the blood plasma. Although plasma has flow properties close to a Newtonian fluid the presence of elements complicates the rheological behaviour of whole blood. Values of effective viscosity of blood show a substantial increase with decreasing rate of shear. This is due to increased formation of various aggregations of red blood cells at the lower shear rates [85]. As the shear rate is increased the aggregates break up and separate into individual cells which results in a linearization of the shear stress vs. shear rate curve. With shear rates in the range $(100-1000 \, \text{sec}^{-1})$ the measured apparent viscosity of blood varies little with shear rate and errors from treating blood as a Newtonian fluid with constant viscosity are not significant [85]. In large arteries such as the aorta

and its major branches, the maximum and mean shear rates are in the range from 100 to 1000 sec^{-1} and the error introduced by considering blood as a Newtonian fluid are probably very small.

APPENDIX B

USE OF TRACER PARTICLES AS A
REPLACEMENT FOR FLUID PARTICLES

It is necessary to consider the accuracy with which a small element of the fluid continuum may be represented by a solid, spherical particle of finite size. Deviations of the path and velocity of tracer particles from the path and velocity of the fluid may be attributed to the following

(a) Deviations Caused by Boundaries or Walls

It is known that the shear stress distribution at the solid/liquid interface, together with the particle's own inertia, results in a radially directed force causing the particle to migrate, in a fully developed Poiseuille flow, to an equilibrium position at about 0.6 R and that this occurs even under neutrally buoyant conditions. Segre and Silberberg [86] and Jeffery and Pearson [87] have shown that both Reynolds number (Re) and particle to tube diameter ratio ($\bar{P}$) are most important in correlating their radial velocity data. Radial velocities were found to decrease and approach zero as both parameters approach zero. Brenner [88] points out that these two parameters also arise from theoretical analysis.

(b) Deviations Caused by a Particle Slip Velocity

Brenner and Bungay [89] have shown that the particle to tube diameter ratio (P) is important in defining the difference

178

between the actual particle translational velocity and the Poiseuille flow velocity. As P approaches zero, the difference approaches zero.

c) Deviations Caused by Accelerating Flows

Newton's second law indicates that the tracer particle will accelerate with the fluid as its mass approaches zero leading to small values of P to assure the proper acceleration of particles.

The above conditions were found true in Poiseuille flow in a straight tube implying steady state conditions and no secondary flows. However, similar parameters would be expected to be important in describing the motion of particles in geometries more complicated than a straight tube. In addition, the above analysis indicates that neutrally buoyant particles tend to imitate the fluid particles they replace as the particle diameter approaches zero.

A criterion for determining whether the deviation from fluid behaviour is significant many be developed on the basis of the relationship between the particle migration and slip velocities and the parameter P. Feuerstein and Woods [54] have argued that the first derivatives of the migration and slip velocities with respect to particle size are small if particles with a size ratio of two or more give equivalent results. Since the deviation velocities increase monotonically from zero with particle size, a small first derivative indicates a small deviation velocity and, therefore, a situation in which particles give accurate streamline traces and velocities.

APPENDIX C

ESTIMATION OF DISPLACEMENT OF PARTICLE IMAGE
DUE TO DIFFERENCE IN REFRACTIVE INDICES

The difference in refractive indices between perspex of the model (1.4812) and the suspending fluid (1.3542) would result in some error in locating the real particle position due to the refraction of bounding rays at the liquid/perspex interface. The maximum error is incurred for the case of a particle situated close to the. tube wall and the bouding ray which is at right angles to the line joining the tube axis and the particle centre. This ray strikes the tube wall at the largest angle of incidence. For a particle of diameter 300 μ situated at a distance of 2 mm from the wall (where the closest particle to the wall was traced), this angle may be found by a geometrical construction to be 58°.

The angle of refraction at the inner wall is given by:

$$\frac{Sin\ i}{Sin\ r} = {}_\ell n_p$$

where   i   is the angle of incidence at the inner wall

r   is the angle of refraction

${}_\ell n_p$ is the index of refraction for a ray travelling from the liquid to the perspex

For a compound wall

$${}_1 n_2 = \frac{n_2}{n_1}$$

Hence

$$\text{Sin } r = \frac{\text{Sin } i}{_\ell n_p} = \text{Sin } i \times \frac{n_\ell}{n_p} = \frac{1.3542}{1.4812} \text{Sin } i$$

For an angle of incidence of 58°, $r = 51^O$ and the angle through which the ray is deflected is 7°. The path length is equal to the thickness of the perspex at this position and is approximately equal to 4 mm. Assuming that the incident and emergent rays are parallel, hence the image of the particle centre is shifted through about 0.5 mm, or less than 2% of the tube diameter, for the worst case.

APPENDIX D

THE USE OF THE ELECTROCHEMICAL TECHNIQUE
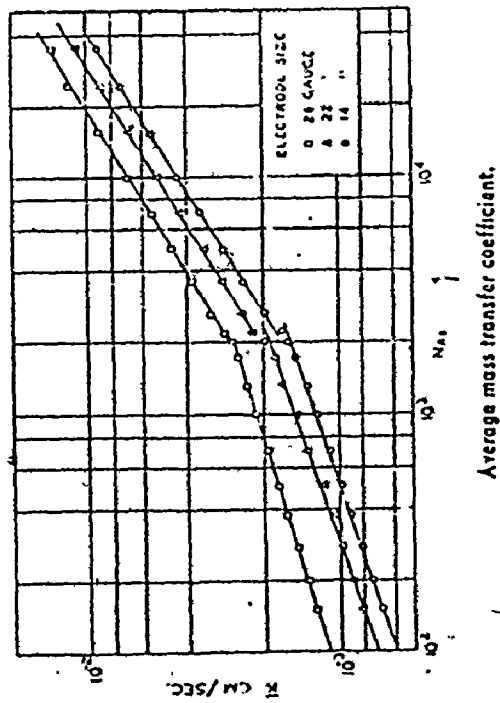IN SHEAR RATE MEASUREMENTS: APPLICATIONS

The electrochemical measurements of wall velocity gradient (shear rate) is the mass transfer analog of the thermal wall anemometer. The technique is based on measuring a limiting diffusion current at an electrode mounted flush with the wall. It has been used successfully by the group of Hanratty and his coworkers [63, 69, 70, 71] for measurements of wall shear stress in a pipe and around a cylinder. The purpose of this appendix is to review these applications and to point out the accuracy of this method in predicting the wall shear rate under a wide range of flow parameters.

One of the simplest systems in which to check the accuracy of the equation relating the mass transfer measurements to the velocity gradient (Equation (5.21) is fully developed flow in a circular pipe. For laminar flow the velocity gradient at the wall can be calculated from the measured volumetric flow rate using the Hagen-Poiseuille equation [80].. For turbulent flow it can be calculated from the measured pressure drop using a force balance [80]. Tests in a 2.54 cm (1 in.) pipe have shown that the electrochemical technique predicts accurate values of the wall velocity gradient over a Reynolds number range of 300-70,000 [69], [70]. The results of these tests are shown in Figure D.1.

(b)
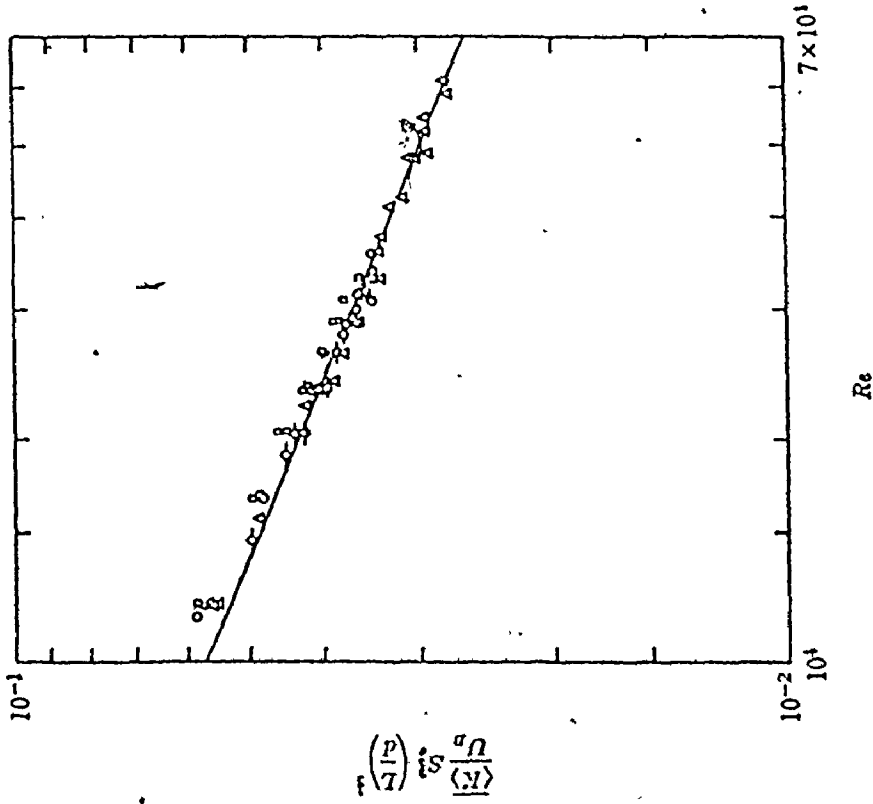
Average mass-transfer measurements. O, $L/d = 0.007$;
□, $L/d = 0.005$; △, $L/d = 0.003$; -O-, $L/d = 0.021$.

$\frac{\langle K \rangle}{U_a} Sc^{\frac{2}{3}} \left(\frac{L}{d}\right)^{\frac{1}{3}}$

Re

(a).

Average mass transfer coefficient,

Figure D.1   Comparison between Measured Mass-Transfer Coefficient in Fully
Developed Flow and Values Predicted by Equation (5.21)
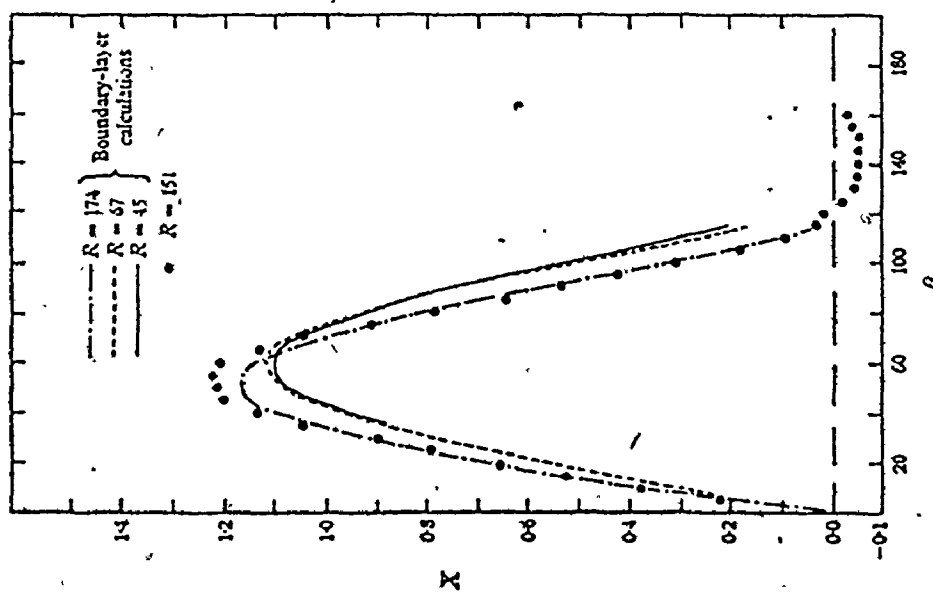(a) from reference [69]
(b) from reference [70].

The electrochemical technique has also been used to study the flow around solid objects. A study by Dimopoulos and Hanratty [63] of the distribution of the wall velocity gradient around a cylinder of 2.54 cm (1 in.) diameter indicates that the boundary-layer theory correctly predicts the measurements between the front stagnation point and the separation for Reynolds number, Re greater than 150. This result is shown in Figure D.1(a).

A companion study to that mentioned above was carried out by Son and Hanratty [71] over a Reynolds number range from 5×10^3 to 10^5. This study showed that the measured velocity gradients prior to separation are described satisfactorily by boundary-layer theory. The agreement between the boundary-layer calculations based on pressure measurements and the electrochemical measurements is shown in Figure D.2(b).
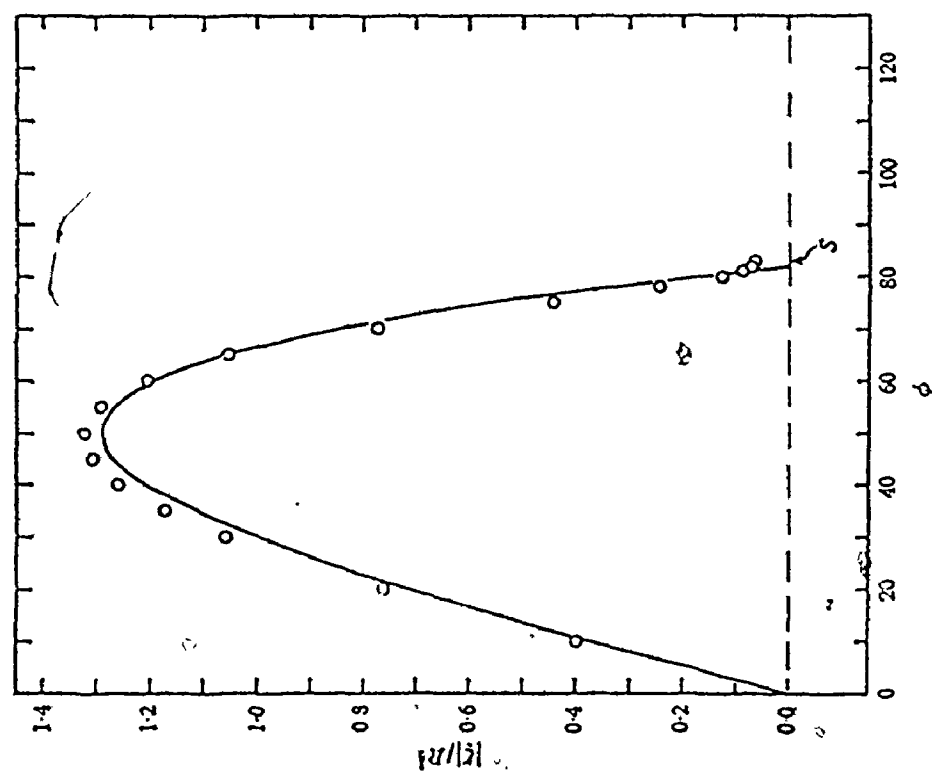
Comparison between boundary-layer calculations and measurements. O, this
study, $R = 20,000$; ———, boundary-layer solution, $R = 10,000$.

(b)

Comparison between boundary-layer calculations
and measurements.

(a)

Figure D.2 Comparison between Bounary-Layer Theory Calculations and Electro-
chemical Measurement of Shear Rate Around a Cylinder
(a) from reference [63]
(b) from reference [71].